Optimisation of PAN-based nanofibres with in situ graphene synthesis and rapid evaluation of graphene-reinforced composites via advanced thermogravimetric analysis

Bianca Nicole Bauer

Linacre College
University of Oxford

A thesis submitted for the degree of
MSc By Research

Trinity 2024

Abstract

The global transition to a low-carbon economy drives the demand for high-performance materials like carbon fibres, which are essential in industries such as automotive and renewable energy.
Polyacrylonitrile (PAN) is the leading precursor in carbon fibre manufacturing because of its high carbon yield and mechanical strength. The performance of carbon fibres is directly determined by the properties of the PAN precursor fibres.
However, current production methods do not fully exploit the theoretical mechanical potential of PAN. Enhancing the mechanical performance of PAN fibres by incorporating graphene is promising, but commercial graphene typically exhibits low quality, with high defect densities and multiple layers (>10 layers), with dispersion being an additional challenge.
This study addresses these limitations by introducing a novel approach: incorporating in situ synthesised graphene into PAN precursor solutions, achieving a uniform dispersion of 0.21 mg/ml graphene with an average of nine layers.
The precursor solution is then used to produce fibres via electrospinning on a drum collector, rotating at approximately 8000 rpm, corresponding to a linear velocity of $\sim$67 m/s. This process produces uniform, graphene-reinforced fibres with an average diameter of 228 ± 45 nm, demonstrating a threefold improvement in stretchability over non-reinforced fibres.
Furthermore, advanced thermogravimetric analysis (TGA) is introduced as a rapid evaluation tool for graphene-polymer composites. The advanced TGA of the PAN-graphene composite confirms successful graphene integration and identifies a previously unobserved decomposition event at 412 °C, specific to shear-exfoliated graphene.

Optimisation of PAN-based nanofibres with in situ graphene synthesis and rapid evaluation of graphene-reinforced composites via advanced thermogravimetric analysis



Bianca Nicole Bauer

Linacre College

University of Oxford

A thesis submitted for the degree of

MSc By Research

Trinity 2024

Contents

1 Polyacrylonitrile (PAN) polymer in material science: challenges, innovations and advanced composite analysis 1

1.1 The importance of PAN fibres . . . 2
1.2 Untapped potential and challenges of PAN-based carbon fibres . . . 4
1.3 Electrospinning PAN precursor fibres: addressing structural challenges in carbon fibre production . . . 5
1.3.1 Structural optimisation: integrating graphene to improve PAN-based precursor fibres . . . 8
1.4 Innovative strategies for PAN nanofibre fabrication and graphene composite material evaluation . . . 10
1.4.1 Optimising PAN nanofibre fabrication via electrospinning with in situ synthesised embedded graphene: a novel synthesis strategy . . . 10
1.4.2 Advanced thermogravimetric analysis as a non-conventional, rapid route for the evaluation of graphene-reinforced composites . . . 12
1.5 Thesis structure and chapter overview . . . 15

2 Direct exfoliation of graphene in PAN-based solutions: a novel fibre-synthesis precursor 17

2.1 Shear-mixing: process overview of preliminary exfoliation and experimental parameters . . . 20
2.2 Ultrasonication: further exfoliation and experimental details . . . 22
2.3 Centrifugation: separation process and detailed experimental parameters . . . 23
2.3.1 Centrifugation: experimental parameters and remarks . . . 25
2.4 Application of the graphene-PAN polymer precursor in electrospinning . . . 27

3 Standard characterisation and analysis of shear-exfoliated graphene 28

3.1 Sample preparation for characterisation: polymer removal using vacuum filtration 28
3.2 Quality assessment of graphene through Raman spectroscopic analysis . . . 30
3.2.1 Benchmarking graphene quality: Raman spectra insights from literature review . . . 30
3.2.2 Experimental evaluation of key Raman spectral characteristics in graphene shear-exfoliated from various PAN concentrations . . . 36

3.2.3 Graphene defect and flake size analysis . . . 41
3.2.4 Graphene layer thickness determination . . . 45
3.3 Quantifying topography of graphene via atomic force microscopy analysis . . . 51
3.3.1 Comparative analysis of AFM images from literature: graphene production via CVD, hummers' method, and shear-mixing . . . 51
3.3.2 AFM results for graphene produced by the synthesis process in this study 56
3.4 Quantifying graphene concentration via UV-Vis absorption spectroscopy analysis 59
3.4.1 Characterisation technique: UV-Vis absorption spectroscopy . . . 59
3.4.2 Application of the Beer-Lambert law for determining graphene concentration 60

4 Advanced thermogravimetric analysis for graphene characterisation 63
4.1 Characterisation technique: thermogravimetric analysis . . . 63
4.2 Advanced TG analysis: addition of deconvolution for overlapping peaks . . . 65
4.2.1 Fitting algorithm . . . 65
4.3 TGA: literature and established thermal decomposition profiles . . . 68
4.3.1 PAN decomposition dynamics . . . 68
4.3.2 Thermal behaviour of carbon-based materials . . . 70
4.4 Graphene quality assessment through advanced TGA . . . 72
4.4.1 Reproducibility study at different heating rates . . . 72
4.4.2 Reference standards . . . 74
4.4.3 Deriving insights from advanced TGA: a comparative study . . . 78
4.5 Key advanced TGA findings in graphene characterisation . . . 86

5 Synthesis and characterisation of graphene-reinforced electrospun PAN fibres 89
5.1 Characterisation technique: scanning electron microscopy . . . 89
5.2 Synthesis method: electrospinning . . . 91
5.2.1 Key-parameters and their effects . . . 93
5.3 Development and construction of the experimental setup . . . 95
5.4 Parametric study and optimisation on PAN fibres . . . 98
5.4.1 Electrospinning parameter analysis at zero speed: the standard collector . 98
5.4.2 Enhancing fibre alignment with increased drum collector speed . . . 102
5.5 Evaluation of electrospun PAN nanofibres . . . 103
5.5.1 Fibre diameter distribution and morphological uniformity of PAN nanofibres: the role of graphene . . . 106

6 Conclusion and future work 112

Appendices
.1 Fibres: mechanical performance . . . 118

Bibliography 125

1

Polyacrylonitrile (PAN) polymer in material science: challenges, innovations and advanced composite analysis

Global climate change is a growing concern, particularly regarding our reliance on fossil fuel energy and its impact on the environment. The transition from our current energy system to a low-carbon one is crucial for our future. Addressing this, there is a growing emphasis on pioneering electric energy solutions. This is evident in the shift of the automotive industry to electric vehicles, advancements in battery technology, and the evolution in wind energy production. These developments are key to achieving a sustainable future but also necessitate the innovation of advanced materials that can meet the evolving demands of these rapidly advancing sectors.

Carbon fibre, with its outstanding strength-to-weight ratio, is a leading material in meeting the demands of advanced sectors like automotive engineering and renewable energy. [1–3] As the primary precursor for carbon fibre production, polyacrylonitrile (PAN) fibres form the basis for manufacturing those carbon fibres. [4–7] The widespread use of PAN fibres is due to their unique properties, including high carbon content, easy processability, thermal stability, and mechanical strength. [3, 8] The key role of PAN fibres in carbon fibre production highlights the need for

continued research to optimise their properties and achieve further advancements in carbon fibre performance, supporting progress towards a carbon-neutral future.

1.1 The importance of PAN fibres

This section investigates the significant role of polyacrylonitrile (PAN) in advanced material applications, with a special focus on carbon fibre production. PAN is utilised in applications such as water purification, air filtration, and protective clothing, owing to its high chemical-thermal resistance, mechanical strength, and hydrophobic nature. [9]

Its most critical application, however, is centered on carbon fibre fabrication. Nowadays, about 90 % of carbon fibres on the market are based on polyacrylonitrile (PAN) as the precursor. [9] The molecular structure of PAN, characterised by a high concentration of carbon and nitrogen, is depicted in figure 1.1. The carbon backbone facilitates the development of an ordered and stable structure in carbon fibres. [10, 11]

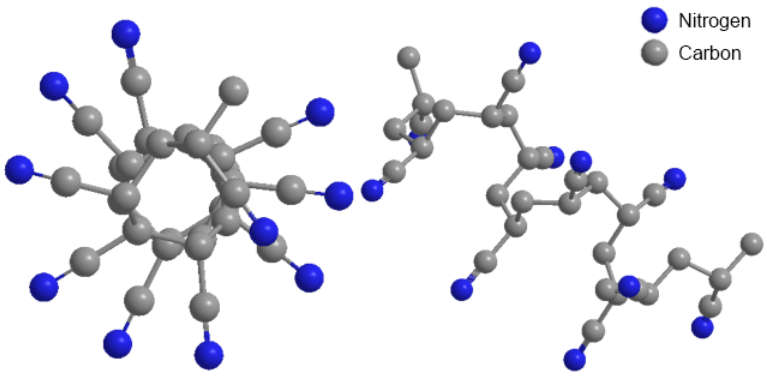

Figure 1.1: PAN-molecule: irregular helix structure because of the intramolecular repulsion between adjacent nitrile groups. The standard PAN polymer contains approximately 65 % C, 26 % N and 6 % H. The left image illustrates the front view, and the right image shows the side view. Hydrogen atoms have been excluded to enhance the visibility of the polymer structure. Created using ChemDraw software.

Consequently, in carbon fibre production, the quality of the PAN precursor fibre is critical as it is directly proportional to the resulting carbon fibre structure. [4–7] Through high-temperature carbonisation, the sp^3 hybridised carbon within stabilised PAN transforms into sp^2 hybridised six-membered carbon-only rings, which cluster into ordered structures, enhancing crystallinity and reducing defects along the fibre axis. [10, 12–15] The high carbon yield of PAN enhances

the structural integrity of carbon fibres, reflected in their lightweight nature, high strength, and resilience to thermal and elastic stresses. Hence, carbon fibres are at the forefront of material innovation, significantly impacting key sectors with their unparalleled strength-to-weight ratios. They have become indispensable across various high-performance materials industries, including aerospace, automotive, and renewable energy (figure 1.2). [1–3]

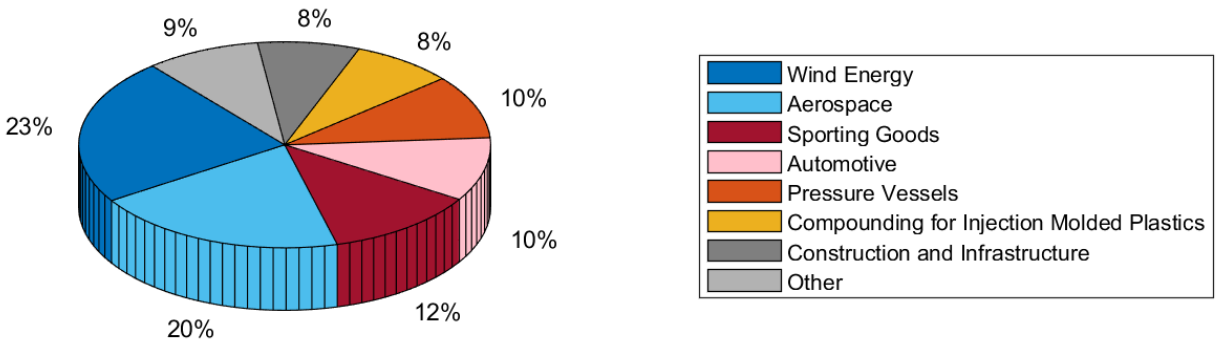

Figure 1.2: Distribution of carbon fibre consumption worldwide in 2020 by end-use market, as reported by Composites Manufacturing. [1]

A notable application is in the automotive industry, where carbon fibres are being utilised to develop low-emission and lightweight vehicles, effectively replacing traditional materials like aluminium due to their significantly higher strength-to-weight ratio, being up to 5–10 times stronger while also approximately 50 % lighter. [9, 16, 17] The broad adoption of carbon fibres across diverse industries directly correlates with the remarkable growth of the carbon fibre market. The market has grown from 33,000 metric tons in 2010 to an estimated 197,000 metric tons by 2023, indicating a compound annual growth rate of approximately 14.73% over 13 years. [18] In 2023, the carbon fibre industry has reached a market size of 3,821 million USD, projected to grow to 10,511 million USD by 2032. [19] As the carbon fibre market grows and diversifies, it underscores the heightened demand for research dedicated to advancing the characteristics of carbon fibres. The goal is to make these carbon fibres more cost-effective and versatile for various applications. [9, 16, 20]

1.2 Untapped potential and challenges of PAN-based carbon fibres

The superior mechanical properties of carbon fibres stem from the parallel alignment of crystallites along the fibre axis. Each crystallite consists of layers of two-dimensional carbon sheets arranged in a honeycomb structure, bound by weak van der Waals forces between the planes. The strong covalent bonding between carbon atoms provides significant rigidity and resistance to deformation. This structural arrangement results in a high Young modulus and specific strength. [21, 22]

Despite their outstanding features, commercially available carbon fibres have not yet tapped into their true potential. These fibres are predominantly produced through the wet-spinning method, which involves precursor extrusion into a coagulation bath to form fibres, followed by subsequent stretching and high-temperature conversion steps. Compared to the theoretical strength potential of 180 GPa for carbon fibres, the highest strength achieved to date by Toray Industries is 7 GPa, indicating significant room for advancement in this field. [23] The key limitations hindering their advancement are the low homogeneity, crystallinity, and crystallite size in the final product. [5–7]

Under commercial fabrication conditions, carbon fibres exhibit skin-core heterogeneity, marked by a two-phase structure of crystalline and amorphous regions, with a gradual reduction in the structural integrity and orientation of crystallites from the skin towards the core region. This structure is schematically illustrated in figure 1.3. [24, 25]

The crystallites within the carbon fibres can take on shapes from ribbons to sheets. Distinct features of these crystallites include their size, orientation relative to the fibre axis, and the physical separation from adjacent crystallites through elongated, needle-shaped voids or amorphous regions. Voids often form in the core due to the imperfect packing and irregular shapes of crystallites, which are typically bent, curled, and twisted in this region.

In conclusion, as highlighted earlier (figure 1.3), the low structural integrity of commercial carbon fibres presents a critical challenge. By achieving greater crystallinity, larger crystallite size, better axial alignment, and reduced porosity, the mechanical performance of the fibres can be markedly enhanced, ensuring greater reliability in advanced applications. These characteristics are largely determined by the manufacturing process, with the structure of PAN precursor fibres being one of the key factors in achieving these improvements, as discussed in the next section. [5, 6, 25, 26]

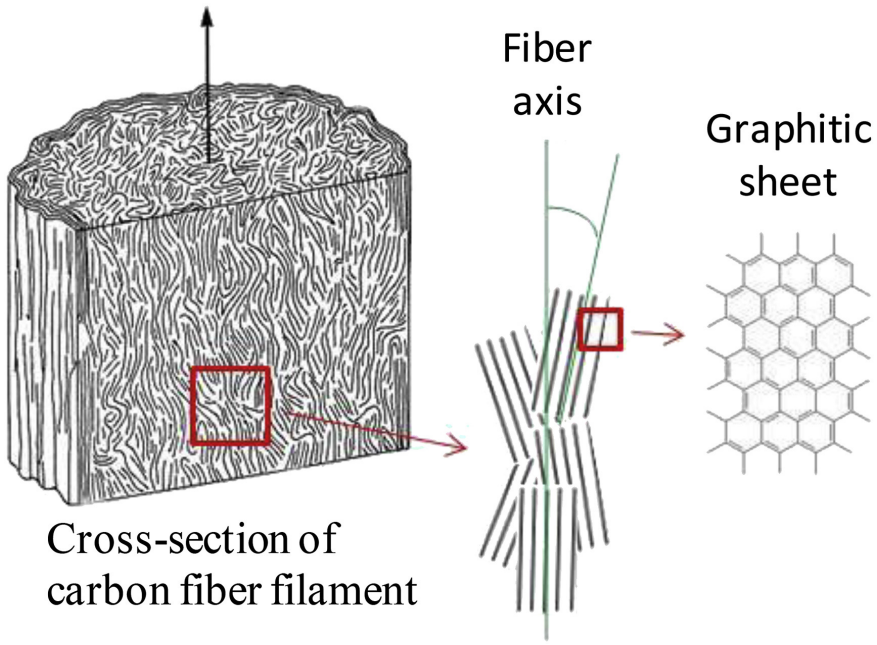

Figure 1.3: Schematic illustration of the skin-core heterogeneity in commercial carbon fibres: the two-phase structure of crystalline and amorphous regions, with a gradual reduction in crystallite integrity and orientation from the skin to the core. Adapted from Morgan *et al.* [24]

1.3 Electrospinning PAN precursor fibres: addressing structural challenges in carbon fibre production

The mechanical performance of carbon fibres is directly correlated with the degree of molecular alignment along the precursor fibre axis, as the structure of the precursor fibre directly impacts the resulting carbon fibre structure. When the molecular chains in the precursor fibre are highly aligned along the fibre axis, the resulting carbon fibres will exhibit similarly aligned crystallites. [5,27] Research indicates that fibres with smaller diameters exhibit increased molecular chain alignment, particularly along their edges. This phenomenon, known as the size confinement effect, enhances the overall degree of molecular chain order within the fibre, improving its mechanical performance. [28–31]

Several laboratory-methods exist for producing fibres with a reduced diameter, including electrospinning, template synthesis, and chemical vapor deposition (CVD). While template synthesis and CVD provide precise control over fibre dimensions, their high costs, complex setups, and scalability challenges limit their suitability for large-scale applications. [32] This research focuses on electrospinning, as it stands out as the most promising method for decreasing the diameter

of PAN-based precursor-fibres while addressing large-scale manufacturing requirements like cost-effectiveness, easy process control, and mass production capabilities. [32,33] Electrospinning utilises a high electric force to stretch a precursor solution through a spinneret into precursor-nanofibres. [2] However, while commercially available carbon microfibres demonstrate superior mechanical performance (Young modulus of $429\,GPa$ [34]) compared to electrospun carbon nanofibres (Young modulus of $262\,GPa$ [35]), these values are not directly comparable due to significant differences between industrial-scale and laboratory-scale production. [9] Industrial processes involve wet-spinning, multiple complex stretching steps to enhance molecular chain alignment, and carbonisation at temperatures exceeding 3000°C, far beyond what is achievable in most laboratory setups. As a result, performance data from commercial fibres are not directly comparable with lab-produced electrospun fibres. [5–7, 36]

To facilitate a comprehensive understanding of electrospun fibres, a comparative analysis of the mechanical performance of fibres across various chemical compositions from the literature has been conducted. Figure 1.4 presents this overview, illustrating that electrospun PAN-based carbon nanofibres outperform others in terms of tensile strength and Young modulus. In particular, the carbon nanofibres produced by Beese *et al.* have demonstrated exceptional performance, achieving a tensile strength of $7300\,MPa$ and a Young modulus of $262\,GPa$, as detailed in their study. [35] This remarkable performance is attributed to the ability of PAN to undergo carbonisation, forming stable sp^2 hybridised carbon structures that align in parallel along the fibre axis, enhancing mechanical properties. [21, 22]

Although PLLA and PI both achieve remarkable tensile strength and Young modulus in their non-carbonised forms due to factors like crystallinity and molecular orientation, their chemical structures hinder efficient carbonisation. [37–41] PLLA, with its aliphatic backbone of single carbon-carbon bonds, limits efficient carbonisation due to its thermal instability, low decomposition temperature, and inability to form stabilised intermediates and hexagonal carbon networks. [37–39, 42] While PI demonstrates strong mechanical performance and possesses an aromatic structure that is suitable for carbonisation, PAN remains the preferred precursor for carbon fibres due to its approximately 20 % higher carbonisation yield, facilitated by nitrile groups that promote efficient stabilisation and cyclisation, as well as its cost-effectiveness and well-established processing methods. [11, 40]

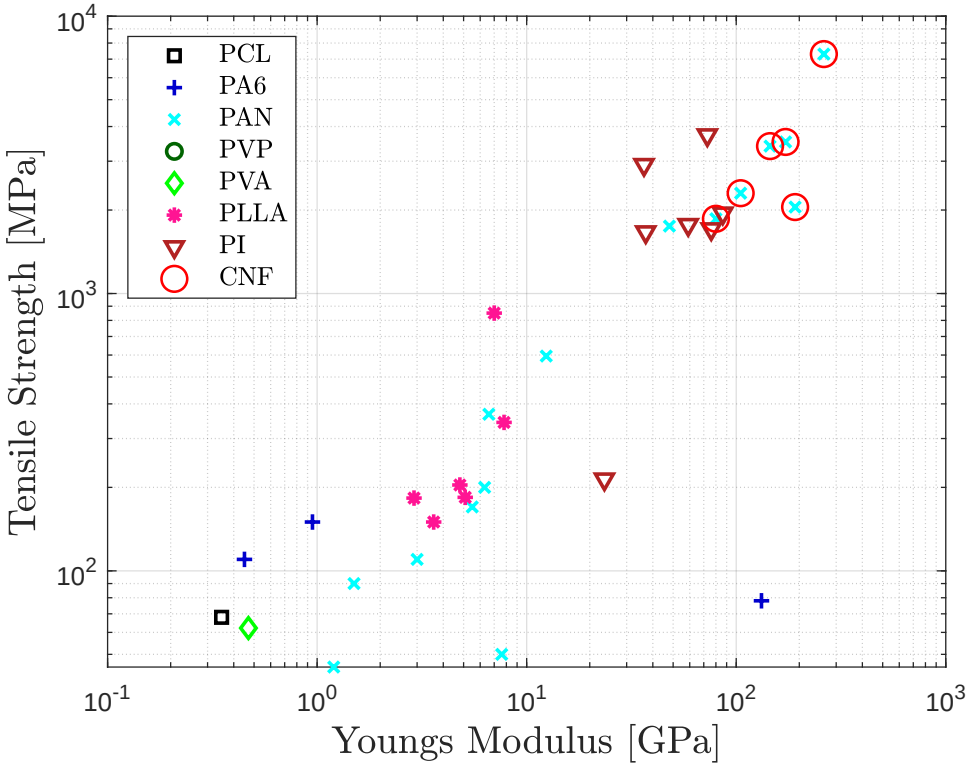

Figure 1.4: Relationship between Young modulus and tensile strength for PCL (polycaprolactone), PA6 (polyamide 6), PAN (polyacrylonitrile), PVP (polyvinylpyrrolidone), PVA (polyvinyl alcohol), PLLA (poly-L-lactic acid), and PI (polyimide). PAN, the only material represented in its carbonised form (circled in red), shows the highest performance after carbonisation, whereas PLLA and PI outperform non-carbonised PAN. Based on data from the literature; The corresponding parameters, sources and additional information can be found in appendix .1 (table .1).

The findings by Papkov *et al.*, which demonstrate that PAN nanofibres with a diameter of 100 nm can reach a modulus of up to 48 GPa, underscore the significance of the size confinement effect in promoting molecular chain alignment along the fibre axis. It is important to note that this particular diameter size and corresponding mechanical performance achievements are specifically observed in isolated nanofibres within the bundle. [31, 43]

The primary focus in this study is the optimisation of the electrospun PAN-precursor fibre, a material with a theoretical Young modulus ranging approximately from 35 to 55 GPa. [36] Through improved processing and molecular alignment, PAN-precursor fibres can be tailored to serve as a precursor for advanced carbon nanofibres that outperform other materials across a range of applications.

However, in electrospinning, the uniform stretching of the jet along the electric field is the primary

driver of molecular chain alignment. [5, 27, 44] Rapid solvent evaporation inhibits chain movement during fibre formation, yet residual solvent allows relaxation after deposition, leading to reduced orientation and compromising mechanical properties in the final nanofibres. [36, 44] This highlights the importance of developing additional mechanisms to increase the degree of molecular chain order within the precursor-fibre beyond what electrospinning alone can achieve.

1.3.1 Structural optimisation: integrating graphene to improve PAN-based precursor fibres

In the literature, the addition of second materials such as graphene and carbon nanotubes to nanofibres is explored, focusing on how this enhances their mechanical performance. The enhancement is driven by the confinement effect, as the second component is acting as a structural framework that limits the mobility of molecular chains, directing their alignment along the fibre axis. [7, 14, 31, 45] This alignment increases the overall structural organisation and performance of the nanofibres, as demonstrated by experimental findings from electrospinning and molecular orientation studies using polarised Raman spectroscopy, Infrared spectroscopy and X-ray diffraction. [7, 14, 31, 46] The strength of second materials like graphene and carbon nanotubes enhances the confinement effect by providing structural rigidity, guiding molecular organisation along the fibre axis. Simultaneously, their electrical conductivity supports the potential for advanced functionality in carbon fibre applications, such as batteries, supercapacitors, and other energy storage or transport systems. [2, 14, 33, 46, 47]

Despite carbon nanotubes having superior properties, such as a Young modulus of 1280 GPa and high electrical conductivity of $0.35 \cdot 10^5\, S/cm$ [48, 49], their high production costs and synthesis temperatures limit their suitability for large-scale industrial applications. [50] In contrast, graphene presents a more practical option for industrial applications due to its feasible and scalable production methods. [51, 52] The potential of graphene in enhancing polymers is not only recognised in academic research but also in its rapid market expansion. The value of graphene-enhanced polymers, which reached 69.9 million USD in 2017, is projected to grow to 315.6 million USD by 2023. This market trend highlights the growing importance of graphene and its role in material innovation and technology development. [53]

The focus, therefore, is on graphene, a promising candidate for enhancing the confinement effect due to its single-layer carbon atom structure arranged in a honeycomb lattice, which provides exceptional rigidity and enables efficient molecular chain alignment. [14, 46, 47] Its outstanding properties include a Young modulus of 1000 GPa [54–56] and ultra-high electrical conductivity of $1.00 \cdot 10^5\, S/cm$. [57, 58] The reason for the high electrical conductivity of graphene is that the carbon atoms are sp^2-hybridised (see figure 1.5). This hybridisation enables the π-electrons, part of the delocalised π-bonds, to form a cloud of electron density above and below the graphene plane. These π-electrons, resulting from the side-to-side overlap of unhybridised p-orbitals on adjacent carbon atoms, thereby facilitate efficient electron mobility. In contrast, the σ-bond electrons, formed by end-to-end orbital overlap, are localised between carbon atoms and do not contribute to conductivity. [59, 60]

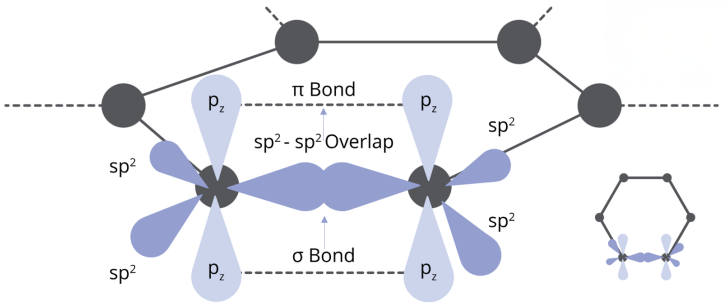

Figure 1.5: Visual depiction of the sp^2-hybridised carbon atoms in graphene, where individual π-bonds formed by p-orbital overlap combine to create a delocalised π-electron cloud that facilitates electron mobility. The σ-bond electrons remain localised between carbon atoms. Adapted from [60].

Despite the development of various graphene production techniques, many are inefficient in terms of quality and cost. Consequently, much of the graphene on the market fails to meet standard criteria, often containing more than 10 layers or significant defects. [61]

Chemical vapour deposition (CVD), for example, produces high-quality graphene but involves high costs and complex processes, which involve the pyrolysis of a carbon-atom precursor and subsequent graphene carbon-atom arrangement to form graphene on a substrate. [55, 62] In contrast, the Hummers' method, a process involving the chemical oxidation of graphite followed by reduction, offers scalability and cost-effectiveness but causes significant structural damage in the graphene produced. [55, 62, 63] To address these challenges, lab-based methods like

ultrasonication, shear-mixing, and electrochemical exfoliation have been explored. [51, 52] Shear-mixing, in particular, stands out as a scalable and efficient technique for producing low-defect, few-layer graphene at reduced costs, by exfoliating graphite in a solvent medium. [62, 64] This study, therefore, introduces a direct, in situ shear-mixing approach for graphene synthesis, integrated into the PAN fibre production process.

1.4 Innovative strategies for PAN nanofibre fabrication and graphene composite material evaluation

This section presents innovative strategies for the fabrication of PAN nanofibres and the evaluation of graphene composite materials. The focus lies on optimising PAN nanofibre production through electrospinning with in situ synthesised graphene and utilising thermogravimetric analysis as a simplified tool for assessing graphene quality in PAN polymer composties.

1.4.1 Optimising PAN nanofibre fabrication via electrospinning with in situ synthesised embedded graphene: a novel synthesis strategy

Building on the discussions and findings presented in earlier sections, this thesis introduces a novel approach for synthesising graphene-reinforced polyacrylonitrile (PAN) nanofibres with enhanced mechanical properties. The innovative aspect lies in the process, where low-defect graphene is synthesised in situ within a PAN and dimethylformamide (DMF) solution, which simultaneously acts as the precursor for PAN fibre production via electrospinning. The objective is to improve the mechanical performance of electrospun PAN fibres by increasing the degree of structural order along the fibre axis through graphene integration. To ensure this, the shear-mixing process is specifically designed to produce graphene rather than graphite. The single- or few-layer structure of graphene provides a higher specific surface area compared to graphite, enabling stronger interfacial interactions with the PAN matrix during fibre synthesis. Additionally, graphene hinders the relaxation of molecular chains in the PAN-DMF solution during electrospinning, promoting enhanced molecular alignment. [44] Achieving this effect requires high-quality graphene, as

defects or a multilayered structure reduce its interfacial interactions with the polymer matrix, thereby limiting its impact on fibre properties.

However, commercially available graphene often contains more than 10 layers, is contaminated, mislabeled, and exhibits a high defect density, resulting in lower quality standards and failing to meet the true definition of graphene. [61] Integrating graphene synthesis directly into the PAN-fibre production route addresses the challenges of commercially available graphene. This in-house process, validated in this study, produces low-defect graphene, ensuring consistent quality while offering a potentially scalable and cost-effective manufacturing solution.

Shear-mixing, not previously applied in this context, offers several advantages: it facilitates a uniform dispersion of graphene, while the presence of the PAN-polymer in the solution suppresses the aggregation and re-stacking of graphene. In detail, the polymer adsorbs onto the graphene surface through mechanisms such as charge transfer interactions or electrostatic forces, while the polymer chains create physical barriers, stabilising the graphene dispersion. [52, 65, 66]

According to literature, such as examples in [52] and [66], a polymer concentration of $\sim$1 wt.% is typically employed to achieve these results. In this study, much higher polymer concentrations, up to 9 wt.%, are investigated to assess the impact of varying polymer concentrations. Higher viscosity could increase shear forces, improving exfoliation efficiency and addressing the dispersion challenges arising from the small size and strong van der Waals interactions of nanomaterials. [36, 52, 67]

For example, Abdel-Mottaleb *et al.* dispersed 1 wt.% graphene oxide (GO) synthesised using the hummers' method, into a PAN+DMF solution. Despite a 28-hour dispersion process, SEM analysis (figure 1.6) reveals non-uniform fibre formation due to GO agglomeration. Abdel-Mottaleb *et al.* further demonstrated that fibre irregularities, including bead formation and variations in fibre diameter, become more pronounced with increasing GO content. [68]

Similarly, Khan *et al.* used graphene nanoplatelets with thicknesses ranging from 2-10 nm (>20 layers), where the quality as graphene is questionable given that graphene typically exhibits a thickness around $\sim$4 nm (approx. 10 layers). [69–71] Their dispersion process involves stirring the solution for 18 hours at 500 rpm and 40 °C. This approach resulted in uniform, bead-free fibres, likely due to the improved dispersion stability and reduced aggregation tendencies of nanoplatelets compared to GO. [70]

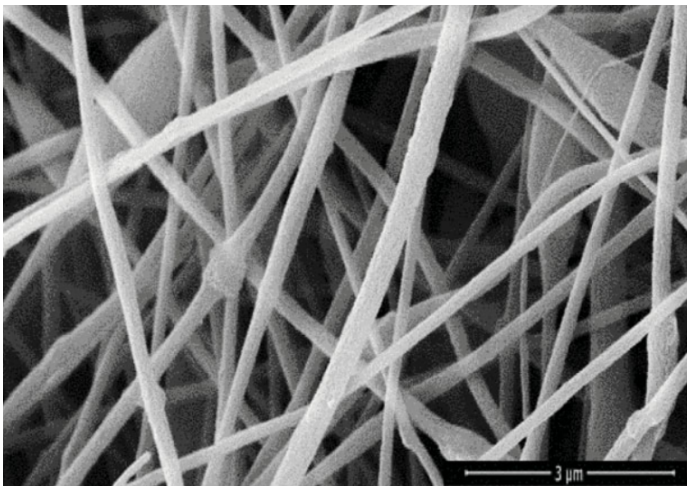

Figure 1.6: The SEM (Scanning Electron Microscopy) image illustrates the morphology of PAN/GO nanofibres, produced by dissolving 10 wt.% PAN in DMF and adding 1 wt.% GO. The solution is mechanically stirred at 35 °C for 24 hours, followed by 4 hours of sonication to ensure homogeneity. Electrospinning is performed at 25 kV with a 15 cm needle-collector distance and a 0.5 ml/h feed rate at a relative humidity of 30-40%. The SEM image shows non-uniform fibre formation, characterised by bead formation, which suggests the agglomeration of GO and challenges in maintaining a consistent dispersion within the solution. [68]

The in situ graphene synthesis within the fibre precursor solution, developed in this study and detailed in chapter 2, effectively overcomes the challenges of graphene quality and dispersion. This method results in uniform graphene-reinforced PAN fibres, as discussed in chapter 5.

1.4.2 Advanced thermogravimetric analysis as a non-conventional, rapid route for the evaluation of graphene-reinforced composites

In addition to the synthesis methods, this thesis places significant emphasis on analysing the yield and quality of graphene using thermogravimetric analysis (TGA). This advanced analysis is important for industrial applications, where efficient and reliable methods are needed to confirm the quality and composition of materials. While current standard characterisation techniques, such as Raman spectroscopy, atomic force microscopy, and x-ray photoelectron spectroscopy, provide comprehensive information on material properties, they offer only local data and require significant time and expertise. The processes often involve extensive sample preparation, repeated measurements for statistical relevance, and complex data interpretation, which can take several days. In contrast, TGA provides broader, bulk information with minimal operator involvement.

Once the sample is loaded, the process runs automatically, with measurement durations ranging from a few hours to half a day, depending on the required resolution. This makes TGA a more efficient and cost-effective quality control tool for industrial applications. [72–74] TGA is an analytical technique that measures the weight change of a material in response to a controlled heating process. This analysis provides valuable insights into the thermal stability and decomposition patterns of the studied material. [72–74]

In the literature, TGA is recently explored as a potential tool for characterising carbon-based materials, with the focus on distinguishing graphene from other carbon-based materials. [72,75–77] This research field investigates how differences in thermal decomposition behavior can be used to identify graphene. [72, 75–77] Building on this, the current work explores the potential of this analysis route for evaluating graphene-reinforced composites.

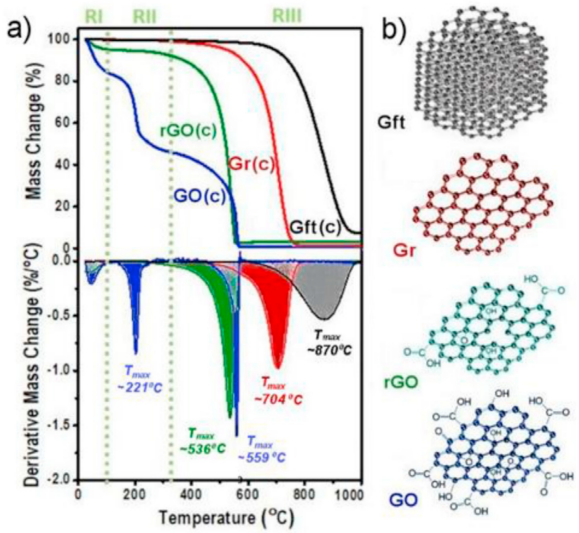

Figure 1.7: a) TGA curves and derivatives for graphene, graphene oxide (GO), reduced graphene oxide (rGO), and graphite, highlighting distinct thermal decomposition profiles. Graphite decomposes at ∼870 °C, while graphene decomposes at ∼704 °C due to fewer layers. GO exhibits three peaks (∼100 °C, ∼221 °C, ∼559 °C), whereas rGO shows two (∼100 °C, ∼536 °C) due to the removal of oxygen groups. b) Depicts material structures. Figure derived from Farivar *et al.* source [72]

For instance, Farivar *et al.* conduct a TGA study on graphene, graphene oxide (GO), reduced graphene oxide (rGO), and graphite, demonstrating that distinct thermal decomposition profiles can effectively differentiate these materials. The TGA results are presented in figure 1.7. The

research examines the decomposition range and the temperature of maximum mass change rate (Tmax), extracted from the first derivative of the TG curve. [72, 77]

Graphite, characterised by its strong honeycomb carbon lattice connected by van der Waals forces, decomposes at the highest temperature, with a single event occurring around 870 °C. In contrast, graphene, consisting of fewer than 10 layers, exhibits a lower decomposition peak around 704 °C. The lower thermal stability of graphene is attributed to its single-layer or few-layer structure, which results in a higher surface area-to-volume ratio. This increased surface exposure accelerates thermal degradation compared to the densely packed, three-dimensional stacked layers of graphite. [72, 77]

GO exhibits three distinct Tmax decomposition peaks: RI for moisture removal (∼100 °C), RII for the degradation of oxygen-containing functional groups and impurities (∼221 °C), and RIII for carbon framework decomposition at 559 °C. The carbon decomposition stage (RIII) involves the oxidation of carbon to form carbon dioxide (CO_2), represented by the reaction:

$$C + O_2 \rightarrow CO_2$$

[72, 77, 78]

In comparison, rGO shows only two peaks: RI for moisture removal (100 °C) and RIII for carbon decomposition (∼536 °C). The absence of the RII peak in rGO is attributed to the reduction process, which removes oxygen-containing functional groups that are responsible for intermediate decomposition events. [72] The lower thermal stability of GO stems from weaker interactions among graphene layers, attributed to oxygen-containing groups and a high defect density. The absence of the RII peak in rGO, resulting from the removal of oxygen groups, differentiates it from GO, while the similar RIII peak indicates that the reduction process does not fully restore the carbon network, possibly increasing defect density. [72, 77, 79]

This study analyses four different carbon allotrope variants. However, commercial graphene produced via various methods can vary significantly in terms of crystallinity, impurities, defects, lateral particle size, number of layers, and oxygen content. With over 20 scalable processes utilised by more than 500 companies globally, these four studied samples might not reflect all existing variations, potentially leading to gaps in the information required for this presented approach. To address this issue, recent efforts focus on developing a standardised experimental condition and protocol, as reviewed in [73]. A consistent standard would enable the comparability of data,

facilitating the development of universally applicable reference data library. However, Pei Lay Yap *et al.* emphasise that interpreting TGA data from literature requires caution, as deviations caused by environmental factors and human error are the primary sources of inconsistent results. [72–74] Accordingly, this work investigates the effectiveness of TGA in assessing the quality and quantity of graphene in polymer composites by analysing and deconvoluting the first derivative of the weight-loss curve. The first derivative peaks, representing the maximum rate of weight change, are used to identify graphene-specific decomposition events, aided by reference spectra generated in this study. The contribution of graphene to the overall weight loss is then utilised to determine its concentration (see chapter 4).

Farivar *et al.* report a detection limit of 5% for carbon-allotrope composite materials. [72] This study extends this investigation to polymer composites, and examines the decomposition profile of graphene produced by shear-mixing fits within these findings. Farivar *et al.* also demonstrate a direct linear correlation between graphene particle size and decomposition temperature. Larger graphene particles exhibit higher decomposition temperature values, attributed to slower combustion kinetics due to their lower surface area-to-volume ratio. [77] Building on this work, the present study examines whether this relationship can be utilised to assess the quality of synthesis processes, such as shear-mixing, that produce particles of varying sizes.

In conclusion, TGA has the potential to greatly simplify material characterisation, offering a straightforward way to ensure quality and properties without separating material components — a significant advantage in industrial contexts.

1.5 Thesis structure and chapter overview

To guide the reader through this unconventional thesis structure, this section summarises the content and rationale behind the organisation of the subsequent chapters. By closely integrating theory and practice within each chapter, the thesis ensures a logical flow for the reader while addressing elements such as characterisation techniques, synthesis processes, and complex analyses.

Chapter 2 introduces the synthesis of graphene in PAN-based solutions, combining theoretical principles with their implementation through shear-mixing, ultrasonication, and centrifugation. Chapter 3 focuses on graphene characterisation, utilising Raman spectroscopy, AFM, and UV-Vis

spectroscopy to provide an in-depth quality assessment. Theoretical principles and literature findings, such as the correlation between the 2D peak shape and graphene layer thickness, are directly applied during Raman spectroscopy analysis, demonstrating a seamless transition from theory to practical application. Chapter 4 evaluates the use of thermogravimetric analysis (TGA) as a bulk graphene characterisation tool, advancing the method and testing its reliability and functionality. Finally, chapter 5 demonstrates the successful fabrication of graphene-reinforced PAN fibres, applying the research findings into a practical application. The conclusion (chapter 6) provides a comprehensive overview of the thesis findings, addressing the achieved results and identifying opportunities for advancing research in graphene synthesis, characterisation techniques, and fibre performance optimisation.

2

Direct exfoliation of graphene in PAN-based solutions: a novel fibre-synthesis precursor

This study develops an innovative fibre precursor synthesis method to produce fibres from polyacrylonitrile (PAN) dissolved in dimethylformamide (DMF), incorporating well-dispersed, low-defect, few-layer graphene. The synthesis method, depicted in figure 2.1, consists of shear-mixing, ultrasonication, and centrifugation, which exfoliate graphite into few-layer graphene within the PAN-DMF solution.

This study adopts the liquid-phase exfoliation approach described by Kai Ling Ng *et al.*, which focuses on evaluating the exfoliation efficiency and dispersibility of graphene in various green solvents as sustainable alternatives to NMP. [82] In contrast, this work uses DMF as the solvent and introduces PAN polymer concentrations of up to 9 wt.%. These modifications alter subsequent processing steps, including centrifugation speed and duration. The goal of this research is to tailor the exfoliation process so that the polymer solution containing exfoliated graphene can be utilised for electrospinning, while investigating the influence and limitations of polymer addition on the exfoliation process. By integrating these findings, this approach enables a novel in situ synthesis of few-layer, low-defect graphene within the fibre precursor, optimising the fibre production process.

For the shear-mixing of graphite, a base solution is prepared using polyacrylonitrile (Sigma-Aldrich, CAS: 25014-41-9, MW: 150,000) dissolved in N,N-dimethylformamide (Thermo Fisher Scientific, CAS: 68-12-2).

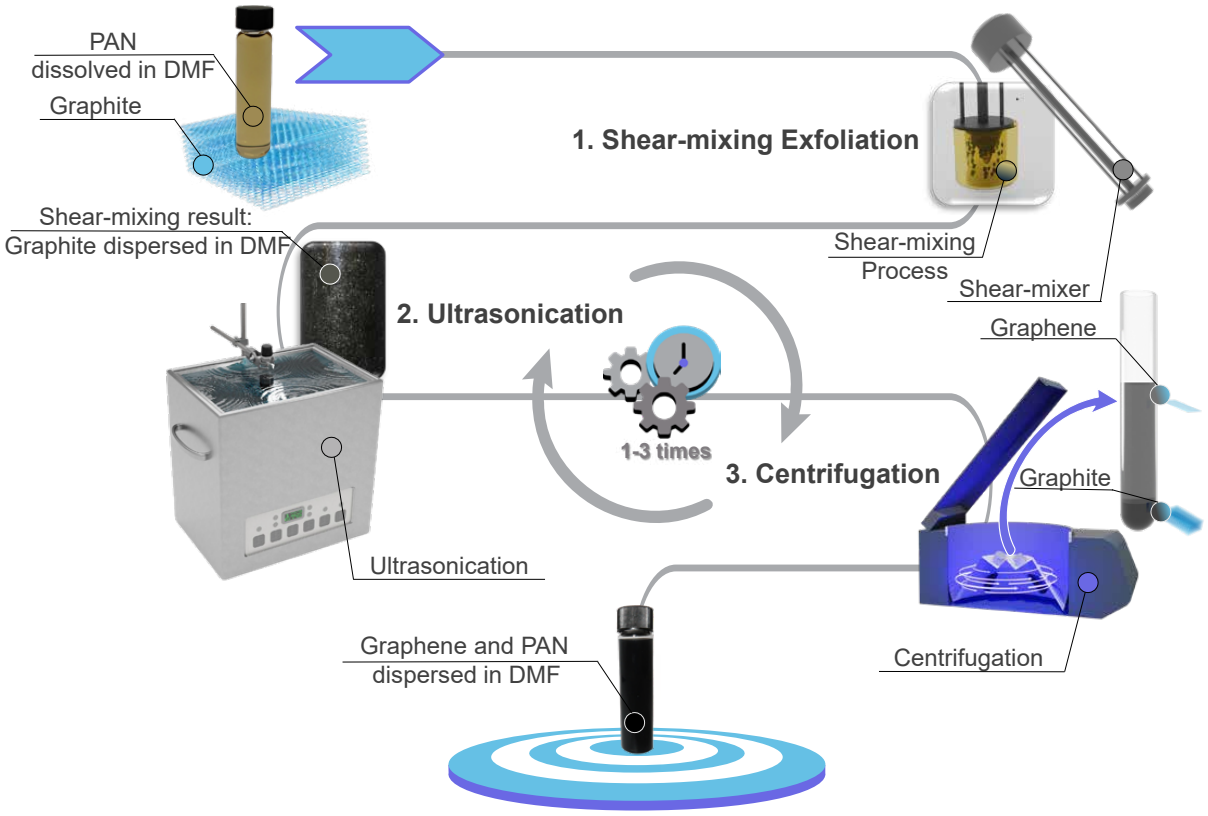

Figure 2.1: The synthesis process for direct exfoliation of graphene in PAN-based solutions to create a novel fibre-synthesis precursor involves the following steps: 1) Exfoliation of graphite in the polymer solution produces well-dispersed, low-defect, few-layer graphene. 2) A 2-minute ultrasonic treatment further reduces the thickness of graphene flakes in the shear-mixed solution, completing any incomplete exfoliation. 3) Post-ultrasonication, graphene is separated from graphite, and the supernatant is utilised in subsequent steps. Steps 2 and 3 are repeated 1-3 times, depending on the solution's viscosity, with higher viscosity requiring additional iterations. The figure is generated using the Blender software.

DMF is an effective solvent for graphene exfoliation, as its surface tension of 37.1 mJ/m^2 [80] is similar to that of graphene, which ranges from 35-60 mJ/m^2. [81] Therefore, it promotes the intercalation of solvent between graphene layers, lowering the van der Waals energy barrier for an effective exfoliation process. Furthermore, the incorporation of PAN polymer into the solution aids in preventing graphene restacking through electrostatic repulsion and steric hindrance. PAN also reduces the surface tension of graphene. Consequently, the surface shows improved wettability. [62, 64, 80]

Graphite platelets (Sigma-Aldrich, CAS: 7782-42-5), characterised by a lateral size of 150 μm and low defect density, are chosen for this experiment. Kai Ling Ng *et al.* indicate that larger

lateral graphite sizes provide a greater surface area for interaction, facilitating solvent penetration and exposing the material more effectively to shear forces generated parallel to the direction of motion between the rotor and stator, thereby enhancing the efficiency of the shear exfoliation process. The low defect density and high crystallinity of the graphite platelets also contribute to efficient exfoliation and the production of graphene with fewer imperfections. [82]

2.1 Shear-mixing: process overview of preliminary exfoliation and experimental parameters

The shear-mixing of graphite-PAN solution produces stably, dispersed graphene with varying sizes and layer thicknesses. 3.75 gr graphite is shear-mixed in 150 ml PAN solution at 5000 RPM for 4 hours to produce a stable graphene dispersion. During the shear-mixing, the total solution volume is kept steady at 150 ml by adding DMF as needed. The solution volume remains stable due to the high boiling point of DMF, with only a negligible amount added to maintain consistency and preserve the polymer concentration. A GREAVES shear mixer, serial number 05558557701023, is utilised.

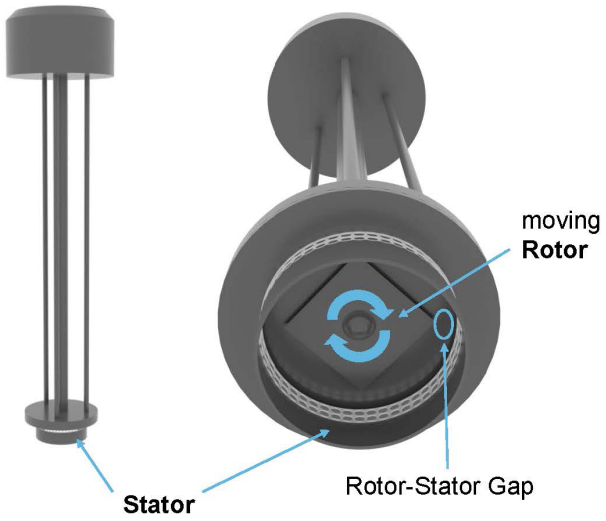

Figure 2.2: Shear-mixer design (synthesis process step 1): graphite is exfoliated in a PAN solution using a shear mixer, resulting in graphene with diverse sizes and layer thicknesses. The shear mixer, consisting of a rotor and a stator separated by a narrow gap, induces fluid flow that creates shear forces, effectively exfoliating graphene layers from the graphite. The left image presents the front view, and the right image shows the bottom view, illustrating the structural configuration of the shear-mixer. Cavitation and collisions between graphite flakes and the mixer further enhance the exfoliation process. The figure is generated using the Blender software.

The shear mixer consists of a rotor and a stator with a narrow gap, as depicted in figure 2.2: High-speed rotor rotation induces rapid fluid flow, generating a velocity gradient between the rotor and stator, creating shear forces that exfoliate graphene layers from graphite. Higher viscosity results in greater shear forces because the fluid resists deformation more strongly. In a rotor-stator system, the velocity gradient stays constant at a given speed, but higher viscosity requires greater

force to maintain the flow rate due to increased resistance to deformation. Hence, viscosity significantly influences the shear forces and determines the efficiency of the shear-mixing process. As demonstrated in figure 2.3, the amount of the PAN in the solution has a strong impact on the viscosity. Viscosity was measured with a viscometer by applying shear stress and monitoring flow characteristics across shear speeds of 45 to 120 RPM. Increasing PAN concentrations (3 %, 5 %, and 10 % by weight in DMF) correspond to an increase in viscosity.

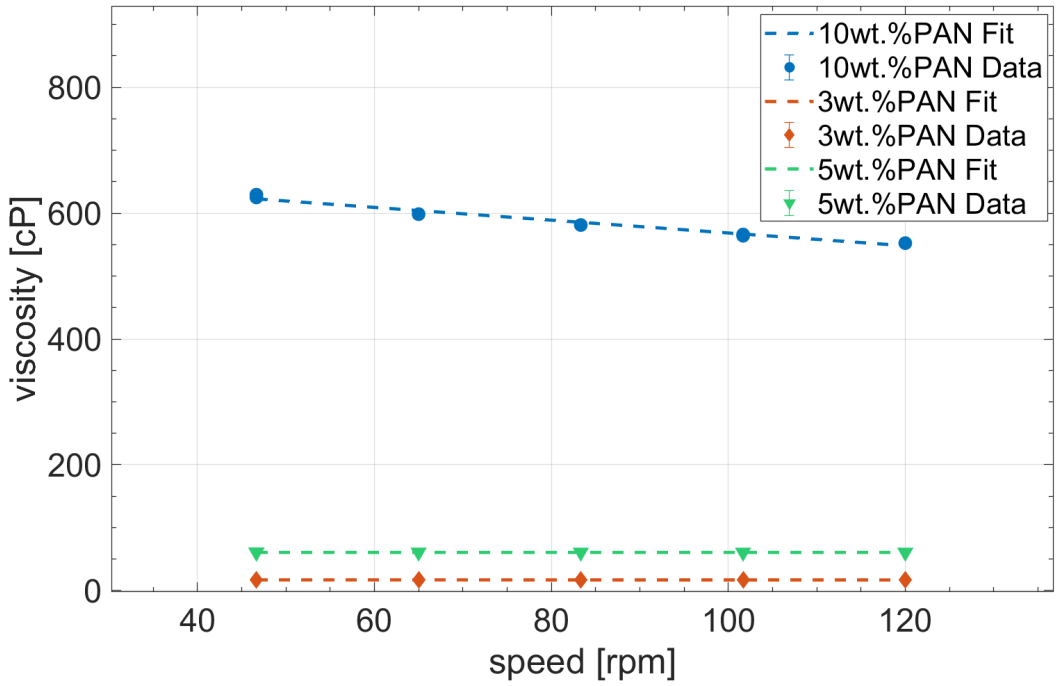

Figure 2.3: Viscosity vs. shear speed for PAN/DMF solutions. Viscosity is the measure of a fluid resistance to flow, determined by the force required to move one layer of fluid relative to another. A viscometer determines viscosity by applying shear stress to the fluid and measuring its flow characteristics. [83] This graph compares the viscosity of polyacrylonitrile (PAN) solutions at concentrations of 3 %, 5 %, and 10 % by weight in DMF, plotted against varying shear speeds. The data reveal that viscosity increases with higher PAN weight percentages, enhancing shear forces and consequently improving the shear exfoliation process. Measurements were performed using a DV2T Viscometer (AMETEK Brookfield), with shear speeds ranging from 45 to 120 RPM, with special thanks to Ryan Schofield for conducting the experiment. The results are based on a single set of measurements.

In addition, cavitation occurs due to pressure pulsations resulting from rapid geometrical and velocity changes, particularly when fluid flows out of the stator holes. [62, 64, 80] The collisions between graphite flakes and the shear mixer also contribute to the exfoliation process. [62, 64, 80]

2.2 Ultrasonication: further exfoliation and experimental details

As a subsequent step, a brief 2-minute ultrasonication is applied to the shear-mixed solution to further reduce the number of graphene layers through liquid exfoliation. [62, 82, 84] Hence, ultrasonication acts as a secondary exfolation step (figure 2.4). This technique involves the propagation of high-frequency sound waves into the solution, causing rapid oscillations in pressure. These oscillations form microbubbles that implode with decreasing pressure, creating shockwaves, which interact with the remaining graphite/multi-layer graphene remaining in the shear-mixed solution. While this method may not be highly efficient in isolation, it is instrumental in completing any incomplete exfoliation, ensuring a more thorough separation of graphene layers. [62, 84] The Ultrawave QS12 equipment is employed for ultrasonication.

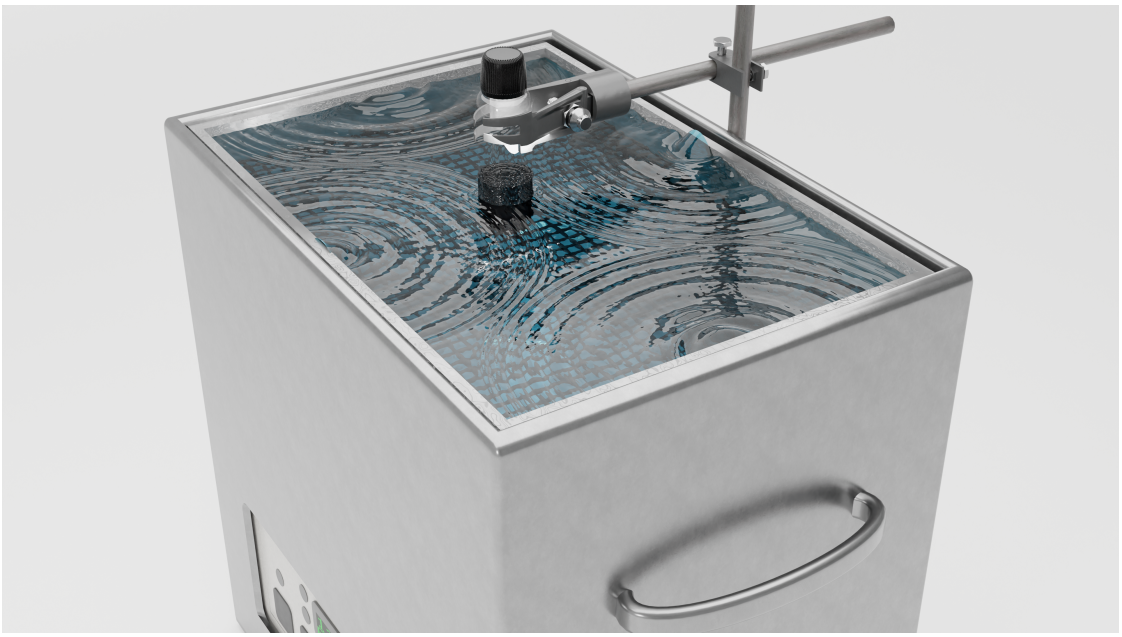

Figure 2.4: Synthesis process step 2: a 2-minute ultrasonication follows shear-mixing to further reduce graphene size. High-frequency sound waves create pressure oscillations, forming microbubbles that implode, producing shockwaves. These shockwaves interact with remaining graphite or multi-layer graphene, completing exfoliation and ensuring thorough graphene layer separation. The figure is generated using the Blender software.

Figure 2.5 illustrates the change in solution colour observed before and after the shear-mixing process. Initially clear and yellow, the solution transforms to a dinstinct black colour with a

metallic shine. The metallic shine indicates residual graphite particles. This underscores the necessity of employing centrifugation to remove these particles from the solution. Notably, the appearance of the solution remains consistent after both shear-mixing and the ultrasonication step.

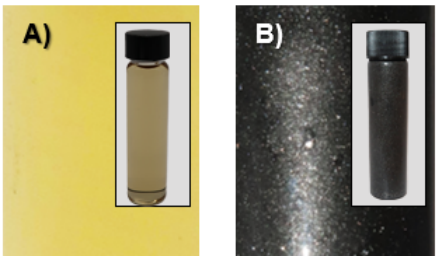

Figure 2.5: Solution colour: A) Pre-shear-mixing: clear, yellow solution. B) Post-shear-mixing: black with metallic shine, indicating residual graphite and the necessity for centrifugation. The images were captured using a digital camera under controlled lighting conditions in a light box to ensure uniform illumination and minimise reflections.

2.3 Centrifugation: separation process and detailed experimental parameters

In this study, centrifugation is conducted using an angular rotor (Universal 320, Hettich), as shown in figure 2.6.

The process parameters, including centrifugation time and speed, are adjusted based on the viscosity of the PAN+graphene+graphite solution. The centrifugation process involves high-speed rotation of the solution around a fixed axis, relying on the centrifugal force F_c that acts perpendicularly to the axis, inducing centripetal acceleration onto the solution, as detailed in equation 2.1. In this equation, the variable m represents the mass in [kg], ω the angular velocity in [rad/s], d the distance of the particle from the axis of rotation in [m]. [85–87]

$$F_c = m \cdot \omega^2 \cdot d \tag{2.1}$$

During centrifugation, the heavier particles in the solution migrate outward and form a sediment, while lighter particles move towards the top, forming the supernatant. The supernatant, which generally entails the top two-thirds of the centrifuged solution, is decanted. The pitch-black colour

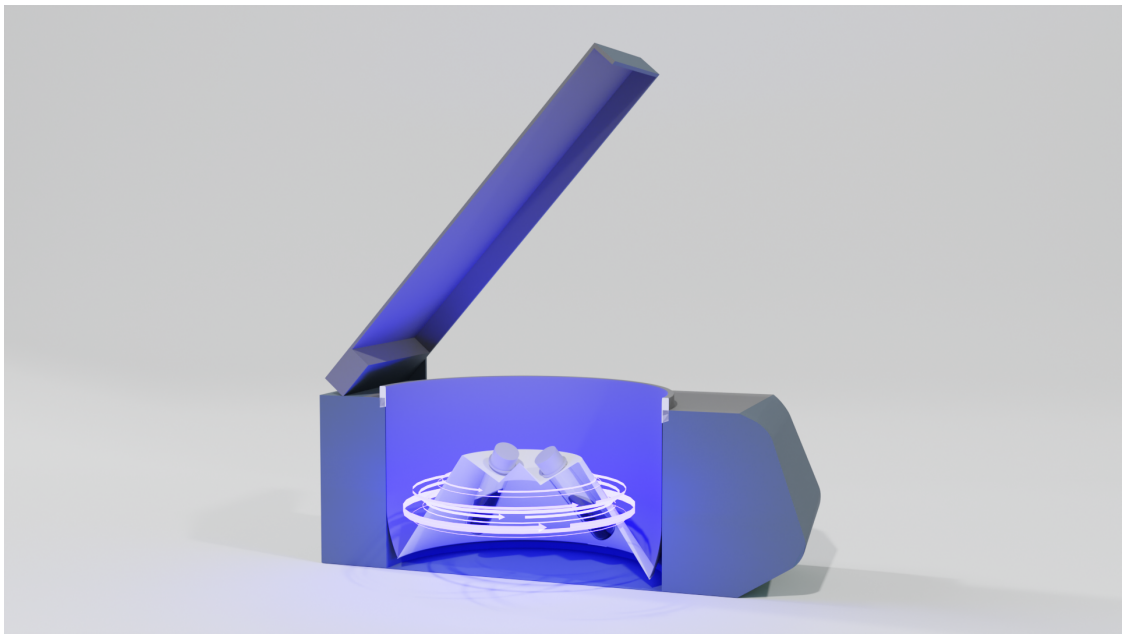

Figure 2.6: Synthesis process step 3) Centrifugation - graphene is separated from graphite, with the supernatant being utilised in subsequent steps. The centrifuge speed, typically set between 500 and 4000 RPM, determines the concentration and quality of the graphene. A schematic of an angular rotor centrifuge is provided, generated using Blender software.

of the supernatant is indicative of successful graphite removal, as depicted in figure 2.7. This colour change serves as a visual confirmation of the effectiveness of the centrifugation separation process.

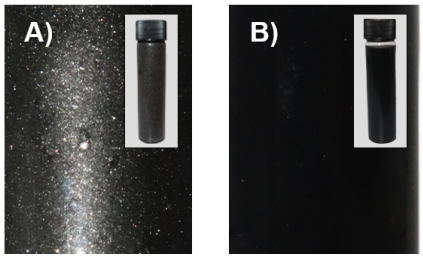

Figure 2.7: Solution colour: A) Post-shear-mixing: black with metallic shine, indicating residual graphite. B) Post-centrifugation: pitch black, marking the removal of graphite. The colour change from A) to B) visually indicates the successful completion of the centrifugation separation process. The images were captured using a digital camera under controlled lighting conditions in a light box to ensure uniform illumination and minimise reflections.

The separation force generated during this process is dependent on the operational speed of the centrifuge, quantified in revolutions per minute (RPM) [85, 87–89]:

$$\omega\,[\text{rad/s}] = \frac{2\pi}{60} \cdot RPM\,[\text{rev/min}] \tag{2.2}$$

At higher RPMs, the increased centrifugal force causes graphite particles and larger, multilayer graphene flakes to sediment more effectively due to their greater mass. Smaller, thinner graphene flakes remain in the supernatant as they sediment more slowly. This process reduces the average thickness of the graphene layers in the supernatant and removes unexfoliated graphite and thicker flakes from the dispersion. Typically, centrifuging at 500 RPM is sufficient to effectively separate the few-layered graphene phase in solvent dispersions. However, speeds ranging from 500 to 4000 RPM can generally be employed for graphene separation, depending on the specific requirements of the spearation process. It is important to consider that the viscosity of the solution and the density of the material significantly impact the effectiveness of centrifugation. Higher viscosities and material densities require increased centrifugal speeds for effective graphene separation. [80,90,91] Therefore, centrifugation parameters vary with the PAN polymer concentrations tested.

2.3.1 Centrifugation: experimental parameters and remarks

The RPM and duration of centrifugation are critical parameters that must be adjusted based on these specific factors, as detailed in table 2.1. Table 2.1 presents the modified centrifugation conditions for different polymer concentrations.

The number of centrifugation iterations is determined by a visual indicator, as explored in figure 2.7. When the solution appears pitch black, no further centrifugation of the supernatant is required, indicating that the process is complete. The polymer solution transitions from yellow to black due to the introduction of graphene, which dominates the optical properties of the material through its strong light absorption. When too much graphene is removed during centrifugation, the solution becomes less opaque, resulting in a lighter or more transparent black tone.

As shown in table 2.1, an increase in polymer concentration, and therefore viscosity, necessitates a greater number of centrifugation steps and higher RPM. This relationship is confirmed and visually represented in figure 2.3. Centrifugation speed is maintained at the lowest possible value to preserve graphene concentration, with an incremental increase of 500 RPM in each iteration.

Table 2.1: Step 3 of the precursor synthesis process, centrifugation parameters are adjusted for different PAN polymer concentrations. The parameters include PAN polymer concentration, time duration, number of iterations, and corresponding applied speed, with additional remarks provided for each experimental series. PAN polymer concentrations ranging from 3 wt.% to 6 wt.% are suitable for producing exfoliated graphene and can serve as precursors for fibre production via electrospinning. The 6 wt.% concentration is determined to be the most effective, as its higher viscosity produces the maximum shear forces required for optimal graphite exfoliation.

Polymer Concentration [wt.%]	Duration [min]	Iterations	Speed [RPM]	Remarks
0	60	1 2	500 500	Dispersibility is low, after standing sedimentation.
3	90	1 2 3 4	1500 1500 1500 2000	Too liquid for electrospinning: low solution viscosity, outside the optimal electrospinning range, produces non-uniform fibres with beads (example: figure 5.6). Explanation see section 5.5.
4	90	1 2 3 4	1500 1500 1500 2000	Suitable for electrospinning: viscosity near the optimal electrospinning range; see section 5.5 for fibre production details.
5	90	1 2 3 4	1500 1500 1500 2000	Suitable for electrospinning: viscosity is nearly within the optimal electrospinning range (see section 5.5 for explanation).
6	90	1 2 3 4 5	2000 2500 2500 3000 3000	Optimal for electrospinning: viscosity within the optimal window (see section 5.5 for details).
7	90	6 7 8 9	3000 3500 4000 4000	Approaching the centrifuge speed limit, a viscosity threshold is reached, preventing complete separation of graphite and graphene. While the viscosity falls within the electrospinning range, this condition is excluded due to incomplete separation.
8	/	/	/	Too viscous, max centrifugation force too low.
9	/	/	/	Too viscous, max centrifugation force too low.
10	/	/	/	Too viscous, max centrifugation force too low.

The used centrifugation duration, speeds and iteration numbers are detailed in the table 2.1 (columns 'Duration', 'Iterations' & 'Speed'). Prior to centrifugation, an ultrasonication step is consistently implemented and repeated in parallel with the number of centrifugation steps.
Table 2.1 shows that a 6 wt.% PAN solution is the maximum usable concentration in the PAN fibre precursor synthesis process, providing the highest viscosity under the tested conditions. This concentration is utilised for subsequent characterisation and adopted as the standard solution for electrospinning, as it has the highest viscosity and generates the maximum shear forces required for optimal exfoliated-graphene production and achieves sufficient viscosity for electrospinning (see section 5.5).
However, for centrifugation in this series of experiments, as depicted in figure 2.6, an angular rotor (Universal 320, Hettich) is used. This fixed-angle orientation of the angular rotor results in diagonal sediment formation at the bottom end and along the inner outer wall of the test tubes. When considering alternative methods, utilising a swinging-bucket rotor, which rotates horizontally, the number of necessary centrifugation runs is reduced by 1-2 times (tested on 3wt.% and 4 wt.% PAN-based solution). The horizontal position during rotation allows the centrifugal force (F_c) to act along the entire length of the tube, resulting in sediment accumulation at the end of the tube. Although not employed in these experiments, the swinging-bucket rotor could improve outcomes by achieving a clearer separation between sediment and supernatant and reducing the number of centrifugation iterations needed. [92]

2.4 Application of the graphene-PAN polymer precursor in electrospinning

The shear exfoliation of graphite directly within the PAN polymer solution, as outlined in this chapter, produces a graphene-reinforced PAN precursor. This precursor is utilised in the electrospinning processes. Chapter 5 details the methodologies and results of applying this precursor in electrospinning. Chapters 3 and 4 focus on the characterisation and analysis of shear-exfoliated graphene.

3

Standard characterisation and analysis of shear-exfoliated graphene

Section 2.2 demonstrates that shear-mixing followed by centrifugation changes the colour of the solution from yellow to black, suggesting the formation of graphene. To confirm this, further characterisation is necessary, including Raman spectroscopy, atomic force microscopy (AFM), and ultraviolet-visible (UV-Vis) absorption characterisation.

3.1 Sample preparation for characterisation: polymer removal using vacuum filtration

For accurate characterisation of graphene, it is essential to remove the influence of the PAN polymer from the measurements. This step ensures that PAN does not mask or modify the results, establishing precise evaluation of the graphene properties. Employing vacuum filtration with a 0.22 μm PTFE filter has been instrumental in facilitating this required separation of polymer from graphene. Vacuum filtration is selected for its chemical compatibility, as the PTFE filter resists solvents like DMF without degradation, ensuring effective and reliable graphene-polymer separation. This process is depicted schematically in figure 3.1, where the graphene-polymer mixture, diluted in DMF at a 1:10 ratio, is passed through the filter under vacuum conditions, effectively trapping the graphene while allowing the polymer to pass through. Installed in-line

after the suction flask, which collects the filtered liquid, a cold trap condenses DMF vapours to prevent damage to the vacuum pump.

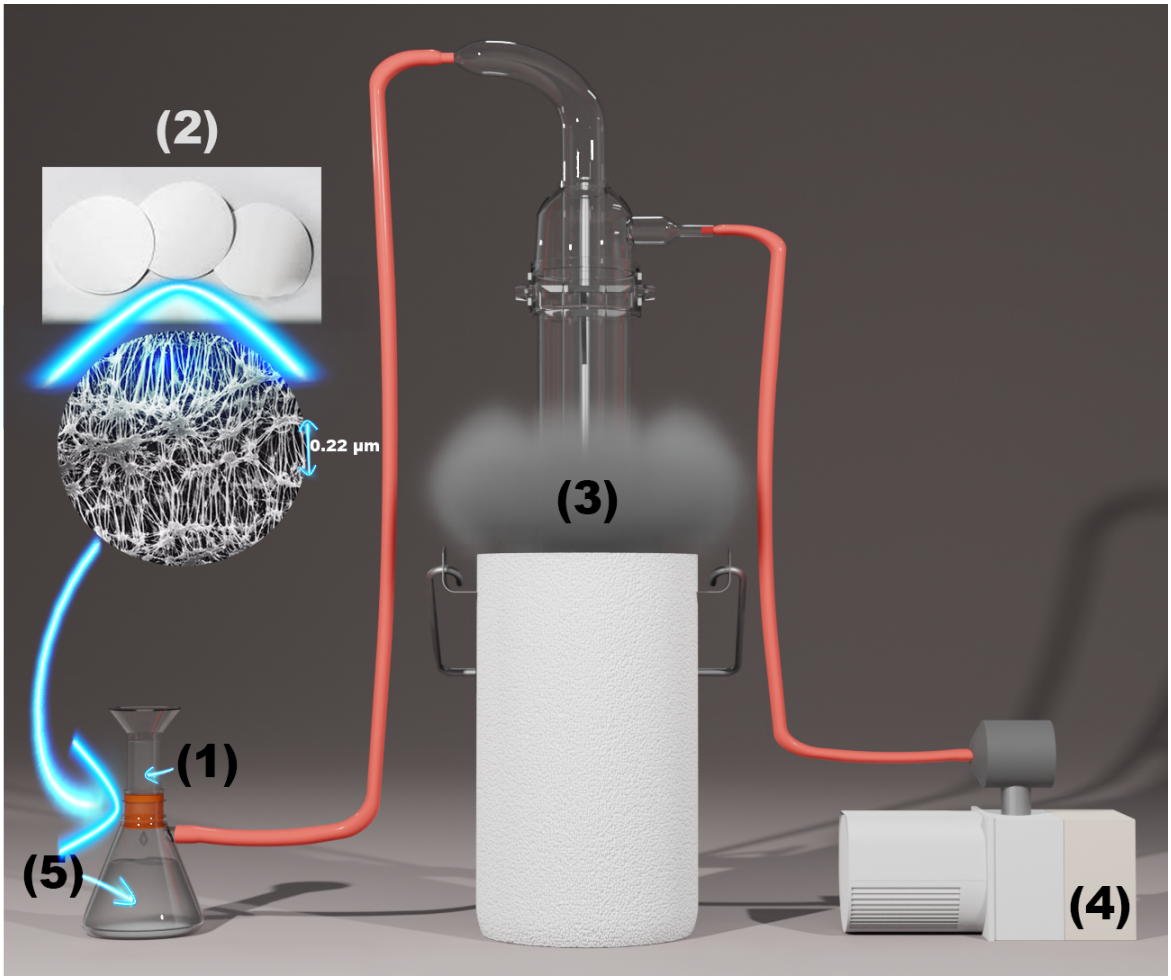

Figure 3.1: Schematic representation of the vacuum filtration process for graphene extraction from a PAN polymer+DMF solution. In this method, the graphene-PAN polymer dissolved in DMF is further diluted in DMF to a ratio of 1:10 (1). The diluted solution is then passed through a 0.22 μm PTFE filter (2) under vacuum. ((2) also depicts the filter and its scanning electron microscope imagery, revealing the pore morphology. [93]) The vacuum creates a pressure gradient that draws the liquid through the filter, trapping the graphene while allowing the polymer+DMF to pass through. To protect the vacuum pump (4) from DMF+PAN, a cold trap containing liquid nitrogen (3) is installed in-line after the suction flask (5) to condense vapours before they reach the pump. This setup ensures efficient filtration and protection of the vacuum system, facilitating graphene isolation and characterisation.

For Raman spectroscopy analysis (section 3.2), the filtered graphene is transferred onto adhesive copper foil. For atomic force microscopy (AFM) analysis (section 3.3), graphene is dispersed in 10 mL of isopropanol (IPA) by subjecting the filter with the deposited graphene to 5 h of ultrasonication. Subsequently, three droplets are placed on a silicon wafer for AFM

characterisation. The dilution is benefical for making the graphene sample coverage on the wafer dense, but not aggregating.

3.2 Quality assessment of graphene through Raman spectroscopic analysis

Raman spectroscopy serves two key purposes: to validate the successful separation of PAN and graphene via filtration, as detailed in section 3.1, and assessing the quality of the synthesised graphene. Raman spectroscopy provides crucial insights into the quality and type of graphitic materials through the peak shape, intensity and position in the spectrum. The spectrum is determined by measuring the energy shift in photons inelastically scattered by phonons, reflecting changes in the vibrational states of the material. [94–96] The goal of this study is to create graphene with 10 layers or fewer, since materials with more layers are not considered graphene, addressing the typical issue found in commercial graphene products. [61]

3.2.1 Benchmarking graphene quality: Raman spectra insights from literature review

A comparative study of Raman spectra peak characteristics from graphene and graphite, as well as commercially produced graphene via the hummers' method and CVD provides essential information for evaluating the compositional and quality differences of the studied samples.

Comparative analysis: graphite vs. graphene

Figure 3.2 presents the Raman spectra of graphene and graphite. Notable peaks include the G peak at $1580\,\mathrm{cm}^{-1}$ and the 2D peak at $2700\,\mathrm{cm}^{-1}$, which are the most intense features, providing essential insights into the material characteristics.

The G peak in Raman spectroscopy, occurring around $1580\,\mathrm{cm}^{-1}$ for graphene and graphite, reflects the in-plane bond stretching mode of sp^2-bonded carbon atoms. This peak is characterised by a phonon mode with two distinct vibrational modes of equal energy (doubly degenerate phonon mode) occurring within the plane of the graphene lattice.

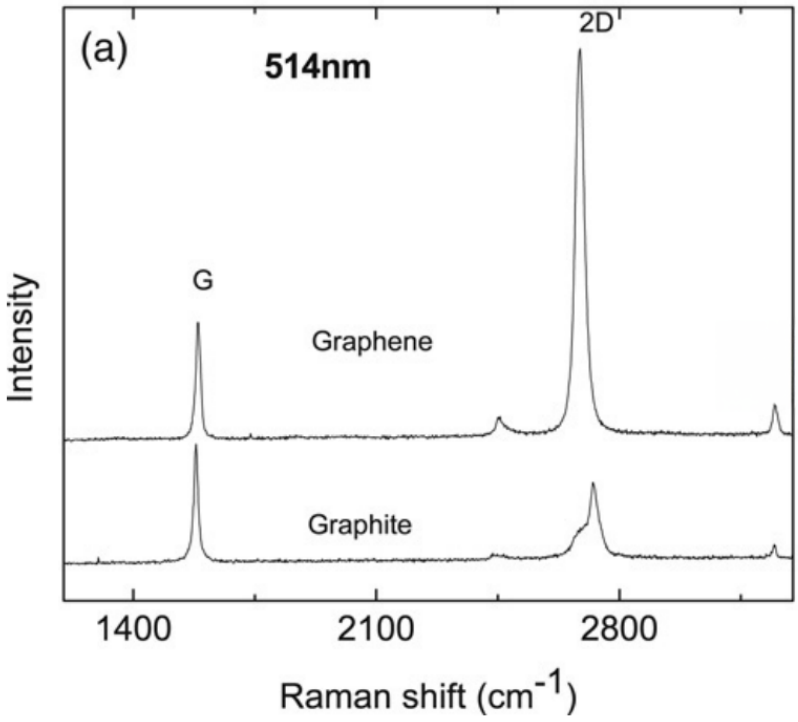

Figure 3.2: Comparison of Raman spectra of graphene and graphite at 514 nm excitation. The spectra show the G peak at 1580 cm^{-1} and the 2D peak at 2700 cm^{-1}. The 2D peak of graphene is sharp and about four times more intense than its G peak, whereas the 2D peak of graphite is broader and split into multiple components. The G peak intensity is similar for both materials. This figure is adapted from the work of Ferrari *et al.* [97]

The second-order 2D peak, typically observed around 2700 cm^{-1}, originates from a double phonon resonance process involving two in-plane phonons with opposite momentum. This ensures momentum conservation, enabling a resonance that significantly amplifies the Raman signal. These phonons represent in-plane vibrational modes of carbon atoms, with components both parallel and perpendicular to the carbon-carbon bonds. The 2D peak is highly sensitive to the electronic band structure because the resonance condition depends on the interaction between phonon vibrations and electronic transitions. The term "second-order" refers to the involvement of two phonons in this process, distinguishing it from the first-order G peak, which arises from a single phonon interaction. The characteristics of this peak, including its shape and position, provide insights into the number of graphene layers, reflecting the structural properties of the graphitic material. [96, 98–101]

Figure 3.2 reveals a distinct difference in the shape and intensity of the 2D peak in graphene

compared to graphite. The 2D peak of graphene is remarkably sharp and exhibits an intensity approximately four times that of the G peak. [97] This sharpness is reflected in the full width at half maximum (FWHM) value, ranging from 24-30 cm^{-1}, indicating a high degree of structural order and crystallinity. [102–104] As bulk disorder increases, FWHM values correspondingly rise. In contrast, the 2D peak of graphite is broader and consists of two components, typically around 1/4 and 1/2 the height of the G peak, resulting in an overall FWHM that is almost double that of graphene, often exceeding 40 cm^{-1}. [97, 100, 104] Despite these variations in the 2D peak, the G peak intensity is comparable between monolayer graphene and graphite, underscoring the similarities in their structure. [97, 104] Consequently, the FWHM values are similar, ranging around 13-16 cm^{-1}. [105, 106]

Comparative analysis of commercially produced graphene: hummers' method vs. CVD

As discussed in section 1.3.1, the two predominant methods for synthesising graphene are the hummers' method and chemical vapour deposition (CVD). While this research focuses on shear-mixing as a synthesis process, comparing its outcomes with those from the hummers' method and CVD provides valuable benchmarks for evaluating graphene quality and properties.

The oxidation of graphite to graphene oxide (GO) via the hummers' method, followed by the reduction of GO, is a widely adopted approach to produce reduced graphene oxide (rGO) with properties approaching those of pristine graphene. This method is favored in the graphene production industry for its cost-effectiveness and scalability, although it compromises the structural integrity and performance of the resulting graphene. [55,62,63] As the first synthesis step, graphene oxide (GO), represented by the red spectrum in figure 3.3, is produced by treating graphite with strong oxidizers followed by exfoliation. This process introduces oxygen-containing functional groups, such as epoxy, hydroxyl, and carboxyl, which decrease the crystallinity and increase the defect density within the material. Consequently, a broad D peak, which is not present in graphite or graphene (figure 3.2), is apparent in GO. [107–109]

The D peak, appearing around 1350 cm^{-1}, signals the presence of defects. It arises from a vibrational mode involving distortions in the hexagonal arrangement of carbon atoms. In pristine graphene, this mode remains inactive due to symmetry constraints, which prevent the required interaction between vibrations and light. Defects or edges break this symmetry, enabling the

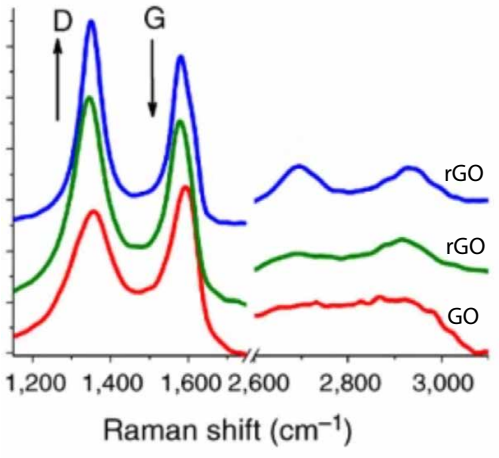

Figure 3.3: Comparison of Raman spectra for GO (red), rGO reduced with hydrazine hydrate ($RGO_{NH2–NH2}$, green), and rGO reduced with hydriodic acid and acetic acid ($RGO_{HI–AcOH}$, blue). The GO spectrum exhibits a broad, intense D peak and an upshifted G peak, with the absence of a 2D peak, indicating high defect density and low crystallinity primarily due to oxidation. The rGO spectra show higher defect density compared to GO, as indicated by increased D peak intensity, a more pronounced 2D peak, and a G peak shift towards the graphite position, suggesting partial recovery of the hexagonal carbon lattice with additional defects from the reduction process. The blue spectrum features a more pronounced 2D peak and a G peak shift closer to the graphite position, indicating a higher degree of structural recovery compared to the green spectrum. This figure is adapted from the work of Moon *et al.* [110]

vibrational mode to become Raman active and detectable as the D peak. [100, 101, 111–113] This peak is broad, with a FWHM between 55 and 125 cm^{-1}. The existence and broad shape of the D peak indicate lattice imperfections, primarily due to the introduction of sp^3 hybridised carbon atoms, which are a result of oxidation. The absence of the 2D band in GO spectrum reflects the breakdown of the sp^2 bonding network, with the structure being primarily dominated by disorder. In GO, the oxidation process introduces oxygen-containing functional groups that disrupt the sp^2 network and the stacking of graphene layers. Additionally, the G peak in the GO spectrum, observed around 1591-1594 cm^{-1}, is higher compared to the G peak of graphite at 1580 cm^{-1}. [97] This peak also has a broader FWHM, ranging from 28 to 66 cm^{-1}, attributed to isolated double bonds resonating at higher frequencies. These characteristics further signal the presence of structural defects in GO. [107–110, 114]

The Raman spectrum of reduced graphene oxide (rGO), represented by the green and blue spectra in figure 3.3, highlights the structural changes following the reduction of GO. Numerous methods, including chemical, thermal, and electrochemical techniques, can be used to reduce GO

to rGO. These spectra demonstrate the variations in rGO quality resulting from different reduction techniques, underscoring the inconsistency in commercially available graphene. The reduction process significantly impacts the quality of the resulting rGO, determining how closely its structure resembles graphene. The green spectrum is obtained using hydrazine hydrate ($RGO_{NH2-NH2}$), whereas the blue spectrum results from the use of hydriodic acid and acetic acid ($RGO_{HI-AcOH}$). Generally, $RGO_{NH2-NH2}$ (green spectrum) introduces nitrogen impurities, resulting in lower quality rGO. Both G peaks in the blue and green spectra shift towards the graphite position at $1580\,cm^{-1}$ [97], with the blue spectrum ($RGO_{HI-AcOH}$) positioned closer at $1581\,cm^{-1}$. The shift highlights the partial recovery of the hexagonal carbon structure, reflecting a structure with remaining defects. Further evidence of structural recovery in rGO is provided by the appearance of a 2D peak, absent in GO, signaling the recovery of the hexagonal carbon lattice. Notably, the 2D peak is more distinct and pronounced in the blue rGO spectrum compared to the green, suggesting a higher degree of structural recovery. However, the intensity of the D peak, located at around $1350\,cm^{-1}$, increased in both rGO spectra, indicating a higher defect density. This increase is attributed to the removal of oxygen-containing functional groups from GO during the reduction process, which results in the creation of additional defects in the carbon lattice. [107–110, 114] Furthermore, a key parameter for assessing the structural quality in carbon-based materials, including graphene, is the I_D/I_G ratio, which compares the intensity of the D band to the G band in Raman spectroscopy. An I_D/I_G ratio below 1 typically indicates low defect density and high crystallinity, classifying various carbon-based materials, such as those in the nanocrystalline graphite phase and pristine monolayer graphene. For GO, the I_D/I_G ratio is 1.04, highlighting a considerable defect density due to the incorporation of oxygen functional groups. Following reduction to rGO, this ratio rises to 1.21, indicating that although some sp^2 carbon networks are restored, new defects are introduced, leading to a higher overall defect density. Both ratios are above 1 showcasing their high defect-density and low crytallinty, and from a scientific standpoint should not be classified as graphene. [110, 111, 113, 114]

In contrast, while CVD is complex and costly, making it less suitable for industrial applications, it yields high-quality graphene through the pyrolysis of a carbon precursor and subsequent atomic arrangement on a substrate. [55, 62] The Raman spectrum of CVD graphene, as illustrated in

figure 3.4, is nearly identical to that of a graphene monolayer (figure 3.2), highlighting the superior structural integrity and minimal defect density achieved through this synthesis method. [115]

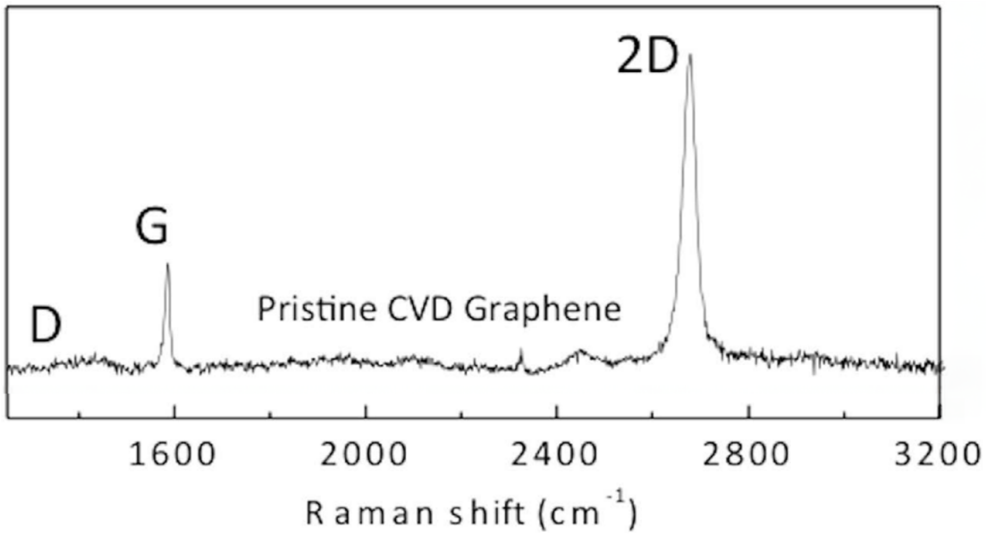

Figure 3.4: Raman spectra of CVD graphene, grown on 25 μm thick copper foils at 1000°C using a quartz tube reactor with CH_4/H_2 as precursors, demonstrate features typical of monolayer graphene. [115] This is evidenced by the sharp 2D peak and the G peak position, which closely align with the spectra shown in figure 3.2. This figure is adapted from the work of Grande *et al.* [115]

Raman spectroscopy analysis of shear-exfoliated graphene

Figure 3.5 shows a representative Raman spectrum for shear-exfoliated graphene from the literature. This synthesis method closely resembles the process utilised in this study, serving as a reference benchmark. The characteristic G peak at 1582 cm^{-1} and 2D peak at 2716 cm^{-1}, typical of graphite/graphene, are observed. The 2D peak intensity is lower than the G peak, indicating that monolayer graphene is not produced. Nevertheless, the 2D peak shape differs from that of graphite, which typically comprises two components (see figure 3.2). The shape of the 2D peak indicates few-layer graphene, with Paton *et al.* estimating a layer count of around 7. [116] A D-band appears around 1350 cm^{-1}, similar to GO and rGO (see figure 3.3), but in this instance, it is narrower and less intense. The corresponding I_D/I_G ratio is 0.17, reflecting a significantly lower defect density compared to rGO/GO. This defect density originates partly from the graphite starting material and may also result from the shear-mixing process. [116]

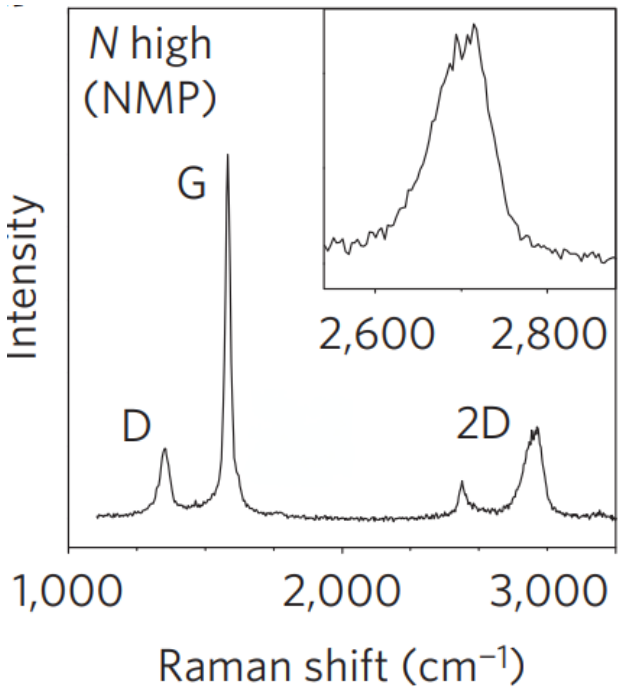

Figure 3.5: Raman spectrum of N-methyl-2-pyrrolidone (NMP)-exfoliated graphene, synthesised with mixing time of 20 min, graphite concentration of 80 g/L, rotor speed of 5700 RPM, and liquid volume of 1500 mL. The spectrum shows a G peak at 1582 cm^{-1} and a 2D peak at 2716 cm^{-1}, typical of few-layer graphene (estimated to have ∼7 layers). A D-band at 1350 cm^{-1}, narrower and less intense than in rGO/GO, reflects a lower defect density ($I_D/I_G = 0.17$), partly due to the graphite precursor and shear-mixing process. This figure is adapted from the work of Paton *et al.* [116].

3.2.2 Experimental evaluation of key Raman spectral characteristics in graphene shear-exfoliated from various PAN concentrations

This analysis aims to evaluate the spectral data from graphene samples produced with varying concentrations of polyacrylonitrile (PAN) in dimethylformamide (DMF) through shear-mixing of graphite. The analysed spectra are shown in figure 3.6. The samples are analysed using a LabRAM Aramis Raman spectrometer, equipped with a 514 nm excitation laser source and a 100x objective lens. The fitting of the Raman spectra is performed using the non-linear least squares method, applying a lorentzian lineshape, as detailed in section 4.1.

Three variations are compared: 0+graphene (without polymer, figure 3.6b), 6+graphene (with 6 wt.% PAN, figure 3.6c), and 9+graphene (with 9 wt.% PAN, figure 3.6d), along with a reference graphite sample (Graphite-R, figure3.6a). The respective peak characteristics are detailed in table 3.1. As depicted in figure 3.6, the deconvoluted and fitted Raman spectra for 0+graphene

and 6+graphene exhibit a slight discrepancy in the peak intensity of the cumulative fit (red) for the G peak compared to the raw spectrum (blue). This difference arises due to the narrow and intense nature of the G peak, coupled with fluctuations in the signal caused by the low sample yield from vacuum filtration, which affects the accuracy of the fit. The limited material results in weaker signals and greater sensitivity to inconsistencies in laser focus or sample orientation, disproportionately influencing the measured data. In contrast, 9+graphene shows this phenomenon less prominently due to a larger sample size available for Raman analysis, leading to more consistent measurements.

The G peak in Raman spectra is a superposition of two components: the G peak and the D' peak. To account for this, the cumulative G peak is deconvoluted into these individual peaks. Typically, the weak D' peak, located around 1620 cm^{-1}, lies in the flatter tail of the cumulative peak, where the slope is low, making it less sensitive to minor fitting errors. Moreover, the D' peak is used only in the intensity ratio with the D peak ($I_D/I_{D'}$). Since the D peak is significantly more intense, its dominance in the ratio ensures that potential minor variations in the D' peak have minimal impact on the results. The D' peak in Raman spectra arises from intravalley phonon scattering, initiated by defect sites such as edges or distortions in the graphene lattice, where lattice vibrations interact with electronic states without significant momentum change, remaining within the same energy region, and providing insights into localised defect types (see section 3.2.3). [100, 101, 111, 113]

To confirm the successful removal of PAN through filtration, the Raman spectra of the samples produced with varying PAN concentrations (0+graphene, 6+graphene, and 9+graphene) are analysed, as depicted in figures 3.6b, 3.6c, and 3.6d. The absence of PAN-related peaks, which are generally broad and appear around 2243 to 2268 cm^{-1}, suggests successful polymer removal. [117, 118] However, the high spectral intensity of graphene due to resonance with the laser limits the detection of residual PAN to cases where it is present in large amounts. To confirm polymer removal with greater certainty, complementary atomic force microscopy analysis (section 3.3.2) demonstrates that the polymer is effectively separated from graphene through vacuum filtration. [119, 120]

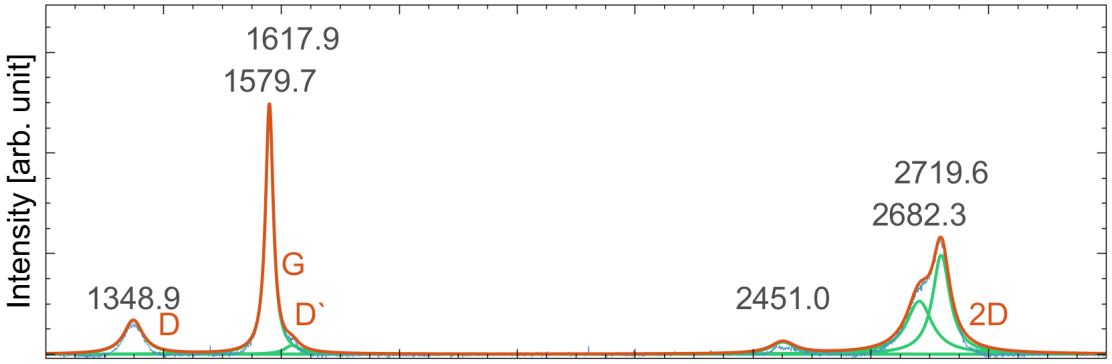

(a) Graphite-R: Raman spectrum of graphite. The distinct shoulder in the 2D peak shape, characteristic of graphite, is clearly visible. D peak indicates vacancy-type defects. Spectrum obtained using a 514 nm laser. Green curve: deconvoluted peaks; blue curve: original spectrum; red curve: fitted spectrum.

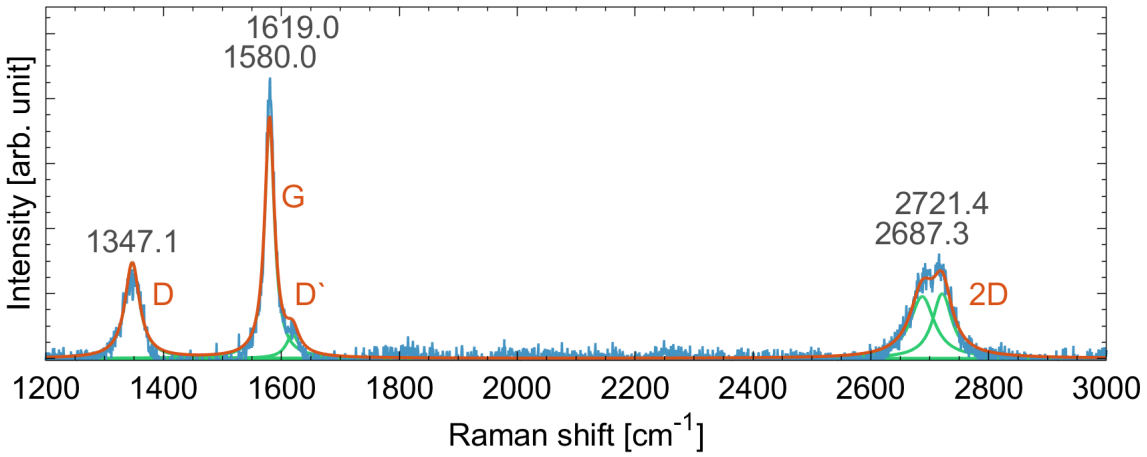

(b) 0+graphene: Raman Spectrum of graphene produced in DMF without polymer via shear-mixing of graphite. Green curve: deconvoluted peaks; blue curve: original spectrum; red curve: fitted spectrum. Obtained with a 514 nm laser; 3 spectra from different sites on the sample are evaluated.

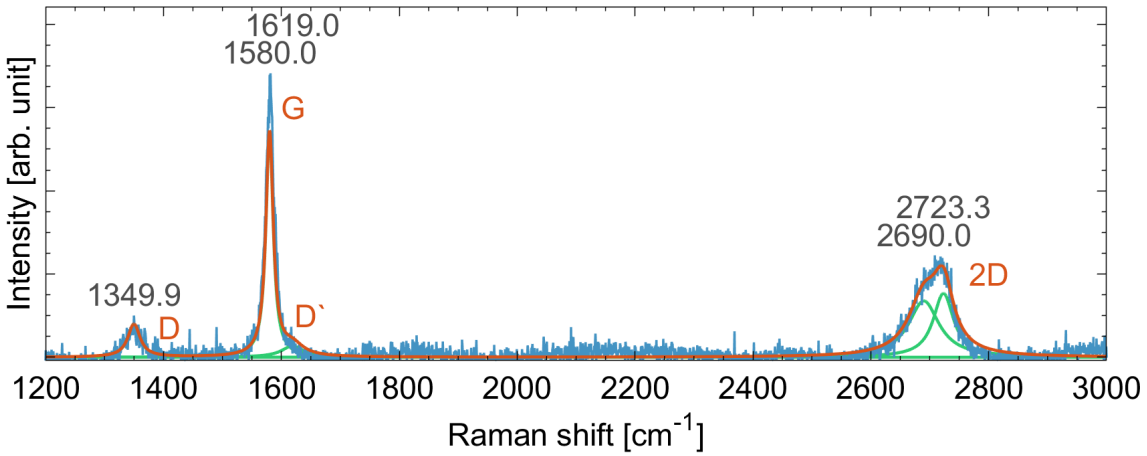

(c) 6+graphene: Raman Spectrum of graphene produced in DMF with 6 wt.%PAN via shear-mixing of graphite. Green curve: deconvoluted peaks; blue curve: original spectrum; red curve: fitted spectrum. Obtained with a 514 nm laser; 3 spectra from different sites on the sample are evaluated.

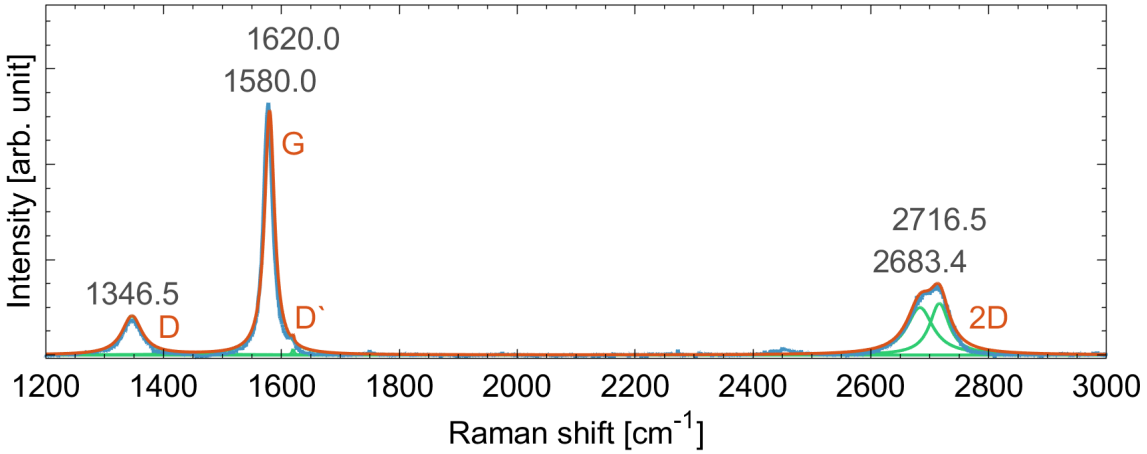

(d) 9+graphene: Raman Spectrum of graphene produced in DMF with 9 wt.%PAN via shear-mixing of graphite. The spectrum is obtained using a 514 nm laser, and 3 spectra from different sites on the sample are evaluated. Green curve: deconvoluted peaks; blue curve: original spectrum; red curve: fitted spectrum.

Figure 3.6: Raman spectra for 0+graphene (shear-exfoliated without polymer), 6+graphene (shear-exfoliated in DMF with 6 wt.% PAN), 9+graphene (shear-exfoliated in DMF with 9 wt.% PAN), and Graphite-R (graphite reference sample with 150 μm flake size and low defect density). The 2D peak shape in the graphite spectrum features a distinct shoulder, characteristic of graphite, along with a D peak indicating vacancy-type defects. The graphene samples do not exhibit the sharp 2D peak typical of monolayer graphene, which is usually four times more intense than the G peak, as seen in the reference monolayer graphene spectrum (figure 3.2). Instead, the filtered material shows features of few-layer graphene, including a pronounced G peak at 1580 cm^{-1} and a broad 2D peak at 2700 cm^{-1}, without the distinct shoulder typical of Graphite.

The Raman spectra of 0+graphene, 6+graphene, and 9+graphene do not show the distinct sharp 2D peak of monolayer graphene, which is typically four times more intense than the G peak, as seen in the reference monolayer graphene spectrum (figure 3.2). This indicates that the synthesis method does not exclusively produce monolayer graphene. Consequently, the Raman spectrum of the filtered material reveals features of few-layer graphene, including a pronounced G peak at 1580 cm^{-1} and a broad 2D peak at 2700 cm^{-1}, without the pronounced, distinct shoulder typical of graphite. [96, 98, 100, 101]

As summarised in table 3.1, the G peak position is consistent across all samples, appearing at approximately 1579.7 cm^{-1} for graphite and 1579.8 cm^{-1} for the 0+graphene and 6+graphene samples, reflecting the in-plane bond stretching of sp^2-bonded carbon atoms.

The 9+graphene sample shows a slight upshift to 1580 cm^{-1}. The 9+graphene sample also has a greater FWHM of 19.5 cm^{-1} compared to Graphite-R (15.9 cm^{-1}) and 6+graphene (15.0 cm^{-1}), indicating a higher degree of structural defects in 9+graphene. Similarly, 0+graphene

Table 3.1: Raman peak characteristics for 0+graphene (shear-exfoliated without polymer), 6+graphene (shear-exfoliated in DMF with 6 wt.% PAN), 9+graphene (shear-exfoliated in DMF with 9 wt.% PAN), and Graphite-R (graphite reference sample with 150 μm flake size and low defect density). All values are derived from deconvoluted and fitted Raman spectra. The 2D peak is deconvoluted into two peaks (1st and 2nd peaks, as shown in the third column). For graphene samples, values are averaged from three spectra, with standard deviations reflecting local variations rather than measurement errors. Graphite-R values are based on a single deconvoluted spectrum. Raman intensity can fluctuate due to experimental conditions such as laser focus, surface roughness, and sample orientation. Therefore, the analysis focuses on peak position, FWHM, and intensity ratio.

Sample	D Position	G Position	D' Position	2D Position (1./2. peaks)
Graphite-R	1348.9	1579.7	1617.9	2682.3 / 2719.6
0+graphene	1349.1 ± 1.4	1579.8 ± 0	1619.2 ± 0	2687.9 ± 0.8 / 2722 ± 1.0
6+graphene	1351.4 ± 1.3	1579.8 ± 0	1619.2 ± 0	2688.3 ± 2.9 / 2722.6 ± 0.4
9+graphene	1347.1 ± 1.3	1580 ± 0.4	1617.9 ± 2.8	2685 ± 1.3 / 2716.1 ± 1.1

Sample	D FWHM	G FWHM	D' FWHM	2D FWHM (1./2. peaks)
Graphite-R	39.2	15.9	30.0	52.5 / 35.2
0+graphene	34.7 ± 8.1	17.7 ± 4.0	24.4 ± 6.7	51.8 ± 3.1 / 40.1 ± 0.2
6+graphene	23.3 ± 2.8	15.0 ± 0	42.7 ± 4.1	65.5 ± 2.3 / 41.4 ± 1.9
9+graphene	34.1 ± 8.2	19.5 ± 2.7	10.8 ± 6.3	57.3 ± 3.0 / 35.34 ± 4.1

Sample	I_D/I_G	$I_D/I_{D'}$
Graphite-R	0.136	3.85
0+graphene	0.317 ± 0.13	3.297 ± 0.70
6+graphene	0.167 ± 0.04	2.69 ± 0.27
9+graphene	0.170 ± 0.02	5.1 ± 2.00

displays a higher FWHM of 17.7 cm^{-1}. [2, 13, 97, 100] Graphite and 6+graphene exhibit FWHM values within the reported range for graphite and graphene (13-16 cm^{-1}), whereas 0+graphene and 9+graphene show slightly higher values. [105, 106] Importantly, while FWHM values increase with structural disorder, the introduction of edges, when several graphene flakes are captured by Raman spectroscopy due to their size, does not significantly affect these measurements. [2, 13, 97, 100] Hence, the observed increase for 0+graphene and 9+graphene suggests an increase in structural disorder.

For Graphite-R, the D peak is at 1348.9 cm^{-1} with a FWHM of 39.2 cm^{-1}. The studied samples show slight variations: 0+graphene at 1349.1 cm^{-1}, 6+graphene at 1351.4 cm^{-1}, and 9+graphene at 1347.1 cm^{-1}. The considerably higher standard deviation for the D peak (1.4 for 0+graphene, 1.3 for 6+graphene and 9+graphene) compared to the G peak (std $\leq$ 0.4) suggests that the

D peak location around 1350 cm^{-1} is consistent across samples, implying that the positional shifts are not analytically significant. The FWHM varies among the samples, with 6+graphene exhibiting the narrowest FWHM (23.3 cm^{-1}) and 0+graphene the broadest (34.7 cm^{-1}), closely followed by 9+graphene (34.1 cm^{-1}). This correlates with the I_D/I_G ratio, assessing structural quality, where 6+graphene has the lowest ratio (0.167). These values align with the findings discussed in the literature review in section 3.2.1. However, despite having a similar FWHM, 0+graphene shows a higher I_D/I_G ratio (0.317) compared to 9+graphene (0.170), indicating other influencing factors are present. One possible explanation is that shear-mixing reduces the original graphite flake size, creating smaller graphene flakes. As a result, multiple graphene flakes are captured in one Raman spectrum, with their edges manifesting as defects (edge defects), thereby affecting the D peak and I_D/I_G ratio. [116] Therefore, understanding the relationship between defect types and flake sizes is essential. Section 3.2.3 presents further analysis of I_D/I_G and the D' peak, utilised for the $I_D/I_{D'}$ ratio, and their correlation with flake size and crystalline domain size. High-quality graphite (Sigma-Aldrich, CAS: 7782-42-5) with a lateral size of 150 μm and low defect density is chosen as the base material for graphene production in this experiment. [82] Its Raman spectrum is referenced as Graphite-R. The D peak intensity is relatively low compared to the G peak, reflected by an I_D/I_G ratio of 0.136, providing a strong baseline for evaluating the effects of PAN concentration in the resulting samples. With a large flake size, Graphite-R shows the lowest I_D/I_G ratio (0.136) and no edge defects, while the highest FWHM (39.2 cm^{-1}) reflects bulk disorder. The produced graphene retains this defect density, along with additional defects potentially introduced during synthesis or due to the reduced flake size.

The 2D peak is used to determine graphene layer thickness, as detailed in section 3.2.4.

It is important to note that intensity values are primarily used to derive parameters such as I_D/I_G and $I_D/I_{D'}$, rather than being discussed independently.

3.2.3 Graphene defect and flake size analysis

In Raman spectroscopy, graphene edges manifest as defects, necessitating the differentiation of edge defects from other defect types. [116] To evaluate the types of defects present in the studied graphene samples, the empirical $I_D/I_{D'}$ ratio method, as described by Eckmann

et al., is utilised. This ratio enables the identification of the predominance of edge versus vacancy defects, thereby providing a comprehensive analysis of the defect characteristics in the studied graphene samples. [98] The study underscores that the ratio of the D and D' peak intensities in the Raman spectrum is more indicative of the nature and type of defects within the material than of the overall defect density. [98]

Accordingly, the $I_D/I_{D'}$ ratio is identified as a key indicator for classifying defects, with values of 13 pointing to sp^3 hybridisation defects, 7 to basal-plane/ vacany defects, and 3.5 to edge defects, determined empirically through systematic Raman analysis of graphene samples subjected to controlled defect introduction, such as ion bombardment and chemical modifications. [98]

Paton *et al.* demonstrated the applicability of the $I_D/I_{D'}$ ratio on graphite, reporting values of 7.2 to 8.9 associated with vacancy-type defects, primarily arising from the sp^2 hybridised structure of graphite that inherently excludes sp^3 defects, while the lack of edge defects is due to its large flake size.

For Graphite-R (figure 3.6a), the Raman spectrum shows a small D peak, signaling low defect density. This, combined with the large average flake size of 150 μm [82], points to the defects being predominantly vacancy-type. However, its $I_D/I_{D'}$ ratio of 3.85 is 45% lower than the standard indicator value for vacancy-type defects established by Eckmann *et al.*. [98] Paton *et al.* point out the absence of standard deviation data in the study from Eckmann *et al.*, raising concerns about the precision of the $I_D/I_{D'}$ ratio as a marker for defect types due to the lack of statistical significance. [116] As such, large flake size and low defect density of graphite in this study, as confirmed in [82], are likely to influence the conditions under which the D' peak becomes active. While this may cause $I_D/I_{D'}$ ratio values to deviate from those established by Eckmann, the relationship remains applicable: values above the threshold indicate an increase in sp^3 hybridised structures, while those below suggest a rise in edge defects. Thus, the vacancy-type value of 3.85 reported in this study, being 45 % lower than the 7 established by Eckmann, adjusts the edge defect indicator to approximately 1.9 in this context.

The I_D/I_G and $I_D/I_{D'}$ ratios of the studied samples, detailed in table 3.2, indicate the presence of both edge and vacancy-type defects across all samples due, except for the 9+graphene one. In the case of the 9+graphene sample, the $I_D/I_{D'}$ ratio of 5.1 indicates a predominance of vacancy-type

defects. Due to the high polymer concentration, the increased viscosity results in heat production and subsequent polymer solidification during shear-mixing. This process introduces mechanical stresses during the shear-exfoliation of graphene, which could potentially damage the hexagonal carbon structure and contribute to the formation of vacancy-type defects.

Table 3.2: Overview of I_D/I_G and $I_D/I_{D'}$ ratios for 0+graphene, 6+graphene, 9+graphene, and graphite. The I_D/I_G ratios for the graphene samples are higher than those of Graphite-R, indicating additional defects/edges introduced during shear-exfoliation. The $I_D/I_{D'}$ values for 0+graphene and 6+graphene reflect a substantial presence of edge defects, while the 9+graphene sample shows a predominance of vacancy-type defects.

	0+graphene	**6+graphene**	**9+graphene**	**Graphite-R**
$\mathbf{I_D/I_G}$	0.317	0.167	0.17	0.136
$\mathbf{I_D/I_{D'}}$	3.297	2.69	5.1	3.85

As previously identified, the vacancy-type defects present in the graphene samples partly originate from the graphite (Graphite-R) used as the starting material for graphene synthesis. However, the I_D/I_G ratios of the studied graphene samples (0+graphene = 0.317, 6+graphene = 0.167, and 9+graphene = 0.17) exceed that of Graphite-R (0.136) due to the creation of additional defects during the shear-exfoliation process from graphite to graphene. Specifically, the $I_D/I_{D'}$ values for 0+graphene (3.297) and 6+graphene (2.69), being lower than that of Graphite-R (3.85), suggest that part of this increase can be attributed to edge defects. [52, 100, 116]

To gain a deeper insight into the types and densities of defects present, the findings are correlated with the crystalline domain size and flake size.

The crystalline domain size L_a is calculated, based on the equation 3.1, with a laser excitation wavelength λ of 514 nm. The constant $(2.4 \cdot 10^{-10})$ in the (L_a) formula is derived from empirical studies and accounts for the wavelength dependency when relating I_D/I_G to the crystallite size in graphitic materials. [121, 122]

$$L_a[nm] = (2.4 \cdot 10^{-10}) \cdot (\lambda[nm])^4 \cdot \left(\frac{I_G}{I_D}\right) \tag{3.1}$$

A second method uses the formula proposed by Paton *et al.* to calculate the flake size, L_f, in shear-exfoliated graphene, as described in equation 3.2. This approach is based on the assumption

that when edge defects are the primary type of defect present, the D:G band intensity ratio correlates with the average lateral size of the graphene flakes.

$$L_f = \frac{k}{(ID/IG)_{graphene} - (ID/IG)_{graphite}} = \frac{0.17}{ID/IG - 0.14} \tag{3.2}$$

The formula takes into consideration the defects present in the initial graphite material, evidenced by an I_D/I_G ratio of 0.14 for the graphite (table 3.1). Given the large grain size of the graphite, these defects are unlikely to be edge-related, suggesting the presence of vacancy defects in the initial graphite material. The coefficient k, determined to be approximately 0.17 by Paton *et al.*, is derived from the slope of the graph plotting I_D/I_G against $(1/L_f)$, as detailed in their supplementary information. The k value depends on the graphite source, being influenced by defect density and flake size. In this study, the comparable I_D/I_G ratio supports the use of the same k value for further calculations. [80, 116] The calculated values for the crystalline domain size L_a and graphene flake size L_f are presented in table 3.3.

Table 3.3: Calculation of crystalline domain size (L_a) and graphene flake size (L_f) for 0+graphene, 6+graphene, 9+graphene, and Graphite-R. The graphene flakes are approximately 30 times smaller than graphite flakes. Notably, the L_a for 6+graphene and 9+graphene remains close to that of graphite, suggesting the synthesis process primarily increases edge defects without substantially creating vacancy defects. The 0+graphene sample, with flakes five times smaller than 6+graphene, exhibits a significantly reduced L_a, highlighting more pronounced vacancy-type characteristics. The graphite flake size is not derived from the formula (L_f), it is a known quantity from the supplier Sigma-Aldrich (CAS: 7782-42-5). [82]

	0+graphene	**6+graphene**	**9+graphene**	**Graphite-R**
L_a [nm]	52.8	100.3	98.5	123.2
L_f [nm]	939.2	5483.9	5000	150000

The significant reduction in L_f across all shear-exfoliated samples, with graphene flakes being over 30 times smaller than those of graphite, strongly suggests that the increase in the I_D/I_G ratio is primarily due to an increase in edge defects, resulting from the reduced flake sizes.
Given that the flake size L_f is significantly smaller for the graphene samples, the small variation in crystalline domain size L_a between 6+graphene and 9+graphene, relative to Graphite-R, supports the conclusion that the synthesis process with high polymer concentration does not substantially create vacancy defects within the crystalline domains of graphene. [52, 100] The

$I_D/I_{D'}$ ratio of 5.1 for 9+graphene indicates a significant change in defect type, being higher than that of graphite (3.85). Considering that graphite has a low defect density, which may explain its smaller $I_D/I_{D'}$ ratio relative to other graphite materials [82, 116], it appears that the 9+graphene is dominated by vacancy defects. This would imply that the crystalline domain size L_a should be significantly smaller than that of 6+graphene. The absence of differentiation between various defect types, such as edge defects and vacancy defects, within the L_a formula may account for this observation. On the contrary, the increase in the I_D/I_G ratio for 0+graphene can largely be attributed to its flake size being five times smaller than that of 6+graphene, the 0+graphene exhibits more pronounced vacancy-type characteristics, as indicated by its higher $I_D/I_{D'}$ ratio and significantly reduced L_a compared to 6+graphene.

This finding suggests that the introduction of polymer may distribute the shear forces more uniformly, resulting in fewer vacancy defects and and the formation of larger flakes compared to solutions without polymer. Among the studied samples, 6+graphene demonstrates the best performance, with the lowest I_D/I_G ratio (0.167) and $I_D/I_{D'}$ ratio (2.69), and a slightly smaller L_a of 100.3 nm compared to graphite (123.2 nm), despite having an average flake size approximately 30 times smaller—and possibly even further reduced, as elaborated in the AFM analysis in section 3.3.2.

3.2.4 Graphene layer thickness determination

To verify that the produced graphene samples contain 10 layers or fewer [61], this section analyses the graphene layer number through 2D peak shape analysis, peak position analysis of deconvoluted 2D peaks, and a quantitative empirical method.

2D peak shape analysis

Research has shown a correlation between the thickness of graphene and the distinct profiles of its 2D Raman bands. Ferrari *et al.* have empirically demonstrated this correlation, as depicted in figure 3.7 of their study.

The evolution from a sharp to a broader, less defined 2D peak reflects the increase in graphene layers, with a forming shoulder ($\sim$2690 cm^{-1}) adjacent to the main 2D peak indicating multilayer graphene ($\geq$ 5 layers). This shoulder replaces the smaller feature observed in bilayer

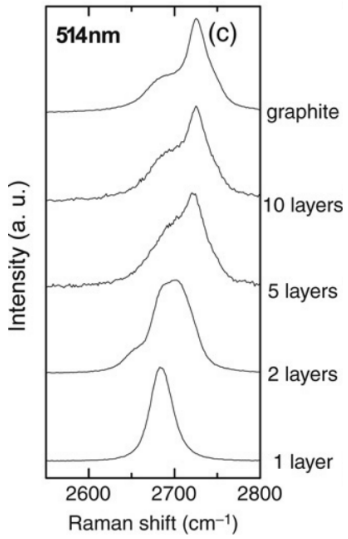

Figure 3.7: The Raman spectrum of the 2D peak evolution, presented by [97], illustrates the transformation of the 2D peak shape from monolayer graphene to graphite. Ferrari *et al.* confirm the number of layers using high-resolution TEM to count dark lines at folded edges, corresponding to the layer count, and electron diffraction to validate the crystalline structure and stacking configuration. Raman spectroscopy further verifies the layer number by analysing the evolution of the 2D peak shape and intensity. The spectra are obtained using a 514 nm laser. [97, 123]

graphene near $\sim$2690 cm^{-1}, which becomes indistinguishable due to the dominance of multilayer interactions. [51, 97]

The analysis of the Raman 2D peak shapes from all studied samples reveals the absence of a distinct shoulder adjacent to the main peak, indicating that the material does not contain graphite. Additionally, the lack of a sharp, singular peak further suggests that the graphene contains more than one layer. A comparison with the 2D peak profiles shown in figure 3.7 indicates that the broad shape of the 2D peak in our studied samples corresponds to a graphene layer number ranging from 5 to 10.

Peak position analysis of deconvoluted 2D peak

The interpretation of peak positions after 2D peak deconvolution provides additional insights into the number of graphene layers, allowing identification of monolayer, bilayer, few-layer, and multilayer graphene components. Peaks at 2647 cm^{-1}, 2690 cm^{-1}, and 2727 cm^{-1} are indicative of monolayer or bilayer, few-layer (3–5 layers), and multilayer graphene (5-10 layers), respectively. [113] This approach relies on deconvoluting the 2D peak to determine contributions

from different graphene layer numbers. A peak below 2650 cm^{-1} reflects the presence of monolayer or bilayer graphene, but its absence suggests minimal or no contribution from these layers. However, the similarity of graphite and multilayer graphene peaks in the $\sim$2727 cm^{-1} range requires additional context, such as 2D peak shape analysis, to ensure accurate attribution. In this study, the 2D peak of the 6+graphene sample is deconvoluted into two distinct components, located at approximately 2687.1 $\pm$ 1.8 cm^{-1} and 2720.2 $\pm$ 3.6 cm^{-1} (refer to table 3.1). Similar 2D peak deconvolution results are observed for the 9+graphene and 0+graphene samples. For 9+graphene, the components are found at 2687.9 $\pm$ 0.8 cm^{-1} and 2722$\pm$ 0 cm^{-1}, while for 0+graphene, the components are at 2685 $\pm$ 1.3 cm^{-1} and 2716 $\pm$ 1.1 cm^{-1}. These results indicate the presence of few-layer to multilayer graphene in the samples.

The peak position analysis of the deconvoluted 2D peak aligns with the 2D peak shape analysis (discussed in the last paragraph), determining the presence of few-layer to multilayer graphene.

Quantitative method based on empirical study

In their work, Paton *et al.* [116] propose a quantitative method to assess the thickness of liquid-exfoliated graphene, utilising a thickness metric M, as outlined in equation 3.3. The metric M is defined as the normalised intensity ratio of the 2D peak (2DPM) to its adjacent shoulder. Given the ambiguity in defining the position of the shoulder, it is set at $2DPM - 30cm^{-1}$ from the main 2D peak. The intensities of graphite, along with the position of the 2D peak maximum (2DPM), are extracted from the graphite Raman spectrum presented in figure 3.6a. The function of the metric M is to correlate the 2D peak intensity ratio with graphene thickness.

$$\begin{aligned} M &= \frac{I_{\text{graphene}}(2DPM)/I_{\text{graphene}}(2DPM-30)}{I_{\text{graphite}}(2DPM)/I_{\text{graphite}}(2DPM-30)} \\ &= \frac{I_{\text{graphene}}(2719.6)/I_{\text{graphene}}(2689.2)}{197.82/140.53} \end{aligned} \tag{3.3}$$

Using the metric M, the mean graphene layer number, N_G, is estimated through an empirical equation formulated by Paton *et al.*, as detailed in equation 3.4. This equation is derived by plotting well-defined N_G values from literature against the metric M obtained from their respective Raman spectra, establishing a relationship based on graphene samples with thicknesses up to

20 layers, which defines the limitation of this method. For this method, Paton *et al.* estimate an error margin of approximately ± 1.5 layers and emphasise the need to collect spectra under consistent conditions for reliable application. [116]

$$N_G = 10^{0.84M+0.45M^2} \tag{3.4}$$

The findings, detailed in table 3.4 present the calculated thickness metric M and the corresponding average number of graphene layers N_G. The results indicate that the mean number of graphene layers for 0+graphene is 11 ± 1.5. To reflect the discrete nature of graphene layers, the thickness is rounded to a range of 9 to 13 layers. For 6+graphene, the mean number of layers is 9 ± 1.5, corresponding to a physical range of 7 to 11 layers. In the case of 9+graphene, the mean number of layers is 7 ± 1.5, translating to a range of 6 to 9 discrete layers.

Table 3.4: Calculation of the thickness metric (M) and the corresponding mean number of graphene layers per flake (N_G) for 0+graphene, 6+graphene, and 9+graphene.

	0+graphene	**6+graphene**	**9+graphene**
M	0.844	0.799	0.724
N_G	11 ± 1.5	9 ± 1.5	7 ± 1.5

Results of graphene layer thickness analysis

This study aims to create a synthesis process for graphene with 10 layers or fewer, as exceeding this threshold results in low-quality material commonly seen in commercially available graphene. [61] The findings in table 3.5 provide a comprehensive evaluation of graphene layer numbers using three different analytical methods for 0+graphene, 6+graphene, and 9+graphene samples. These methods include 2D peak shape analysis, peak position analysis of deconvoluted 2D peaks, and a quantitative method based on an empirical study.

For all three studied variants (0+graphene, 6+graphene, and 9+graphene), the 2D peak shape analysis indicates a range of 5-10 layers. This broad estimation suggests that the samples generally contain fewer than 10 layers, meeting the main objective.

Table 3.5: Evaluation of graphene layer number using various analytical methods for 0+graphene, 6+graphene, and 9+graphene, demonstrating successful graphene production with layer counts below 10 except for 0+graphene, which shows the highest count, followed by 6+graphene and 9+graphene; N_G: average number of graphene layers & GL: graphene layer number range.

Method	0+graphene	6+graphene	9+graphene
2D peak shape analysis	GL: 5-10	GL: 5-10	GL: 5-10
Graphene layer range identification via deconvoluted 2D peak analysis	GL: 3-5 and 5-10	GL: 3-5 and 5-10	GL: 3-5 and 5-10
Quantitative method based on empirical study	N_G: 11 ± 1.5 (range: 9-13)	N_G: 9 ± 1.5 (range: 7-11)	N_G: 7 ± 1.5 (range: 5-9)

The peak position analysis of deconvoluted 2D peaks from shear-exfoliated graphene reveals compositions of 3–5 layers and 5–10 layers for all three variants, supporting the 2D peak shape analysis findings.

The quantitative method provides an estimation of the mean graphene layer number. The 0+graphene sample has a mean layer count of 11 ± 1.5, which slightly exceeds the 10 layer threshold. In contrast, the 6+graphene and 9+graphene samples have mean layer numbers of 9 ± 1.5 and 7 ± 1.5, respectively, both within the target range.

The combined findings from all three methods demonstrate that the 6+graphene and 9+graphene samples successfully meet the criteria of having fewer than 10 layers (table 3.5), thus qualifying as graphene. Using fewer than 10 graphene layers ensures the material retains its 2D properties, as thicker stacks behave like bulk graphite with reduced mechanical and electrical performance, making them unsuitable for advanced fibre applications. [61]

The 9+graphene sample exhibits the lowest average number of graphene layers, at 7 layers, indicating a significant reduction in layer count with increased polymer concentration. This trend indicates that increased polymer concentration effectively reduces the number of graphene layers. However, at polymer concentrations as high as 9 wt.%, Raman analysis indicates an increase in structural imperfections within the graphene. This may result from heat generation and polymer solidification during the high-viscosity shear-mixing process, negatively affecting the

graphene synthesis process. Balancing polymer concentration is crucial to optimising layer count while minimising defects.

Consequently, the 6+graphene synthesis condition, despite resulting in a slightly higher average number of layers (9 instead of 7), is identified as the most suitable for this study. 6+graphene balances a low number of layers with minimal introduction of defects, making it the optimal choice for producing high-quality graphene.

3.3 Quantifying topography of graphene via atomic force microscopy analysis

Atomic force microscopy (AFM) is a technique used to generate high-resolution images at the nanoscale, revealing detailed surface topographies. This method utilises a cantilever with an atomically sharp probe at its end, which oscillates dynamically near its resonance frequency. As the probe scans the surface, variations in the cantilever oscillation frequency are detected and recorded to produce an AFM image. Specifically, as the tip and sample come closer, repulsive forces dampen the oscillation, enabling imaging without direct physical contact between the tip and the surface. The image is generated by recording variations in the oscillation damping as the tip scans across the surface. [124, 125]

3.3.1 Comparative analysis of AFM images from literature: graphene production via CVD, hummers' method, and shear-mixing

This analysis compares AFM images from literature, focusing on graphene produced by the most common methods— CVD and hummers' method—alongside shear-mixing, which is closest to the method employed in this study. The AFM images display topological differences in graphene produced by CVD (figure 3.8), hummers' method (figure 3.9), and shear mixing (figure 3.11).

CVD is a widely used technique for producing low-defect graphene films, as detailed in section 3.2. The AFM image of copper-catalysed chemical vapor deposition-produced graphene in figure 3.8 A displays a large, continuous single graphene layer extending across the entire image (approximately 5 μm). The graphene exhibits distinct micron-sized wrinkles and particles, each measuring several nanometres in height (up to 6 nm). The formation of wrinkles occurs during the growth and subsequent transfer of graphene. The particles identified are residues of the PMMA polymer used to transfer the graphene from the copper metal substrate onto silicon. The height measurement, shown in figure 3.8B, is approximately 0.9 nm. This elevated thickness of graphene on a substrate compared to the interlayer spacing of graphene-graphene ($\sim$0.35 nm) can result from substrate-induced interactions and environmental effects such as adsorbates, contamination, or atomic-scale imperfections in the substrate surface. [69, 71, 126] Defects and impurities, such as those observed,

significantly decrease the electrochemical stability and electrical conductivity of graphene. [69, 127] Addressing these issues remains a critical topic in the CVD research field. [69, 126, 127]

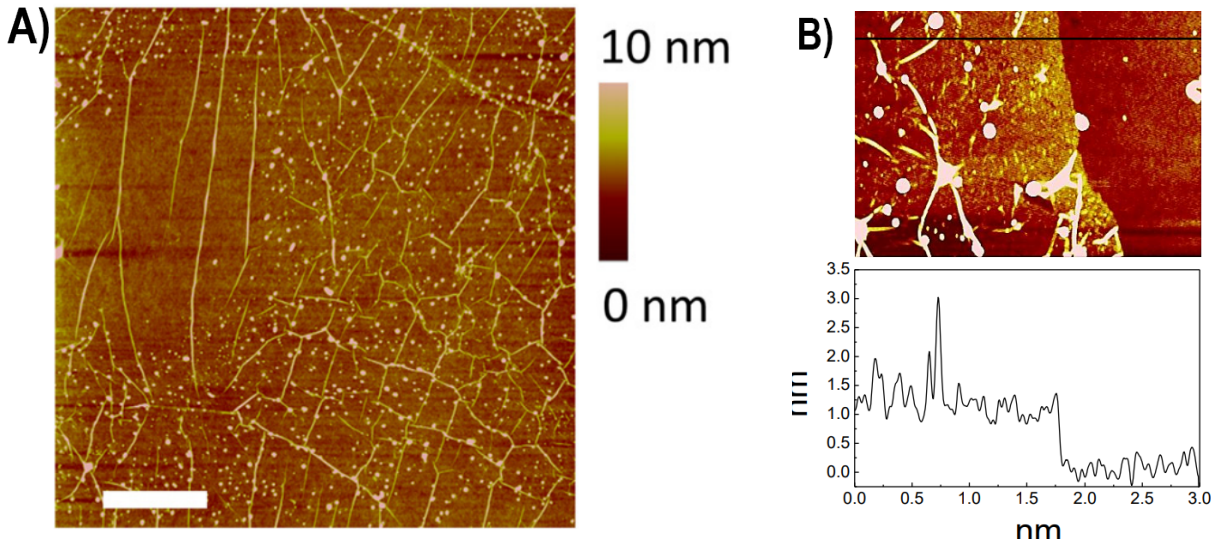

Figure 3.8: The monolayer graphene is prepared by copper-catalysed chemical vapor deposition (CVD) on a silicon wafer, using methane as the carbon source. A) AFM image shows CVD graphene on a silicon wafer, with micron-sized wrinkles from the growth and transfer process, and particles from PMMA used in the transfer process, with a scale bar representing 1 μm. B) The AFM image and cross-sectional analysis of the CVD graphene edge indicate a graphene height of ~0.9 nm, consistent with monolayer graphene. Figure derived from Zhao *et al.* [69].

In contrast to CVD-grown graphene, reduced graphene oxide (rGO) synthesised by the hummers' method exhibits a high defect density, as discussed in section 3.2. Further, the AFM analysis reveals significant variation in the topological characteristics of rGO, exhibiting both dot-like and leaf-like structures (figure 3.9 a).

Through centrifugation, these two topological types are successfully separated. The resulting AFM images reveal dot-like rGO sheets with lateral dimensions less than 100x100 nm (figure 3.9 b), left) and leaf-like rGO sheets with lateral dimensions exceeding 500x500 nm figure 3.9 b), right). [128] The height profiles indicate that the rGO sheets have an approximate thickness of 1.2-1.6 nm, which is higher than that of CVD-grown monolayer graphene (~0.9 nm). [69]

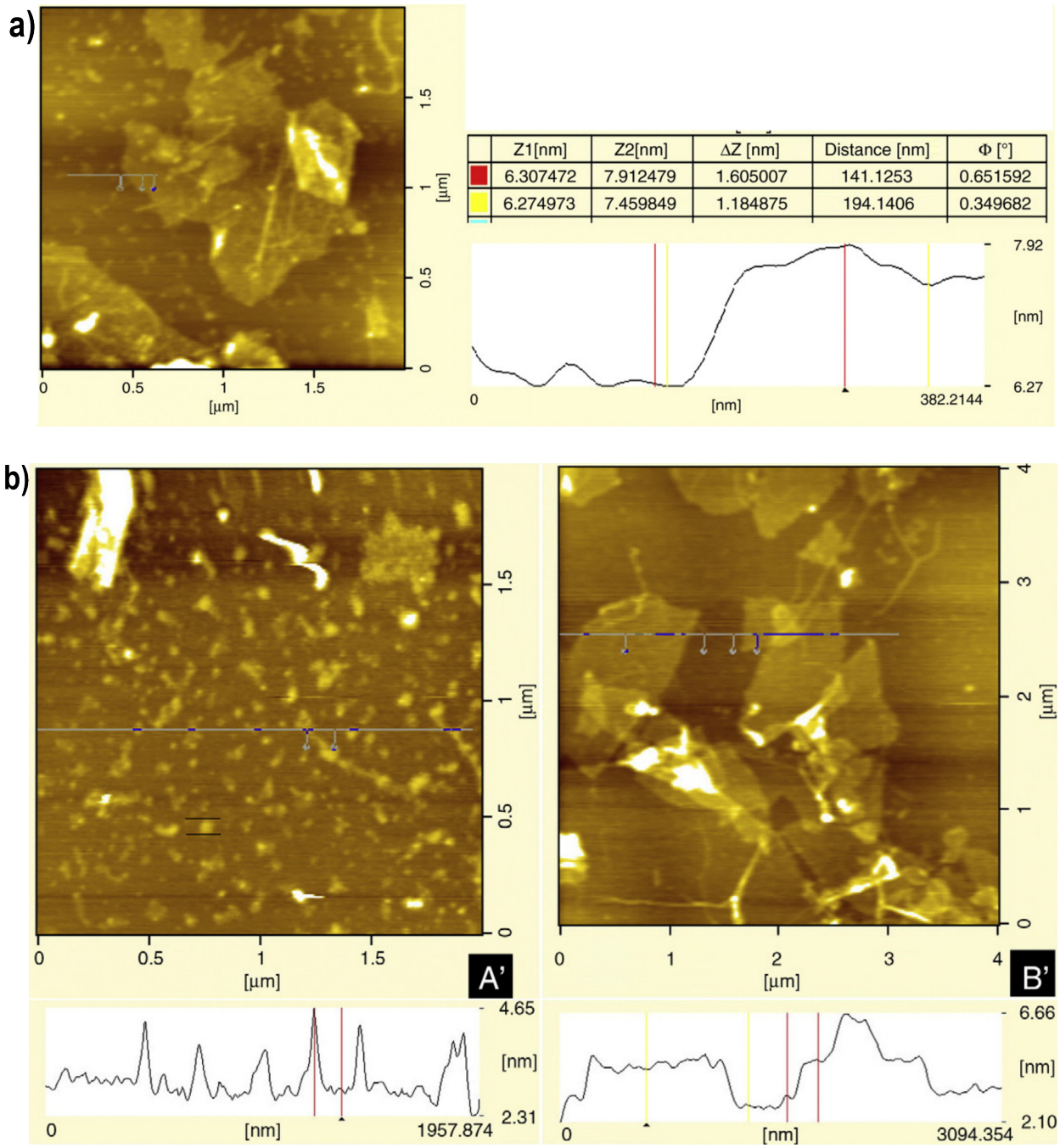

Figure 3.9: AFM images of reduced graphene oxide (rGO) produced by the hummers' method, which involves the oxidation of graphite using $KMnO_4$, $NaNO_3$, and H_2SO_4. The chemical reduction is conducted using hydrazine solution. Prepared on cleaved mica for AFM imaging. a) AFM image of rGO sheets presents a wide range of flake morphologies, including both dot-like and leaf-like shapes. b) AFM image of rGO sheets after centrifugation at 4000 RPM for 20 minutes. Sample-A' represents the supernatant, showing dot-like rGO sheets with lateral dimensions less than 100x100 nm (left). Sample-B' is the sediment, exhibiting leaf-like rGO sheets with lateral dimensions exceeding 500x500 nm (right). The AFM image includes a grey line, representing the area from which the histogram data is derived, with a small arrow indicating the region of height measurements. Each height difference between the marked lines is approximately 1.2-1.6 nm. The figure is derived from Zhang *et al.* [128]

Shear-exfoliated graphene displays a range of morphologies similar to those observed in rGO produced via the hummers' method, as depicted in figure 3.10. An aqueous surfactant solution is utilised in the production process to mitigate reaggregation. The surfactant molecules adhere to the graphene sheets, creating repulsive forces that maintain their dispersion. This results in isolated flakes being visible in the AFM image. [116, 129] It should be noted that the AFM images and histograms show flakes with surfactant, which impacts the height measurements used to determine the number of layers.

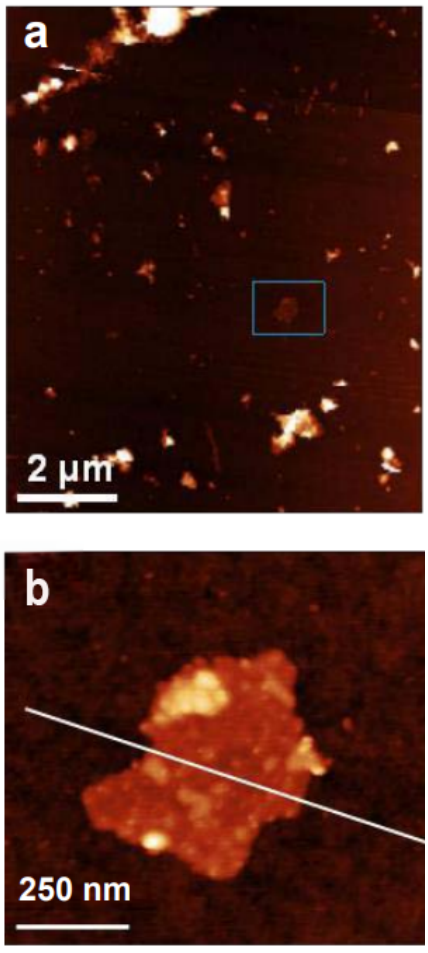

Figure 3.10: a) AFM image of shear-exfoliated graphene. b) AFM image of a single graphene sheet. Synthesis: Aqueous surfactant solution (sodium cholate, NaC) with a rotor speed of 4500 RPM, rotor diameter of 32 nm, initial graphite concentration of 50 mg/ml, and a mixing time of 20 min on Si/SiO_2. Figure derived from Paton *et al.* [116]

Paton *et al.* claim that approximately 7% of the graphene sheets exhibit a height close to

2 nm, interpreted as monolayer graphene (∼0.95 nm) with an additional ∼1 nm attributed to the surfactant layer, as this is the lowest thickness observed. [116] While Raman spectroscopy identifies these flakes as monolayer graphene, the presence of a prominent D peak and a 2D peak intensity less than four times that of the G peak raises questions about the robustness of this conclusion. [97] This correlation between the measured height of graphene flakes and the estimated number of layers, N_G, is visualised in figure 3.11, which includes AFM images of the flakes alongside their height distribution and layer number estimation. In this figure, monolayer graphene shows a height of approximately 2 nm, bilayer graphene around 3 nm, trilayer graphene about 3.8 nm, and few-layer graphene between 6 and 8 nm. Paton *et al.* conduct a statistical analysis of the samples in the study, counting 100–110 flakes per sample, with the result that all samples contain fewer than 10 monolayers, with a mean layer number between 7 and 8. [116]

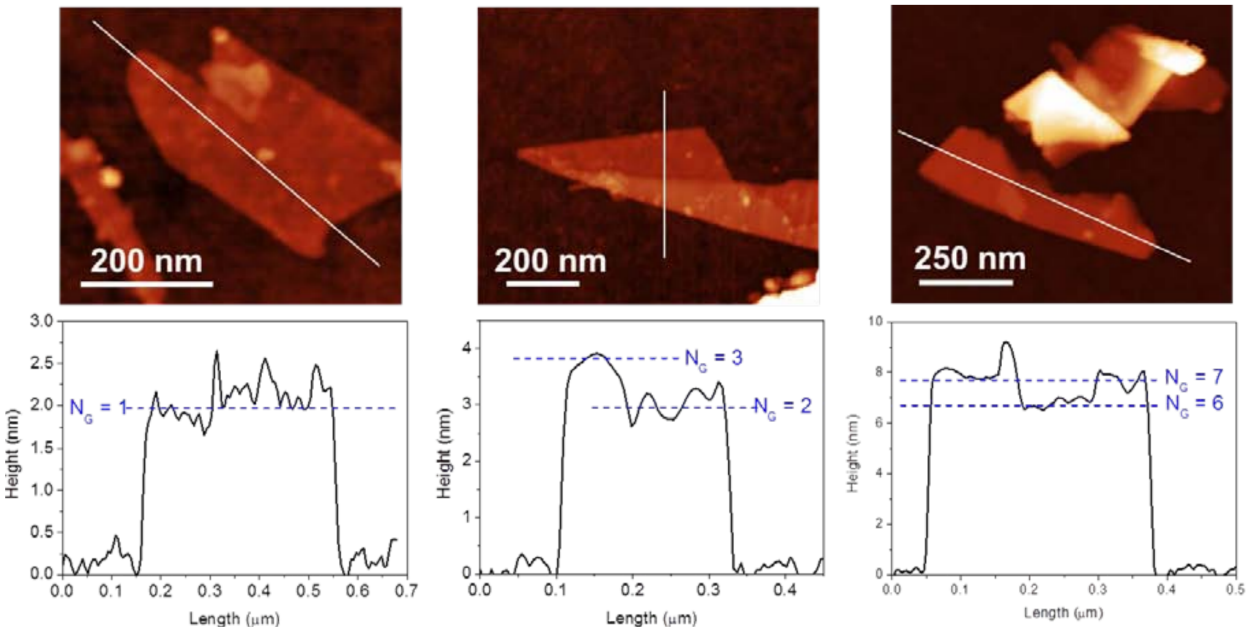

Figure 3.11: Atomic force microscopy (AFM) reference images and associated height profiles for (left to right): monolayer, bi-/trilayer, and few-layer graphene, derived from the study conducted by Paton *et al.* [116]

In contrast, Yao *et al.* measure the thickness of four-layer graphene to be 2.73 nm, which translates to approximately 0.41 nm per layer, considering the thickness of the first layer to be 1.51 nm. The theoretical thickness per layer, approximately 0.35 nm, is lower than the 0.41 nm reported by Yao *et al.*, with the deviation linked to structural and chemical imperfections. [69, 71] The

increased thickness of the first layer, attributed to van der Waals interactions with the substrate, contamination, or defects, is consistent with the findings of Zhao *et al.* [69], which also report an increased initial layer thickness. [69, 71, 126] For ten layers, this results in a thickness of 5.2 nm (9 $\times$ 0.41 nm + 1.51 nm). Therefore, considering both the experimental and theoretical values, the expected thickness for ten layers ranges from 3.96 nm (0.9 nm + 9 $\times$ 0.34 nm) to 5.2 nm.

Paton *et al.* [116] conduct a similar synthesis process to this study, estimating a height of 8.8 nm for ten-layer shear-exfoliated graphene and 0.95 nm for a monolayer, with an surfactant layer thickness of $\sim$1 nm. The observed height of 8.8 nm for ten-layer graphene is significantly greater than the estimated range of 3.96 to 5.2 nm, indicating that the surfactant layer height is inconsistent and thicker than expected.

This finding highlights the importance of isolating graphene to obtain accurate and reliable measurements.

3.3.2 AFM results for graphene produced by the synthesis process in this study

In this study, the Agilent 5400 AFM is utilised, applying a MikroMasch HQ:NSC35/Al BS probe (silicon tips), which operates at resonance frequencies ranging from 150 to 300 kHz.

Figure 3.12 presents the AFM image of graphene produced by shear-mixing graphite in 6 wt.% PAN dissolved in DMF, identified as the most suitable synthesis condition in section 3.2. The observed morphology is more consistent with that of graphene produced by shear-mixing, rather than rGO or hummers' method (see section 3.3.1), despite the higher polymer concentration used in this study. The analysis shows an average height of approximately 3.91 nm $\pm$ 0.45 nm, based on 10 measurements.

As evident from the AFM image, the graphene flakes exhibit an elongated, rectangular morphology rather than a square shape. The calculated layer flake size of 5500 nm, as presented in section 3.2.3, table 3.3, thus refers to the lateral dimensions of the flakes. This interpretation is further supported by the fact that such large flakes, over 10 times the size of the fibre diameters, would not physically fit within the produced fibres. Moreover, the lateral flake size observed in the AFM image is significantly smaller than the calculated value of 5500 nm. While the calculated value, based on an empirical equation, may not be accurate, the AFM image represents vacuum-filtered

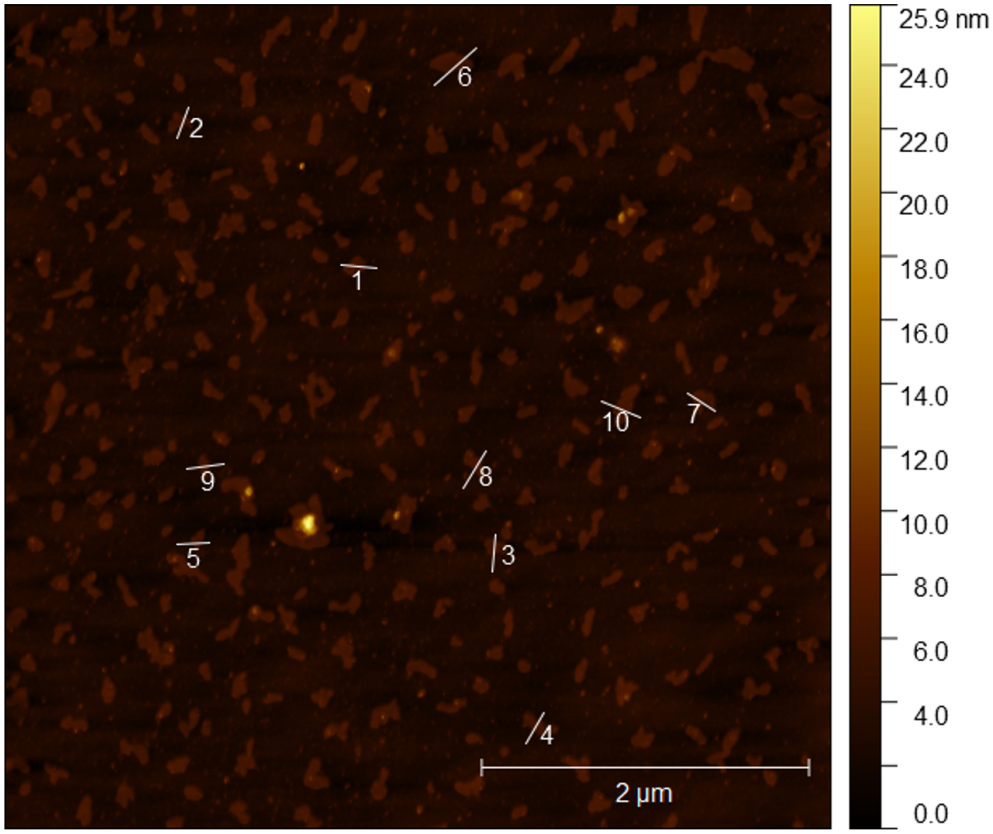

Figure 3.12: AFM image of vacuum-filtrated graphene on a silicon wafer. The graphene, shear-exfoliated in 6 wt.% PAN in DMF, shows an average height of 3.91 nm±0.5 nm from 10 measurements. The graphene flakes exhibit uniform size and consistent lateral dimensions, smaller than those of CVD-grown graphene but larger than those produced by the hummers' method, with lateral dimensions below 500x500 nm. For details on the preparation method, refer to section 3.1.

graphene, where flakes are compressed together and subsequently separated by ultrasonication. This process may have introduced a bias, favouring the detachment of smaller flakes.

The histograms of 3 selected measurements are shown in figure 3.13, highlighting the uniform height distribution of the graphene flakes. The average height of 3.91 nm±0.5 nm aligns well with the established range of 3.96 nm to 5.2 nm, which is considered the maximum height for material to be classified as graphene, corresponding to 10 layers. [61] Raman spectroscopy analysis supports these findings, indicating the presence of few-layer graphene (3-10 layers), with the average number of graphene layers (N_G) determined to be 9±1.5 (section 3.2).

A comparison with Paton *et al.* [116] shows they reported a graphene layer thickness of 6–8 nm for 10 layer graphene with surfactant, which is considerably higher than the measured value

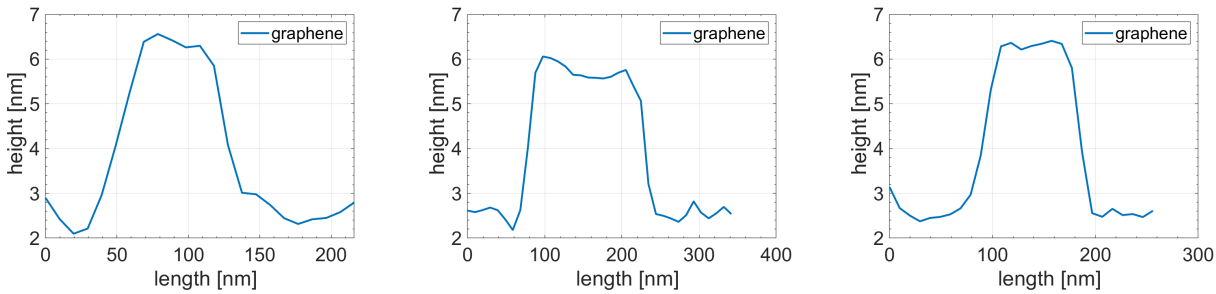

Figure 3.13: Height profiles of measurements 4, 6, and 10 of graphene flakes produced by shear-mixing graphite in 6 wt.% PAN dissolved in DMF, based on the AFM image shown in figure 3.12. The histograms underscore the uniform height distribution of the graphene flakes.

in this study (3.91 nm±0.5 nm). This demonstrates the effectiveness of the vacuum filtration step in removing polymer and achieving accurate results.

3.4 Quantifying graphene concentration via UV-Vis absorption spectroscopy analysis

The ultraviolet-visible (UV-Vis) absorption method is highly effective in determining the concentration of graphene dispersions. [130, 131] Section 3.2 and section 3.3 establish that the produced shear-exfoliated graphene is below 10 layers, classifying it as graphene. [61] The objective is to determine the concentration of this graphene.

3.4.1 Characterisation technique: UV-Vis absorption spectroscopy

In UV-Vis spectroscopy, the absorption and transmission of incident light by the sample are analysed across different wavelengths. The spectrum ranges from 185 nm to 760 nm, corresponding to the ultraviolet-visible (UV-Vis) spectrum. Molecules exhibit distinct absorbance at varying wavelengths due to electronic transitions. In graphene, the UV-Vis spectra result from electron transitions occurring at the carbon π bonds.

Each molecule absorbs light at specific wavelengths respective to its distinctive electronic transitions, with the absorbance A defined as the logarithmic ratio of the incident light intensity I_0 to the transmitted light intensity I, as described in equation 3.5. [130, 131]

$$A = \log_{10}\left(\frac{I_0}{I}\right) \tag{3.5}$$

Graphene characteristically exhibits a stable absorption profile from 500 nm to 800 nm. Consequently, the wavelength of 660 nm is commonly selected for analysis purposes, as the absorption at this wavelength is flat and accurately reflects the graphene concentration: An increase in graphene concentration leads to higher absorption at this wavelength. [132–134] This linear correlation is described by the Beer-Lambert law (equation 3.6), where the absorbance (A) is directly proportional to the concentration of the sample (c), assuming a constant extinction coefficent (ϵ)- a measure of the absorption efficiency of the sample at a particular wavelength - and a fixed path length through the sample (l) at the same wavelength.

$$A = \epsilon \cdot l \cdot c \tag{3.6}$$

As long as the Beer-Lambert law remains applicable, the concentration (c) of a sample can be accurately determined using a concentration calibration curve at the 660 nm wavelength. However, the applicability of the law is restricted to cases with low sample concentrations. At higher concentrations, molecular and ionic interactions can alter charge distributions, thereby affecting absorption characteristics. [130, 131]

3.4.2 Application of the Beer-Lambert law for determining graphene concentration

In this study, UV-Vis absorption spectroscopy is employed to determine the graphene concentration in the centrifuged, shear-mixed solution containing 6 wt.% PAN dissolved in DMF. The UV-Vis spectra in this research are obtained using the Varian Cary 5000.

To facilitate an accurate concentration estimation, a calibration curve is created based on graphene synthesised using the method detailed in Kai et al. (2023) [82], which closely resembles the synthesis process used in this study. Identical experimental parameters are used to shear-exfoliate the same graphite in a solvent without polymer, removing the need for polymer-graphene separation. The similarity in synthesis method provides a solid foundation for the applicability and accuracy of the calibration curve in this study.

The graphene produced in this study is not used to create the calibration curve, as the process requires filtering the graphene-polymer solution to separate the graphene from the polymer, collecting the graphene, and redistributing it in a 6 wt.% PAN polymer solution to accurately determine the graphene concentration. Due to low yields from the vacuum filtration step, there is not enough graphene separated from the PAN+DMF solution for this purpose (see section 3.1). Instead, graphene from the same synthesis process without polymer is employed, as it demonstrates similar characteristics. Initially, a graphene stock solution of 1 mg/ml graphene with a total volume of 2.1 ml is prepared. This stock solution is methodically diluted using the 6 wt.% PAN+DMF solution to obtain various concentration points required for the calibration curve. For example, to obtain a 2 ml solution with a concentration of 0.3 mg/ml, 0.6 ml of the stock solution is mixed with 1.4 ml of the diluent. This dilution process is consistently applied to create all points needed for the calibration curve. As shown in figure 3.14c, the curve covers a concentration range from 0.1 to 0.3 mg/ml, increasing in steps of 0.05 mg/ml. Absorbance-wavelength spectra are used to

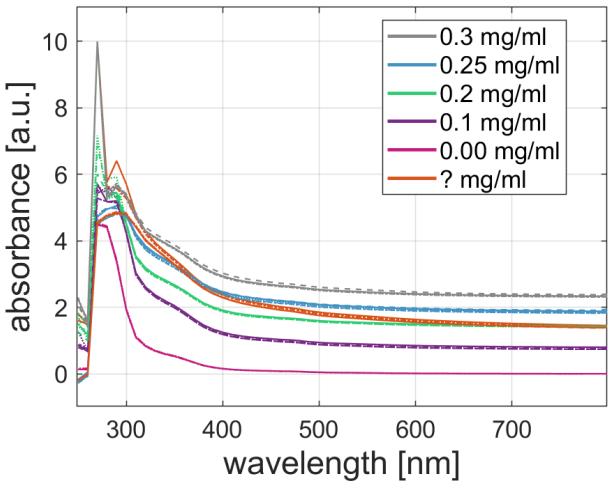

(a) Absorbance-wavelength spectra used to determine the absorbance for the calibration curve and the '?' concentration at 660 nm.

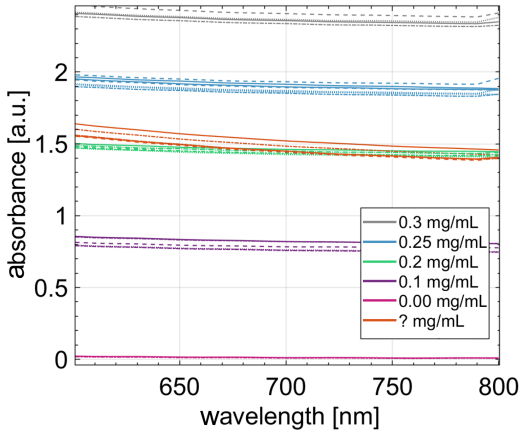

(b) Absorbance-wavelength spectrum showcasing the characteristic flat absorption profile of graphene from 500 nm to 800 nm, resulting from consistent electronic transitions. Absorption at 660 nm is selected for the calibration curve due to its stable absorption characteristics.

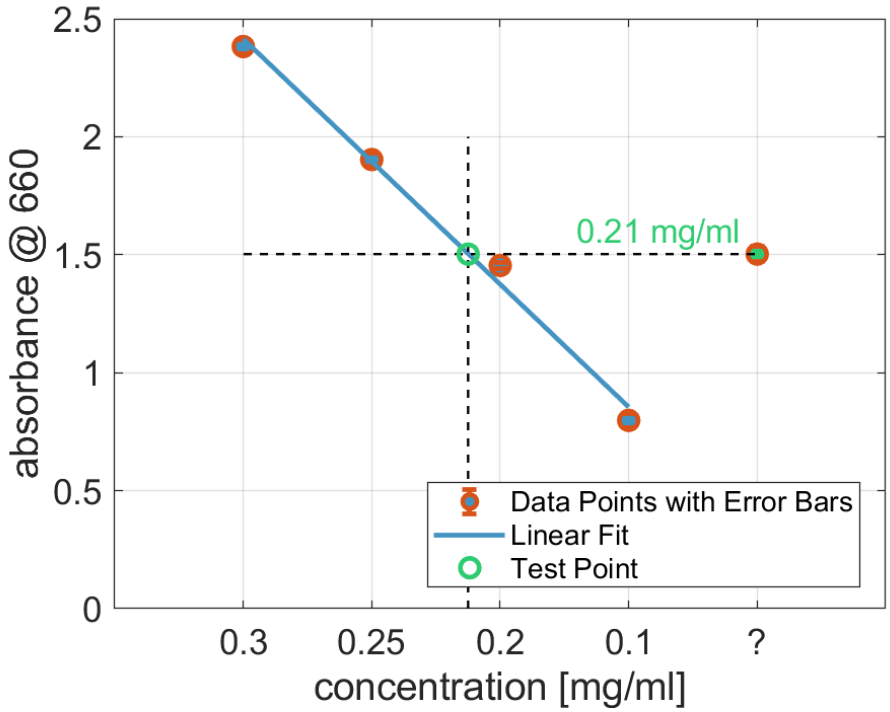

(c) Calibration curve showing the linear relationship between absorbance at 660 nm and graphene concentration, consistent with the Beer-Lambert law. The linear fit line (blue) demonstrates this correlation. The test point (green), marked as '?', represents the graphene concentration obtained from the optimal synthesis condition of shear-exfoliated graphene (based on a 6 wt.% PAN+DMF solution). The error bars (red) represent the standard deviation of the measurements for each data point, with their small size reflecting the high precision of results from three repeated measurements of the same sample.

Figure 3.14: UV-Vis spectroscopy is applied to determine the concentration of shear-exfoliated graphene in a 6 wt.% PAN+DMF solution, labelled '?'. The calibration curve is used to determine the graphene concentration of the '?' solution, resulting in a value of 0.21 mg/ml.

determine absorbance values at 660 nm for both the calibration curve and the 6 wt.% PAN+DMF solution with an unknown graphene concentration, labelled as '?'.

In the UV-Vis measurements, absorbance values are maintained within an optimal order of magnitude ($A < 5$), aligning with the linear range of the Beer-Lambert law. To achieve this, samples are diluted in a 1:1 ratio. This dilution approach is essential for ensuring reliable and reproducible results. Although some absorbance spectra display peak values above 5 (see figure 3.14a), the linear fit of the calibration curve (figure 3.14c) indicates that the Beer-Lambert law remains applicable throughout the measured range.

The absorption curve of the 6 wt.% PAN+graphene+DMF solution produced in this study, labelled as '?', and shown in red in figure 3.14b, exhibits a distinct slope and absorption behaviour before 650 nm compared to the 6 wt.% PAN+graphene+DMF solution prepared with redispersed graphene using the method described in [82], whose absorbance spectra are used for the calibration curve. However, this deviation does not affect the absorption at 660 nm, the point used for creating the calibration curve and used to determine the graphene concentration. These differences, as previously suggested by the AFM analysis (section 3.3.2), could be ascribed to changes in the morphology of graphene, notably the decreased lateral dimensions (below 500x300 nm) relative to those reported by Kai*et al.*, which are approximately 1000x500 nm. [82]

In conclusion, using the calibration curve to correlate absorbance with concentration, the UV-Vis analysis estimates a graphene concentration of 0.21 mg/ml in the synthesised 6 wt.% PAN+graphene+DMF solution from this study, as illustrated in figure 3.14c.

4

Advanced thermogravimetric analysis for graphene characterisation

This chapter evaluates the use of thermogravimetric analysis (TGA) as a method for assessing both the quality and concentration of graphene within composite materials. The objective is to determine whether advanced TGA can effectively replace or supplement existing, more labor-intensive analysis techniques like Raman spectroscopy, UV-Vis absorption spectroscopy and AFM in the study of composite materials incorporating graphene.

4.1 Characterisation technique: thermogravimetric analysis

The standard thermogravimetric analysis (TGA) examines the weight of a material during a heating process at a specific heating rate. In this study, TGA is conducted under an air atmosphere. The weight loss in % over a specific temperature range in °C is measured. This weight loss offers valuable information regarding the nature and quantity of components present in the material under study. Detected weight loss can primarily be attributed to actual loss of mass from thermal decomposition or the evaporation of residual solvents. However, weight changes may also reflect structural transformations, such as changes in crystal structure or melting. While these transitions do not directly cause significant mass loss, they can affect the thermal stability

of the material or facilitate the release of volatiles. Recognising these factors is crucial for accurately interpreting material composition and behaviour. [135]

In thermogravimetric analysis (TGA), components with similar thermal properties often merge in the TGA curve, making them indistinguishable. To resolve this, the first derivative (-DTG) of the curve is calculated. DTG visualises the incline rates of the curve: -DTG peak maxima represent the maximal rate of weight change. Each peak reveals a seperate weight loss event. To further aid in the identification process of weight loss events, the second derivative (-DTG2) of the TGA curve is calculated. Specifically, the zero crossings of the -DTG2 curve correspond to the peak maxima in the -DTG curve. Additionally, the beginning and ending of weight loss events, as indicated in the -DTG curve, are marked by the peak maxima and minima, respectively, in the -DTG2 curve. This approach enables the separation and identification of individual weight loss events, even those that are minor or overlapping.

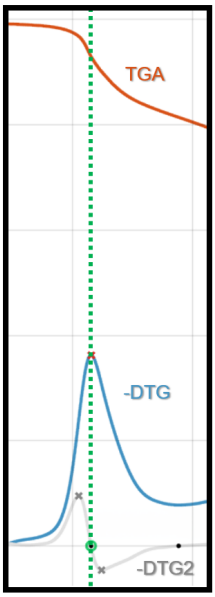

Figure 4.1: Visualising the relationship between TGA and its derivatives (-DTG, -DTG2) on the example of a single-component TGA curve. The red curve represents the TGA data showing weight loss with increasing temperature. The blue -DTG curve indicates weight loss events with each peak, while the grey -DTG2 curve highlights the rate of weight change. The green point marks the maximum rate of weight change, corresponding with the red 'x' and the maxima of the -DTG curve. Grey 'x' marks on the -DTG2 curve indicate the start and end of weight loss processes.

-DTG and -DTG2 are crucial for revealing these overlapping weight loss events that are not apparent in the standard TGA curve. Notably, -DTG never reaches a zero point, indicating that weight loss

processes always have some degree of overlap. The previously described methodology for identifying weight loss events is illustrated in figure 4.1, showing how -DTG and -DTG2 curves enable the identification of weight loss processes of individual components within a composite material. [135]

4.2 Advanced TG analysis: addition of deconvolution for overlapping peaks

When DTG peaks strongly overlap, deconvolution becomes essential for determining the contributions of different components to a weight loss event. This nonstandard approach enables the differentiation and identification of components with similar weight loss characteristics. [77, 136] The method to deconvolute -DTG data peaks is structured around three key elements: the shape of the peaks (lineshape), the method used to fit these peaks (fitting algorithm), and handling the background data (background algorithm).

The deconvolution of DTG data is performed using a MATLAB script, initially based on the open-source code in [137]. This script, initially designed for general peak fitting and well-suited for Raman spectroscopy data, has been adapted for thermogravimetric analysis, incorporating both the first and second derivatives to improve the analysis of decomposition events. Significant modifications have been implemented to enhance its functionality and tailor it to the specific requirements of TGA data interpretation. These modifications include optimising the visual presentation of output graphs to enhance interpretability, integrating advanced baseline fitting algorithms to improve accuracy in analysing complex datasets, incorporating additional lineshape models to expand fitting flexibility, and implementing root mean square error (RMSE) to quantitatively assess fit quality. [137, 138]

4.2.1 Fitting algorithm

The fitting model is constructed from various component peaks, each defined by specific lineshapes and parameters ($\vec{\theta}$), including position, full width at half maximum (FWHM), and area. The goal of the fitting process is to optimise these parameters to align the model closely with measured data. To achieve this, the nonlinear least squares method is applied, utilising the Levenberg-Marquardt algorithm for iterative optimisation.

The nonlinear least squares method aims to find the model parameter values that minimise the sum of the squares of the differences (errors /SEE) between the measured data and the model data. Mathematically, this can be expressed as:

$$\text{SSE} = \sum_{i=1}^{m} [y_i - f(x_i, \vec{\theta})]^2 \tag{4.1}$$

where y_i are the measured data, $f(x_i, \vec{\theta})$ is the model function at x_i with parameters $\vec{\theta}$, and m is the number of data points.
Utilised for solving nonlinear least squares problems, the Levenberg-Marquardt algorithm iteratively adjusts parameters from starting model estimates towards an optimal fit. This algorithm merges the principles of gradient descent with the Gauss-Newton method, making it highly effective for complex parameter optimisation.

- **Gradient descent**: This method adjusts parameters based of the steepest decrease of the SSE, utilising the derivatives of the function. Predominantly effective for correcting parameters that initially are far from their optimum.

- **Gauss-Newton**: This method assumes the SSE function is locally quadratic and finds its minimum, facilitating rapid convergence. Its utility is limited by its initial position dependency, failing to converge when initial estimates are too far from the optimal values.

The transition between these methods is controlled by the damping factor, λ, which is dynamically adjusted during the iterations. Large λ values lead to gradient descent behaviour, while small λ values promote the Gauss-Newton method. This combination of methods enables an adaptive fitting process that is robust against common challenges, such as inaccurate starting parameter estimates. [138–140]

Gaussian lineshape for -DTG fitting

In thermogravimetric analysis, the combination of Gaussian lineshaped peaks is especially suited for fitting the first derivative of the TG curve. Its symmetric, bell-shaped profile closely aligns with the typical weight loss rate patterns observed in materials during thermal decomposition.

The Gaussian distribution accurately captures the peak, where the rate of weight loss is highest, and effectively represents the spread of data, reflecting material variations and deviations.
In contrast, the Lorentzian lineshape, with its narrower peak and extended wings, may not align well with the thermal decomposition profiles observed in TGA. [141, 142]

Baseline fit: maxima interpolation

In TGA, the baseline fit plays a crucial role in isolating specific peak contributions and correcting for baseline drift. This fitting is essential for comparative analysis and quantifying the percentage weight loss of each component. A well-defined baseline facilitates the accurate interpretation of TGA data.
The modified Akima piecewise cubic Hermite interpolation is employed for the baseline fit, which is interpolated from manually selected points and then applied to the data. This method is characterised by its balanced undulation, avoiding the extremes of being overly wavy ('spline interpolation') or flat ('pchip interpolation'). It also handles edge cases effectively without introducing unrealistic features in the curve. The piecewise cubic approach (equations of the third degree) creates smooth curves between each pair of points.
The maxima interpolation involves following steps:
For a set of data points (x_i, y_i), the slope δ_i between each consecutive pair of points is calculated as:

$$\delta_i = \frac{y_{i+1} - y_i}{x_{i+1} - x_i} \tag{4.2}$$

The algorithm then determines the derivative at each data point as a weighted average of adjacent slopes. The derivative at point x_i, denoted as d_i, is given by:

$$d_i = \frac{w_1 \delta_{i-1} + w_2 \delta_i}{w_1 + w_2} \tag{4.3}$$

where w_1 and w_2 are weights calculated to effectively manage flat areas within the dataset and minimise overshooting in the resulting interpolated curve. The weights are defined as follows:

$$w_1 = |\delta_{i+1} - \delta_i| + \frac{|\delta_{i+1} + \delta_i|}{2} \tag{4.4}$$

$$w_2 = |\delta_{i-1} - \delta_{i-2}| + \frac{|\delta_{i-1} + \delta_{i-2}|}{2} \tag{4.5}$$

With the derivatives calculated, the algorithm forms the interpolated curve. In each interval between data points, a cubic polynomial is applied, aligning with the calculated derivatives at the endpoints, which ensures a smooth transition across the entire set of data. [143]

4.3 TGA: literature and established thermal decomposition profiles

This study reviews the published decomposition patterns of polyacrylonitrile (PAN) and various carbon-based materials, such as GO, rGO, and graphite. The objective is to identify peak decomposition events specific to PAN and graphene, facilitating the clear identification of graphene while excluding other potential contributors. The studied material is composed of PAN and graphene, as validated in chapter 2 and section 3.2. This review is obligatory for establishing a baseline understanding of their typical thermal decomposition patterns, thereby enabling accurate comparison and allocation of peaks in the measured data.

4.3.1 PAN decomposition dynamics

Several characteristic weight loss stages for PAN are reported in literature. One such stage occurs around 100 °C, and is attributed to the removal of moisture from the PAN material. [144]
Another key event, known as stabilisation, marks a critical structural change in PAN and typically takes place at temperatures below 400 °C in an air atmosphere. This stage is relevant to the TGA experiments, as it aligns with the experimental conditions used in this study. In general, stabilisation enhances the thermal stability of PAN, as it leads to the formation of ladder-like molecular structures, thereby minimising mass loss, dimensional shrinkage, and volatilisation at temperatures above 400 °C. This process involves various reactions including oxidation, cyclisation, crosslinking, aromatisation, and dehydrogenation, with the dominant reaction being temperature-dependent. Figure 4.2 presents this stabilisation process.
The dominant reaction below 200 °C is dehydrogenation: hydrogen leaves the material, typically through forming a water molecule with another molecule-hydrogen and one external oxygen. The result is a double bond between two carbons and a reduction of the methylene groups (CH_2). Depending on the temperature, dehydrogenation can occur before, after, and simultaneously to

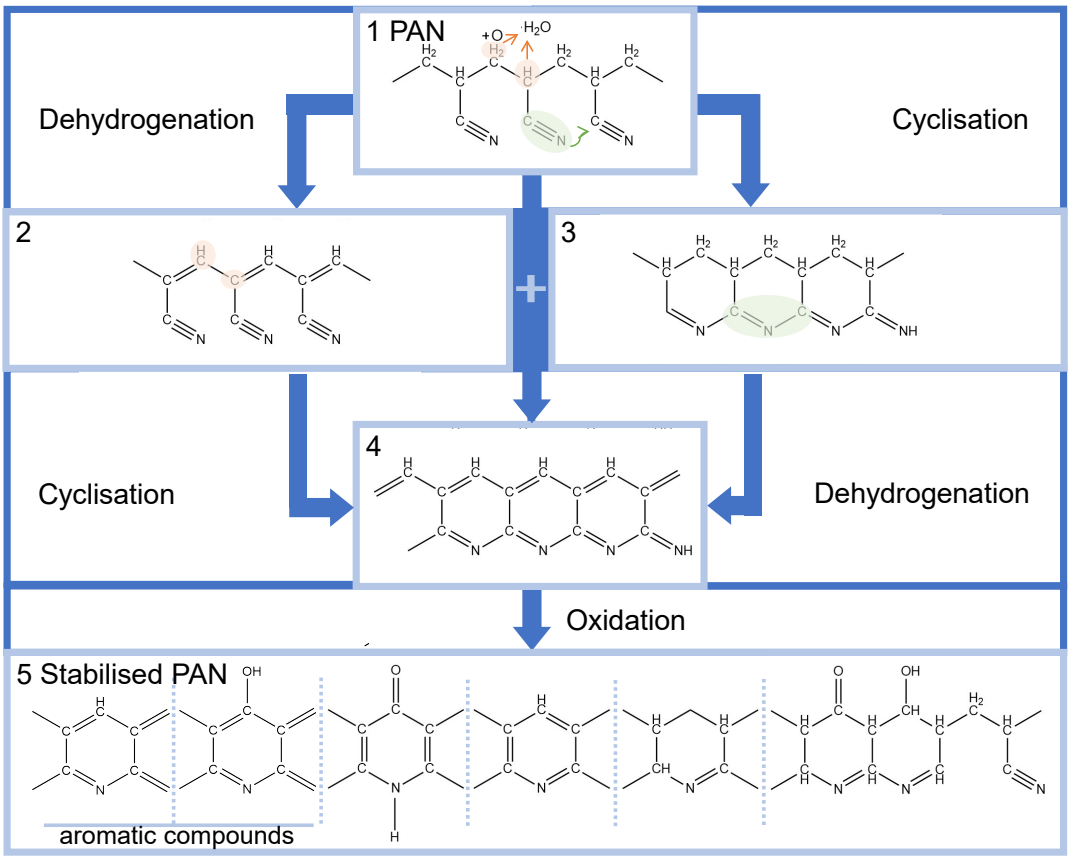

Figure 4.2: Stabilisation process of PAN at temperatures below 400 °C → 1: Original PAN-molecule; Variant 2+4: Dehydrogenation followed by cyclisation; Variant 3+4: Cyclisation followed by dehydrogenation; 4: Cyclisation simultaneous with dehydrogenation; 5: Oxidation results in stabilised PAN. [10, 145–147]

the cyclisation process. [10, 145, 146] For temperatures between 200 °C and 250 °C, cyclisation is the dominating reaction. In the cyclisation reaction, a nitrile bond (C≡N) forms a double bond with an adjacent carbon atom. This is an exothermic reaction. [146]

Oxidation occurs in the temperature range from 300 °C to 400 °C. The oxidation reaction forms carbonyl groups (C=O) and C-OH units. Molecular building blocks containing carbonyl groups appear in ca 40 % of the molecule. In this temperature range, aromatisation and intermolecular crosslinking reactions also start to take place because oxygen promotes these reactions.

Aromatisation is based on the formation of an aromatic compound with alternating single and double covalent bonds. In this reaction, one external oxygen reacts with two hydrogen atoms, which were bonded to the carbon. At this stage, the molecular chains in PAN exhibit improved alignment and begin to partially form ladder-like structures (figure 4.2, **5**). [145–147]

Beyond the temperature of 400 °C, the material enters its decomposition phase, signifying a critical transition in its thermal behavior. [135]

4.3.2 Thermal behaviour of carbon-based materials

Recent findings reveal that a considerable amount of what is sold as graphene on the market does not meet the scientific criteria for being classified as graphene. This is primarily attributed to factors such as a high content of sp^3-hybridised carbon or defect density. [61, 76] In light of this, TGA is being explored as a time-efficient and economical approach to accurately identify various carbon-based materials. Figure 4.3 provides a comprehensive overview of the decomposition patterns observed in these materials. It is important to note that the decomposition temperatures for each material, such as amorphous carbon (AC), graphene oxide (GO), reduced graphene oxide (rGO), carbon black (CB), graphene, and graphite, are presented as ranges. The ranges reflect various influencing factors, such as the equipment specifications, sample weight, heating rate, and material quality. This underscores the necessity of conducting measurements under specific, controlled experimental conditions to obtain accurate reference data.

Despite these temperature ranges, research findings indicate distinct decomposition patterns among carbon-based materials. Unlike graphene and graphite, materials such as amorphous carbon (AC), graphene oxide (GO), reduced graphene oxide (rGO), and carbon black (CB) generally decompose at temperatures below 650 °C. [72,75–77] This lower decomposition temperature is often explained by structural damage and variations from the typical hexagonal carbon structure. [55, 62, 63]

While most of these materials decompose within a similar temperature range, AC is an exception by decomposing at a significantly lower temperature, around 350 °C. Notably, graphene oxide uniquely exhibits two distinct decomposition peaks at around 180-220 °C and 530-620 °C.

In contrast, graphene and graphite exhibit distinct decomposition temperature ranges, at 659–730 °C and 830–949 °C respectively, without any overlap. This difference in decomposition temperatures is primarily attributed to the variation in layer thickness.

In graphite, numerous graphene layers are stacked and bonded by van der Waals forces, forming a dense three-dimensional structure that reduces surface area-to-volume ratio and enhances thermal stability compared to single-layer graphene. [72, 77] This suggests a direct correlation between

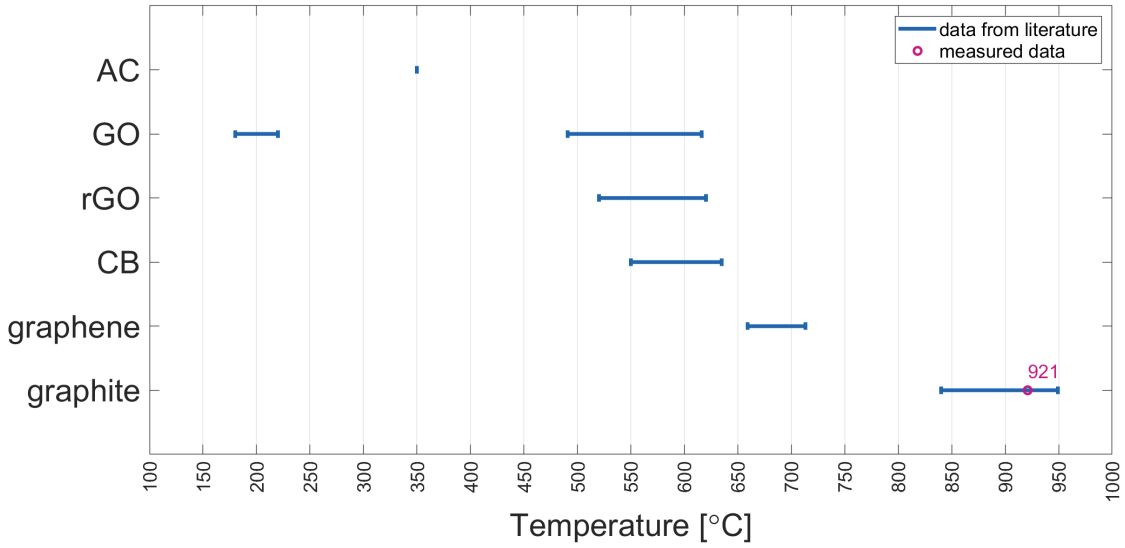

Figure 4.3: Decomposition patterns of various carbon-based materials derived from TGA, including amorphous carbon (AC), graphene oxide (GO), reduced graphene oxide (rGO), carbon black (CB), graphene, and graphite. Temperatures for mass loss events at maximum weight loss rates are presented as ranges (blue), reflecting factors such as equipment specifications and material quality. Graphene decomposes at lower temperatures compared to graphite, correlating with layer thickness. [72, 75–77] One measured temperature point (pink) is included as an example, showing that the graphite used in this study is within the expected range.

the decomposition temperature and the number of stacked graphene layers: the decomposition temperature increases with greater number of graphene layers. This observation leads to an exploration of the potential of TGA in estimating the layer size of graphene, a question addressed later in this chapter.

In summary, when examining pure carbon-based materials, TGA appears to be a viable method for accurately identifying graphene based on established decomposition ranges, as presented in figure 4.3. [72, 75–77] To validate the reliability of this approach, TGA has been conducted on graphite, which decomposed at 921 °C, falling within the expected range. This method presents a practical approach for the simple verification of the quality of commercially purchased graphene, a crucial need given the current variability in graphene quality. [61, 76]

4.4 Graphene quality assessment through advanced TGA

This section evaluates the use of advanced TGA to determine the concentration and quality of graphene in PAN composites. As confirmed in section 3.2, Raman spectroscopy shows the shear-exfoliated graphene produced in this study consists of 3 to 10 layers, with an average of 9 layers, classifying it as graphene. [61]

4.4.1 Reproducibility study at different heating rates

Reproducibility is evaluated using the same PAN polymer specimen (∼7-8 mg per test), tested three times at two different heating rates (1 °C/min and 5 °C/min). This approach is designed to understand the influence of heating rates on the resolution of degradation (DTG) peaks and to determine the optimal parameters for TG analysis. The Pyris TGA 8000 from Perkin Elmer is utilised for conducting the experiments.

All tests are conducted by heating the studied specimen from 30 °C to 1000 °C in an air atmosphere at a flow rate of 40 ml/min. The data are normalised to present weight loss as a percentage, ensuring accurate comparison across samples.

The analysis, depicted in figure 4.4, demonstrates the reproducibility of thermal measurements at heating rates of 1 °C/min and 5 °C/min, revealing a maximum deviation of approximately 5%. This level of consistency across repeated measurements affirms the reliability of the experimental data. Hence, the findings signify that both heating rates provide reliable and reproducible results. The comparison between heating rates reveals that a rate of 1 °C/min significantly enhances DTG peak resolution and reduces peak overlap, as demonstrated in figure 4.5.

Notably, at the 1 °C/min heating rate, two distinct peaks within the 250-450 °C range are clearly visible, in contrast to the overlapping peaks observed at a 5 °C/min heating rate. Thus, it can be concluded that employing a lower heating rate yields a more precise and accurate thermal analysis. [76]

This benefit comes at the cost of increased testing duration - 16.17 hours for 1 °C/min compared to just 3.24 hours for the heating rate of 5 °C/min. The heating rate of 5 °C, established as the standard heating rate in the literature [77, 135, 136], offers a balance between resolution and efficiency with a testing duration.

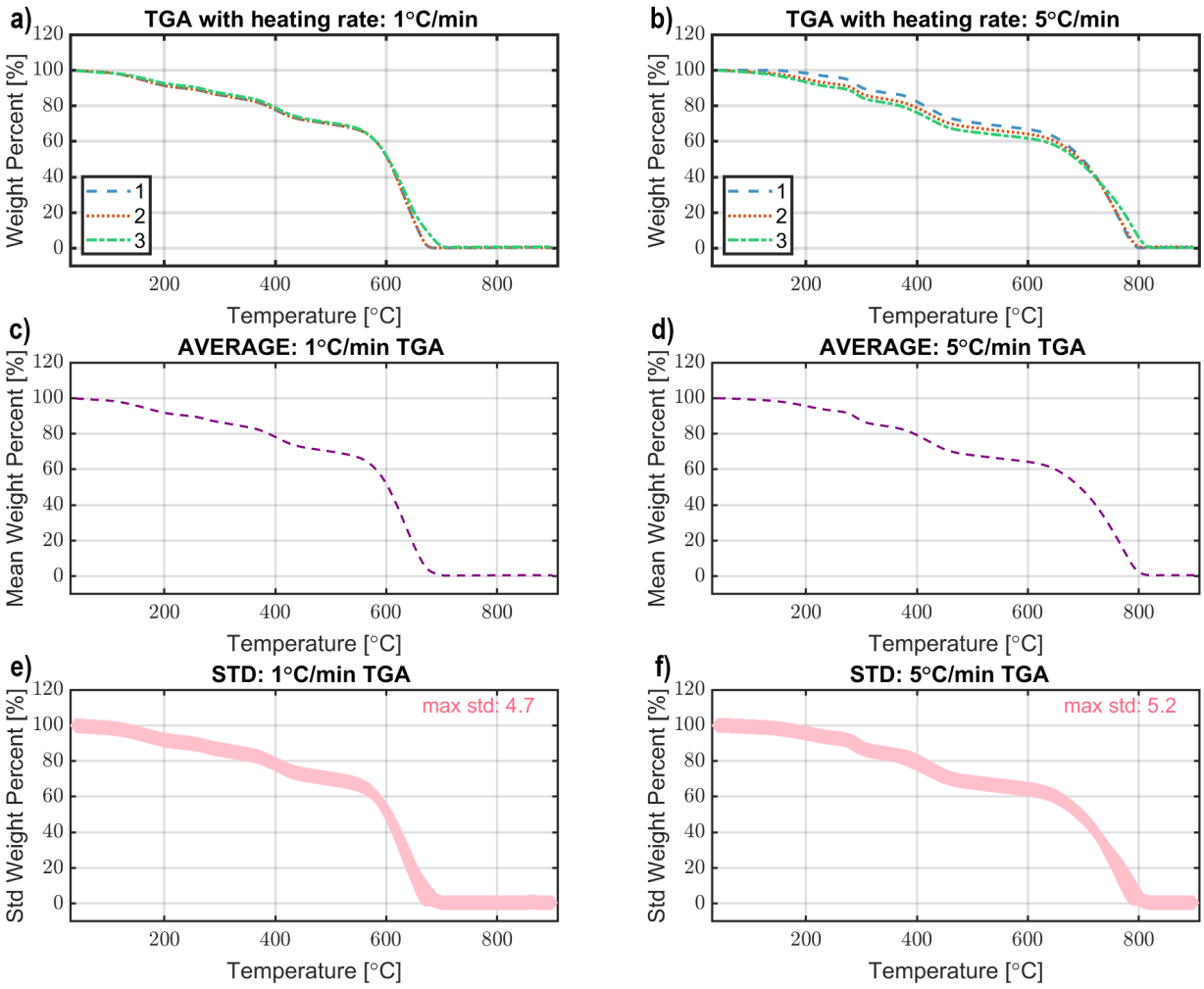

Figure 4.4: TGA curve reproducibility at 1°C/min (a, c, e) and 5°C/min (b, d, f) heating rates: (a, b) TGA curves for PAN polymer (3 measurements), (c, d) average of these curves, (e, f) point-by-point standard deviation, showing max STD of 4.7% (e) and 5.2% (f), affirming data reproducibility.

The comparative analysis reveales a significant 15-22% variation in the decomposition patterns between the heating rates of 1 °C/min and 5 °C/min. Given this, the 1 °C/min rate is determined to be more effective for identifying overlapping mass loss events of carbon-based materials with similar thermal properties, hence offering a more accurate representation of their thermal behavior. [76] Therefore, the lower rate is adopted for subsequent work. These findings underscore the importance of using in-house made reference measurements and advise caution when comparing the data with literature.

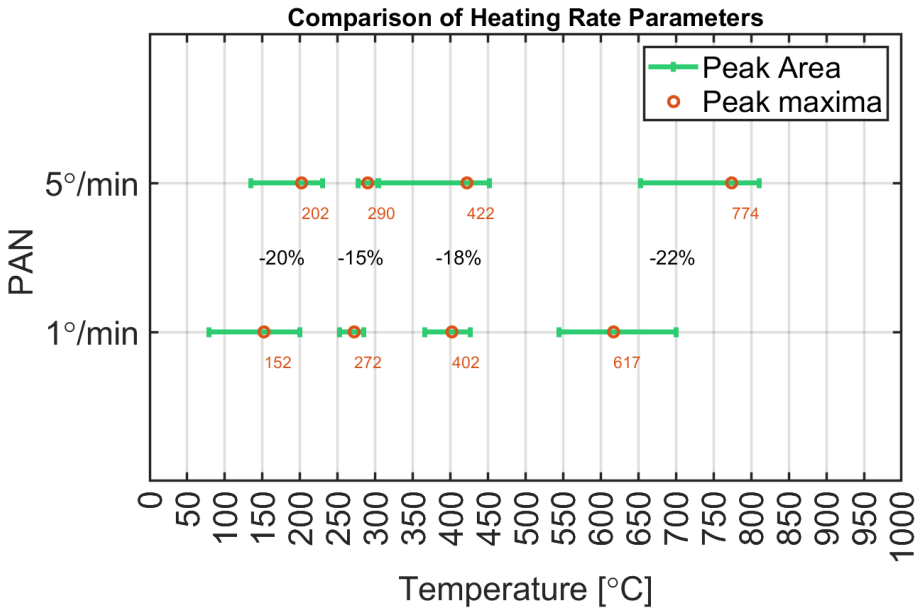

Figure 4.5: Comparison of decomposition patterns at 1°C/min and 5°C/min heating rates: depicts peak ranges and maxima with differences up to 22%, highlighting the higher accuracy of the 1°C/min rate in representing decomposition behaviors. The results are derived from the TGA graph in figure 4.4, using the method detailed in 4.1.

4.4.2 Reference standards

To accurately evaluate the contributions of individual components within the PAN-graphene composite, decomposition profiles for shear-exfoliated graphene and pure polyacrylonitrile (PAN) are established as reference standards.

Reference 1: shear-exfoliated graphene

TGA conducted on reference graphene, prepared as per Kai *et al.* (2023) [82], provides a reference thermal decomposition profile for shear-mixed produced graphene, as shown in figure 4.6. This analysis, at a 1 °C/min heating rate, identifies three major mass loss events: initial moisture and impurities removal (1), followed by the thermal decomposition of graphene at 412 °C (2) and 730 °C (3) peak maxima. The 20 % weight loss at 412 °C (peak 2), an outcome not previously documented in literature (section 4.3.2), presents a unique occurrence. This particular second peak, absent for graphene synthesised by other methods, suggests a direct link with the shear-mixing production technique.

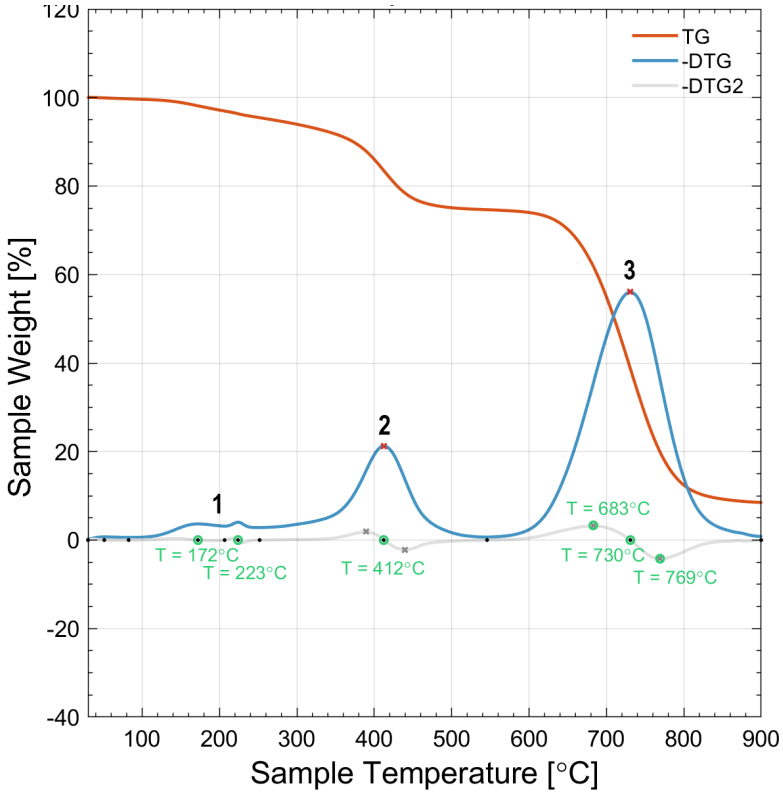

Figure 4.6: Reference 1 – TGA of shear-exfoliated graphene (Kai *et al.*, 2023 [82]): displays three mass loss events, highlighted by -DTG peaks and the corresponding -DTG2 curve. Conducted at a heating rate of 1°C/min. Notably, the 20% mass loss observed at 412 °C has not been previously documented in literature (section 4.3.2). This second peak is specific to shear-mixed graphene, indicating a direct link to the production method.

Shear forces introduce defects in shear-exfoliated graphene flakes, potentially disrupting the hexagonal carbon structure (section 3.2.3). Defects in graphene, being more chemically reactive than the pristine lattice, could serve as initiation sites for oxidation and combustion at elevated temperatures, resulting in a 20 % weight loss. This is of a similar order of magnitude as the ∼10 % oxidation-induced weight loss observed in PAN (see section 4.3.1), supporting the plausibility of this assumption. Additionally, the thermal behavior of shear-mixed reference graphene at 412 °C, when compared to the oxidation patterns of PAN in the same temperature range, suggests that this mass loss event may be driven by oxidation processes. Oxidation at the defects of graphene could introduce oxygen-containing functional groups, such as hydroxyl, epoxy, and carboxyl, altering its chemical and physical properties. This modification potentially accounts for the reference graphene position at the higher end of the thermal decomposition range for

graphene, a range established by existing literature graphene (section 4.3.2).

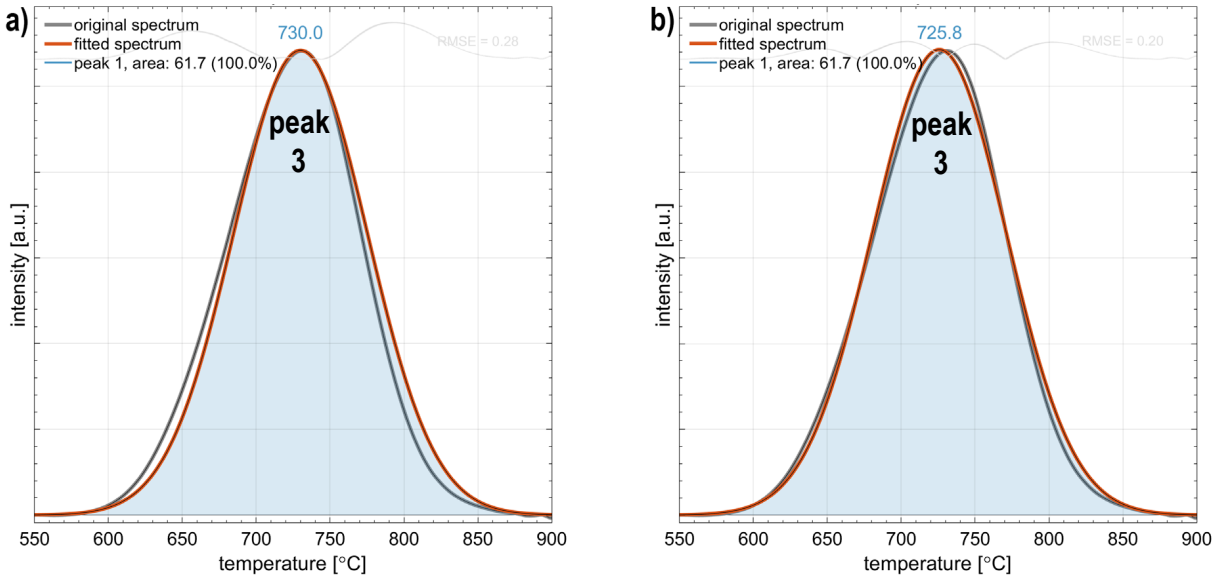

Figure 4.7: Comparison of two Gaussian lineshape fits for the last decomposition peak (3) of reference shear-exfolaited graphene (figure 4.6): a) Constrained fit at the empirically validated 730 °C peak maximum and b) Optimal model fit at 725.8 °C peak maximum. Grey represents the original spectrum, red denotes the fitted spectrum, and blue highlights the peak area. Adjusting the model to the empirically-validated maximum of the peak results in a higher RMSE of 0.28 compared to 0.2 for a peak at 725.8 °C, indicating slight asymmetry. The Gaussian lineshape is a valid approximation for modeling the -DTG decomposition peak, but these limitations should be considered.

Figure 4.7 a) demonstrates the Gaussian fit applied to the third mass loss event of reference graphene, showing a distinct decomposition component peaking at 730 °C, as -DTG2 analysis with a single maximum and minimum suggests (figure 4.6). However, adjusting the model to this empirically-validated peak maximum leads to a higher root mean square error (RMSE) of 0.28, compared to 0.2 for an peak maximum at 725.8 °C (figure 4.7 b), indicating slight peak asymmetry with tailing to the right. Nevertheless, the Gaussian lineshape provides a valid approximation for modeling the -DTG decomposition peak. Such findings highlight that model fits, while useful, are approximations that may not fully capture the complexities of thermal decomposition processes. In some instances, a higher RMSE can offer a closer representation of the actual decomposition process.

Reference 2: pure PAN

TGA of the pure dried PAN-solution, illustrated in figure 4.8, serves as a key reference point for this study. Conducted with a heating rate of 1 °C/min, TGA reveals four distinct mass loss events: moisture loss (1), dehydrogenation and cyclisation (2), oxidation (3), and decomposition (4), coherent with the decomposition dynamics discussed in section 4.3.1.

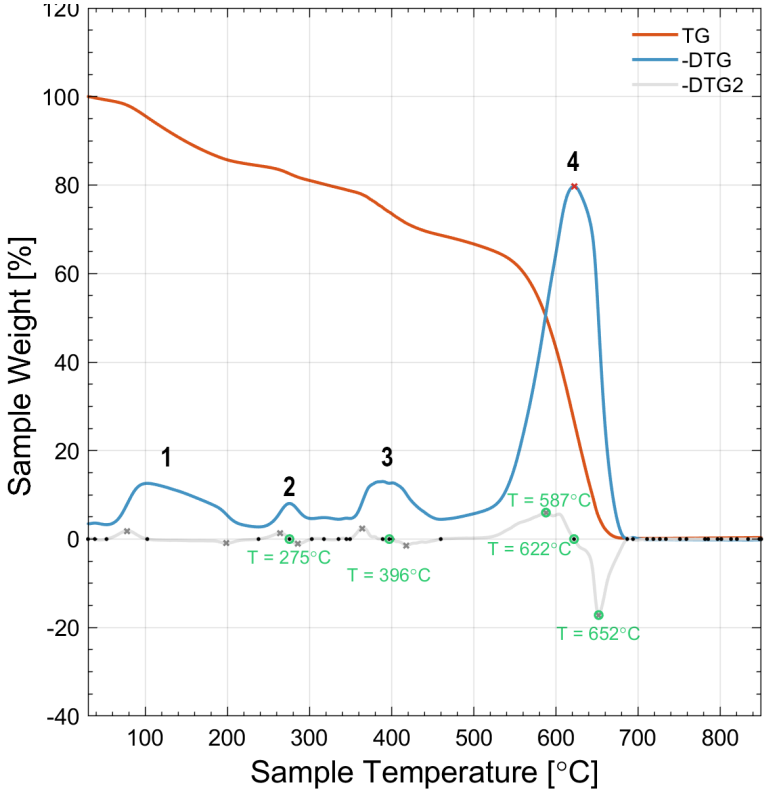

Figure 4.8: Reference 2 – TGA of pure dried PAN-solution: displays the thermal decomposition profile with corresponding -DTG and -DTG2 curves. Conducted at a heating rate of 1 °C/min. Key observations include: 1. peak (∼100 °C) corresponding to moisture removal, 2. peak (275 °C) indicating thermal stabilisation, 3. peak (396 °C) representing oxidation, and 4. peak (622 °C) signaling decomposition.

Complete thermal degradation (4), accounting for 70 % of the weight loss, is observed by 652 °C, with a noticeable right-skewed asymmetry in the final decomposition peak. Here, the -DTG2 analysis suggests between two and three decomposition events, reflected in deviations from the standard curve progression (figure 4.1) and the presence of at least two local maxima and minima. Building on this, the peak deconvolution of the fourth -DTG decomposition peak is explored with one, two, and three peaks.

Figure 4.9 reveals that the single peak model (a), with an RMSE of 1.05, fails to accurately represent the data, whereas a two-peak model (b) significantly improves fit with an RMSE of 0.22. However, the three-peak model (c), providing the best fit with an RMSE of 0.1, most accurately captures the decomposition behavior of PAN, thereby suggesting three distinct stages in its thermal breakdown.

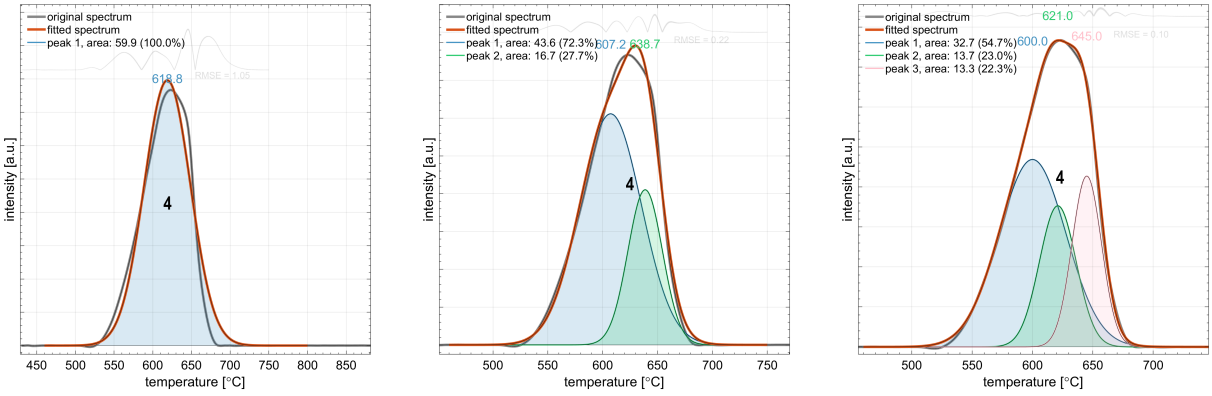

Figure 4.9: Model fit for fourth -DTG peak of dried PAN-solution: demonstrates fits with one peak (a), two peaks (b), and three peaks (c), highlighting the increasing accuracy. The three-peak model, with an RMSE of 0.1, best represents the decomposition behavior, indicating three distinct stages in the thermal breakdown of PAN.

4.4.3 Deriving insights from advanced TGA: a comparative study

Three comparative studies are conducted. The first examines the impact of graphite and graphene on PAN composites, the second investigates the effect of varying PAN concentration during shear-mixing on PAN+graphene composites, and the third provides a comparative analysis with commercial graphene.

Study 1: dried 6 wt.% PAN+graphene solution before and after centrifugation

Figure 4.10 (a) presents the TGA of dried 6 wt.% PAN+graphene solution, illustrating a profile shaped by contributions from both PAN and graphene. The synthesis of graphene via shear-mixing in a 6 wt.% solution is identified as the optimal synthesis condition, as demonstrated in chapter 2 and section 3.2. The TG analysis presents four distinct mass loss events that align with known behaviors of the reference materials: initial moisture and impurities removal (1), PAN

dehydrogenation and cyclisation (stabilisation) (2), followed by two overlapping events attributed to both PAN and graphene oxidation (3) and decomposition (4), respectively.

To assess the effectiveness of graphite removal via centrifugation in the PAN+graphene composite and its impact on thermal behaviour, the TGA results of the dried 6 wt.% PAN+graphene solution are analysed before and after centrifugation (figure 4.10). The decomposition after centrifugation in figure 4.10 (a) concludes at 650 °C, indicating no further weight loss, whereas in figure 4.10 (b), pre-centrifugation decomposition continues beyond this temperature due to differences in material composition.

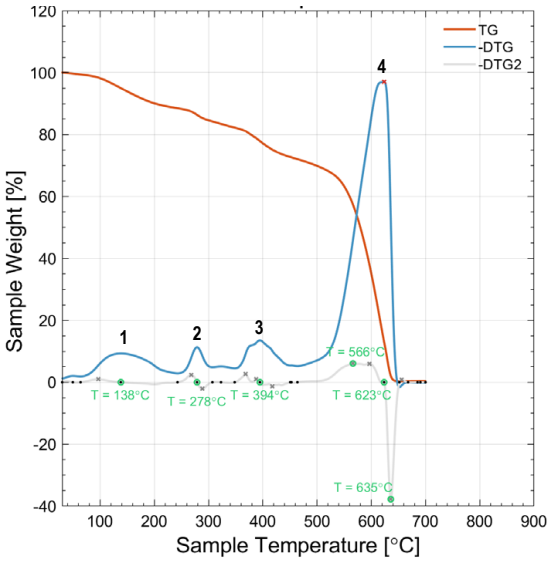

(a) TGA of dried 6 wt% PAN+graphene solution after centrifugation.

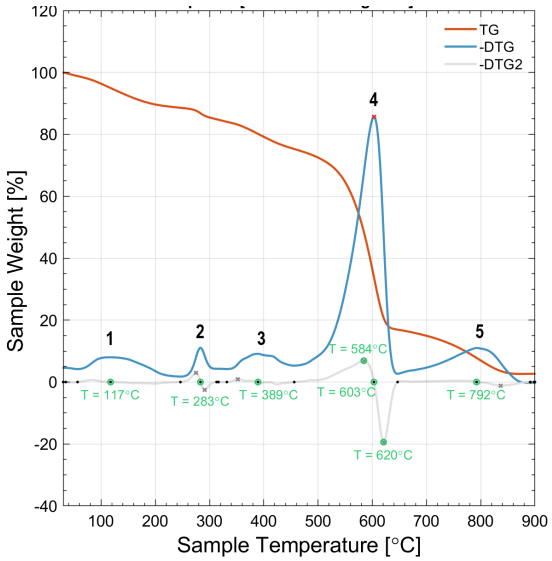

(b) TGA of dried 6 wt.% PAN+graphene solution before centrifugation.

Figure 4.10: TGA of dried 6 wt.% PAN+graphene solution after (a) and before (b) centrifugation, conducted at a 1 °C/min heating rate. The pre-centrifugation TGA presents a fifth peak at 792 °C, indicative of graphite. Post-centrifugation (a), the absence of a fifth peak confirms the successful removal of graphite: the decomposition process concludes at approximately 635 °C, beyond which no additional weight loss can occur, signifying the completion of all possible thermal events. Consequently, the temperature measurement is terminated at this point, as the thermal decomposition of the sample has been fully recorded.

The pre-centrifugation TGA shows a distinct fifth peak at 792 °C with a 10 % weight loss (figure 4.10 (b), signifying residual graphite, multilayer graphene ($\geq$10 layers) and graphene decomposition. This decomposition phase ends at 875 °C, consistent with the starting temperature for graphite decomposition reported in the literature (section 4.3.2). The result implies that shear-mixing significantly reduced the layer size of most graphite flakes, promoting earlier thermal breakdown.

Notably, the TG analysis reveals that the presence of graphene, multilayer graphene ($\geq$10 layers) and graphite creates two seperate mass loss events (fourth and fifth -DTG peaks). Without this multilayer-graphene ($\geq$10 layers) and graphite share, the decomposition events are more overlapping, forming one -DTG peak, as shown in figure 4.10 (a). The absence of the peak at 792 °C post-centrifugation validates the ability of the centrifugation process to isolate multilayer graphene ($\geq$10 layers) and graphite. The differences observed in the TG analysis before and after centrifugation highlight the impact of centrifugation on the quality of the graphene within the PAN matrix.

After centrifugation, the -DTG curve of the composite shows a notable shift of the fourth peak to a higher temperature, specifically from 603 °C to 623 °C. The removal of multilayer graphene ($\geq$10 layers) and graphite appears to revert the thermal characteristics of the composite closer to that of pure PAN, indicating that the presence of multilayer graphene and graphite disrupts the typical thermal decomposition pathway of PAN by lowering the decomposition temperature.

In figure 4.11, the deconvolution of the third -DTG peak in the 6 wt.% PAN+graphene composite, before (a) and after centrifugation (c) respectively, reveals similar findings. This similarity indicates that the peak is independent of the presence of graphite. The peak observed at around 413 °C in both figures corresponds to graphene, as evidenced by its match with the reference graphene peak at 412 °C. This confirms the presence and impact of graphene on the thermal decomposition of the composite material, as PAN exhibits no peaks within this thermal range. Moreover, in both cases analysed, the deconvoluted decomposition peak at 413 °C consistently accounts for 42 % of the total weight loss during this decomposition event, suggesting that this weight loss peak is exclusively associated with graphene rather than graphite. Below 400 °C, the two peaks correlate with thermal events specific to PAN, highlighting the contributions from both components to the thermal profile of the material observed in the thrid peak.

The deconvolution of the fourth -DTG peak in the 6wt.% PAN+graphene composite, before (b) and after centrifugation (d), is displayed in figure 4.11.

Prior to centrifugation, the presence of a fifth -DTG peak marks a distinct mass loss event linked to the decomposition of graphene, multilayer graphene ($\geq$10 layers) and graphite. The fourth DTG peak is therefore attributed to PAN, supported by the strong fit of its deconvolution

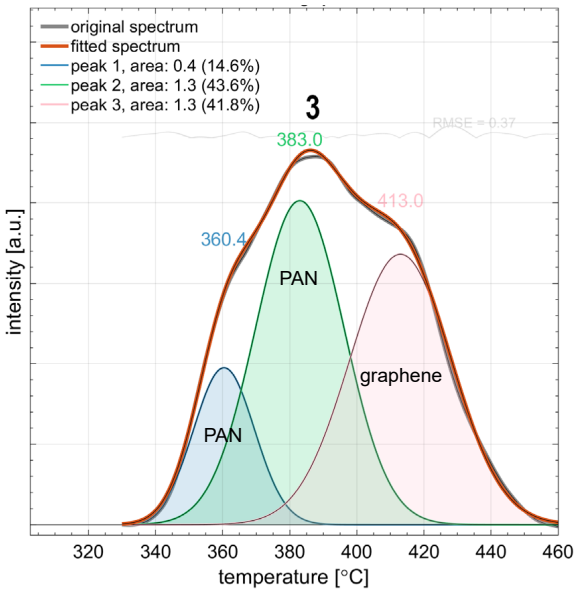

(a) before centrifugation: 340-460 °C range.

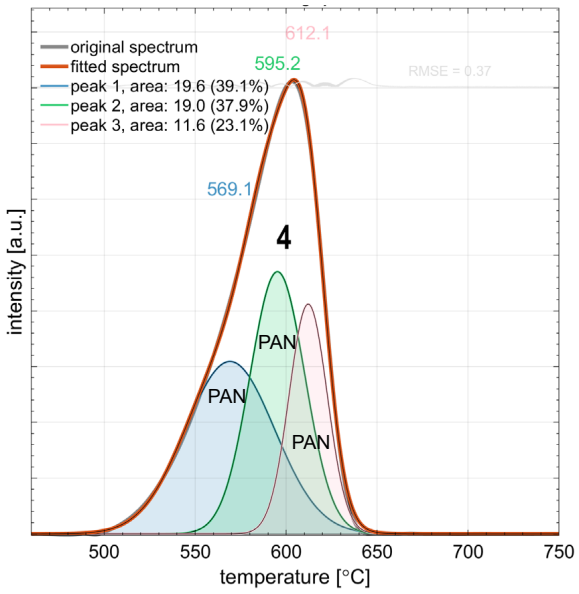

(b) before centrifugation: 500-650 °C range.

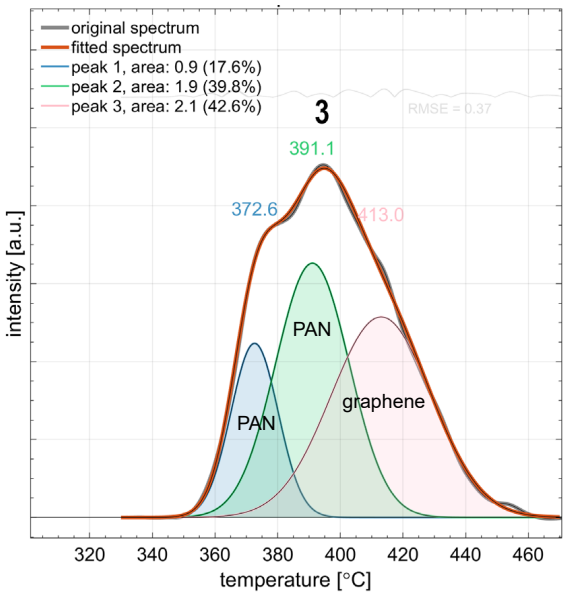

(c) after centrifugation: 340-460 °C range.

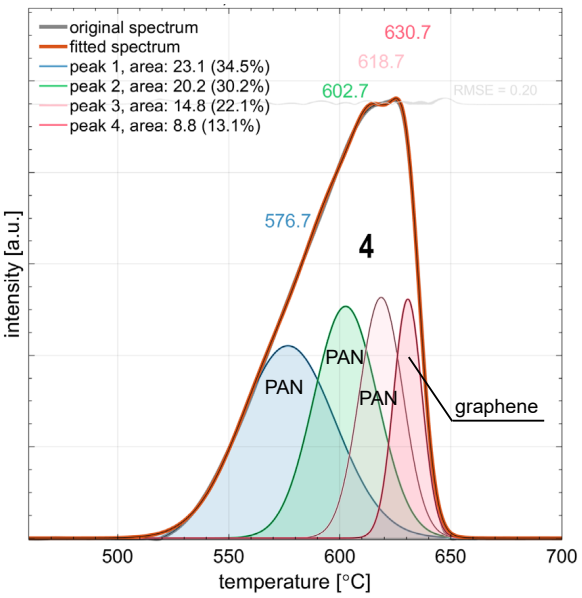

(d) after centrifugation: 500-650 °C range.

Figure 4.11: -DTG peak deconvolution of dried, 6 wt.% PAN+Graphene solution before (top) and after (bottom) centrifugation– (a) and (c): The peak at 413 °C corresponds to graphene, as evidenced by its match with the reference graphene peak at 412 °C (Figure 4.6), indicating its independence from graphite. (b): Decomposition events are attributed to PAN, as graphene- and graphite-related mass loss events are related to the fifth peak. (c): Additional deconvolution peak at 630.7 °C after graphite removal is assosiated with graphene decomposition.

into three peaks, which correspond to to the known decomposition stages and deconvolution profile characteristic of pure PAN, as outlined in section 4.4.2.

After centrifugation, the disappearance of the fifth -DTG peak —resulting from the removal of multilayer graphene ($\geq$10 layers) and graphite— leads to overlapping decomposition behaviour of graphene and PAN, as previously established. Consequently, the fourth DTG peak deconvolutes into four distinct peaks, as evidenced by the strong fit presented in figure 4.11(d). An additional peak at 630.7 °C emerges, representing the contribution of graphene, which accounts for 13.1 % of the total weight loss in this decomposition stage. The PAN deconvolution peak maxima are approximately 10 °C lower in the presence of graphene (see section 4.4.2), as graphene could enhance the heat transfer and disrupt the polymer structure, accelerating thermal degradation. The entire decomposition process accounts for a 69 % loss in weight, of which 9 % is derived from the decomposition of graphene. With the composite weighing 7.42 gr, the graphene content is calculated to be 0.67 gr, exceeding the 0.315 gr graphene expected from a 125 ml solution at a 0.021 gr/ml concentration, as discussed in section 3.4, indicating a discrepancy between the two characterisation methods. Therefore, while TGA can identify components in a material even at very low concentrations, it reaches its limitations in accurately quantifying graphene at these minimal levels. The relatively low amount of graphene compared to PAN may not be sufficient to demonstrate a measurable impact in the TGA. To accurately determine the percentage of each component in the material, complementary and standardised characterisation methods, such as UV-Vis spectroscopy (see section 3.4), should be employed.

Study 2: dried 4 wt.% PAN+graphene solution

For the dried 4wt.% PAN+graphene solution, the analysis involving TGA, -DTG, and -DTG2 curves is presented in figure 4.12a, with the peak deconvolutions for the 340–460 °C and 500–700 °C ranges detailed in figures 4.12b and 4.12c, respectively.

This analysis demonstrates patterns consistent with the 6wt.% PAN+graphene composite, both in the number of peaks and their proportions. Affirming the interpretation in chapter 3 that variations in polymer concentrations have minimal impact on the structural integrity, defect density, and concentration of the produced graphene.

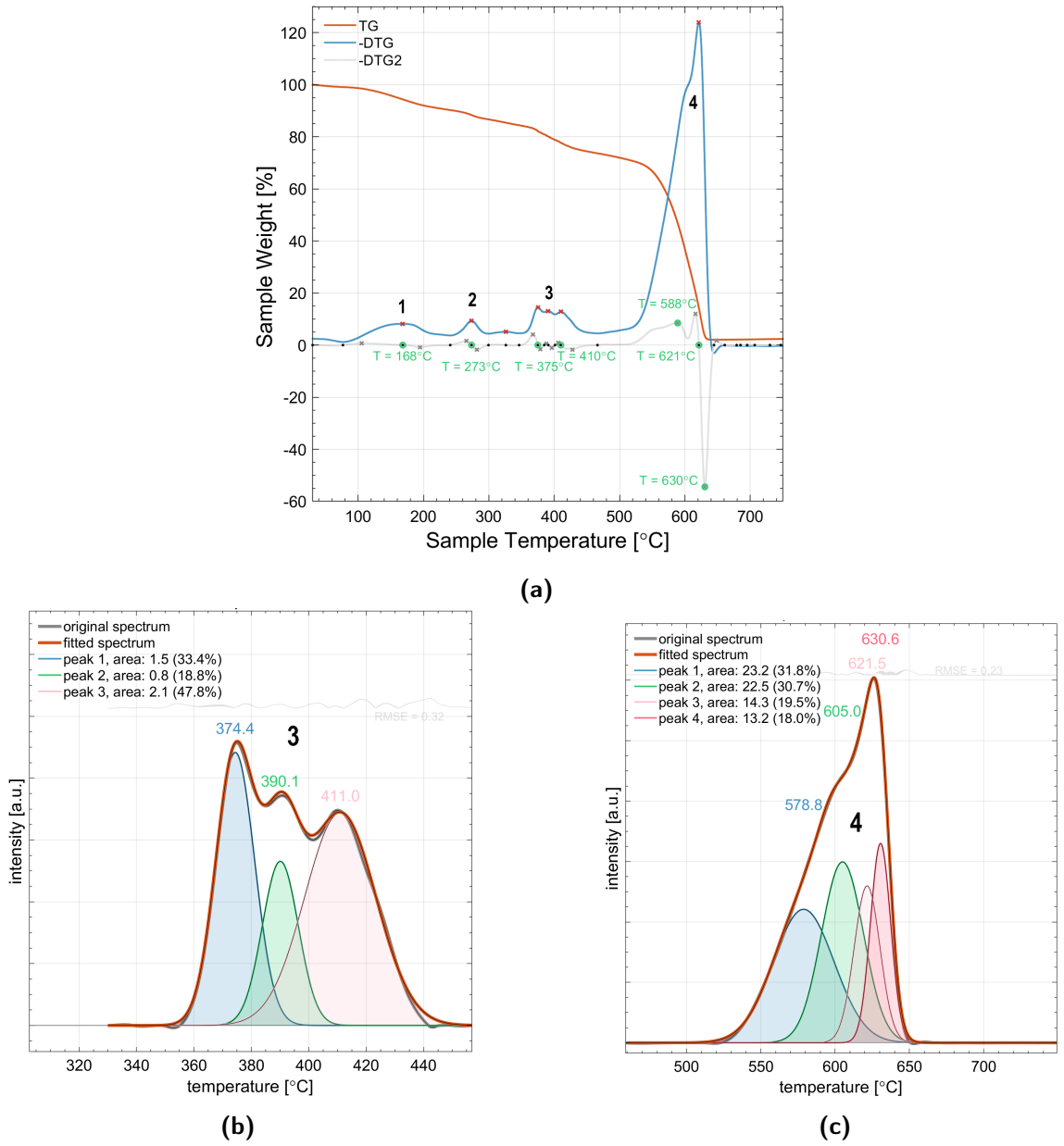

Figure 4.12: Analysis of dried 4wt.% PAN+graphene solution: (a) TGA, -DTG, and -DTG2 curves, (b) Deconvolution for the 340–460 °C peak and (c) 500–700 °C peak. Similar decomposition patterns to shear-mixed graphene in 6 wt.% PAN+DMF solution indicate that varying polymer concentrations minimally impact the structure, defect density, and concentration of graphene.

Study 3: comparative analysis with commercial graphene

TGA of commercially available graphene (Elicarb PR0955, Thomas Swan & Co. Ltd.), depicted in figure 4.13, shows a major decomposition peak at 593 °C (3), characteristic of rGO decomposition patterns, as outlined in section 4.3.2.

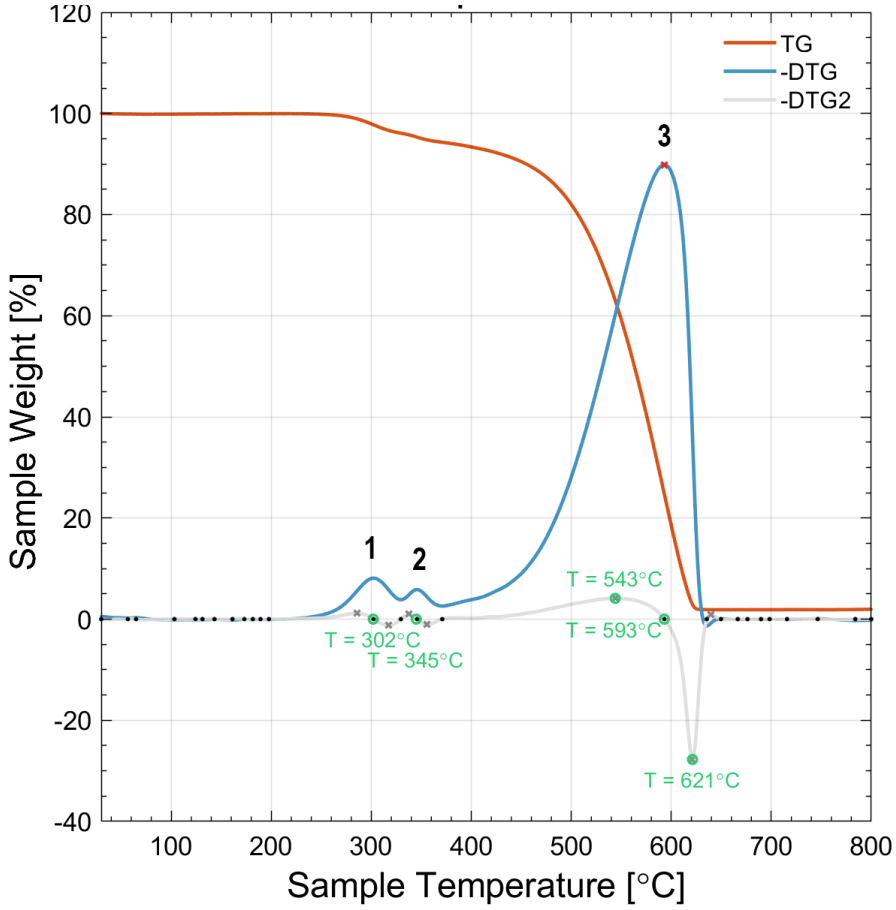

Figure 4.13: Commercial graphene TGA profile. Peaks at 593 °C and 345 °C correspond to rGO decomposition and amorphous carbon, respectively. The thermal decomposition profile does not match that of graphene.

This finding supports the understanding that commercially sourced graphene typically does not classify as graphene. [61]

The analysis also uncovers two additional peaks with maxima at 302 °C (1) and 345 °C (2), which deviate from standard literature data for rGO. Particularly, the peak at 345 °C shows an overlap with the thermal behaviour of amorphous carbon, suggesting that the commercial graphene sample may be a composite of rGO and amorphous carbon.

This finding validates TGA as an effective preliminary diagnostic tool for identifying carbon-based materials based on peak positions, as established in the literature. [72, 75–77] In this context, TGA confirms that the material under investigation cannot be classified as graphene due to a mismatch in thermal decomposition behavior.

However, this example highlights the importance of using established complementary analytical techniques, such as Raman spectroscopy, to accurately assess the material quality and composition. Specifically, peaks 1 and 2 are not characteristic of rGO, which could be attributed to variations in chemical and structural properties, compositions, impurities, or overall material quality. Therefore, to establish TGA as a robust diagnostic tool, a comprehensive understanding of the decomposition behaviors of different commercial graphene materials—produced by over 20 established scalable processes—must be developed.

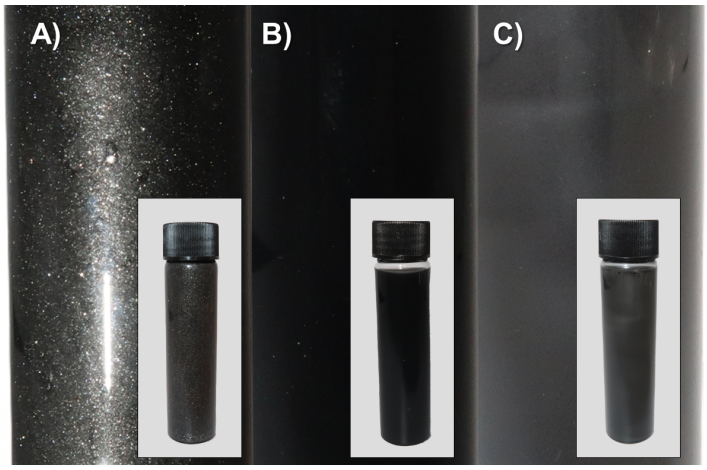

Figure 4.14: Comparative illustrations of dispersions in DMF and PAN – colour is a simple first indicator: (A) Shear-mixed graphite with PAN and DMF solution exhibits a grey, sparkling appearance due to the presence of graphite. (B) Graphene uniformly dispersed in DMF and PAN appears dark black, indicating complete graphite removal. (C) Commercial graphene dispersed in DMF and PAN shows a grey colour with a slight glow, revealing the presence of materials other than graphene.

Despite the complexities in characterisation, the colour of the solutions serves as a simple indicator of material composition, as depicted in figure 4.14. Shear-mixed graphite with PAN and DMF solution (A) exhibits a grey, sparkling appearance due to the presence of graphite. In contrast, a solution of graphene uniformly dispersed in DMF and PAN (B) appears dark black, indicating the complete removal of graphite. Meanwhile, commercial graphene dispersed in DMF and PAN (C) displays a grey colour and a slight glow, which contrasts with the other samples. These optical characteristics suggest the material may not be pure graphene.

4.5 Key advanced TGA findings in graphene characterisation

Finally, the studied data are compared to validate TGA as a reliable method for analysing the properties of graphene-containing PAN composites. An overview graph summarising all mass-loss events documented in this study is presented in figure 4.15. This graph serves as a key reference for understanding the thermal behavior and degradation patterns of the studied materials. In this study, TG analysis provides insightful data on the thermal behavior of PAN and graphene composites.

The initial -DTG peak maxima observed between 102-172 °C are attributed to the evaporation of moisture or solvents, a common feature in TGA studies.
The following peaks are characteristic of PAN (standard PAN) as identified via -DTG analysis, which represents the maximum rate of weight change during mass loss events. The peak at 273-283 °C is indicative of PAN stabilisation. The peaks observed at 360-394 °C are associated with the oxidation process in PAN, while the peaks between 577-645 °C are indicative of the decomposition temperature of the material. These characteristic PAN peaks are utilised alongside the reference graphene sample to determine which peaks correspond to graphene and which to PAN.

Reference graphene produced via shear-mixing shows distinct -DTG peaks at 412 °C and 724 °C. The 412 °C peak, absent in literature-based references (graphene, blue) but consistently observed in samples containing shear-exfoliated graphene, suggests unique attributes introduced by the shear-mixing process. This peak at approximately 412 °C is present in PAN+shear-exfoliated graphene composites (PAN6+graphene, PAN5+graphene, PAN4+graphene) but is absent in pure PAN analysis, making it a reliable indicator of shear-exfoliated graphene. The temperature range of these mass loss events is characteristic of oxidation processes, as PAN oxidation also occurs within this range, and may be attributed to the oxidation of graphene edges and shear-induced defects. The second decomposition peak of reference graphene, originally at 724 °C, shifts to 630 °C when graphene is part of a PAN matrix. This peak is linked to shear-exfoliated graphene, as

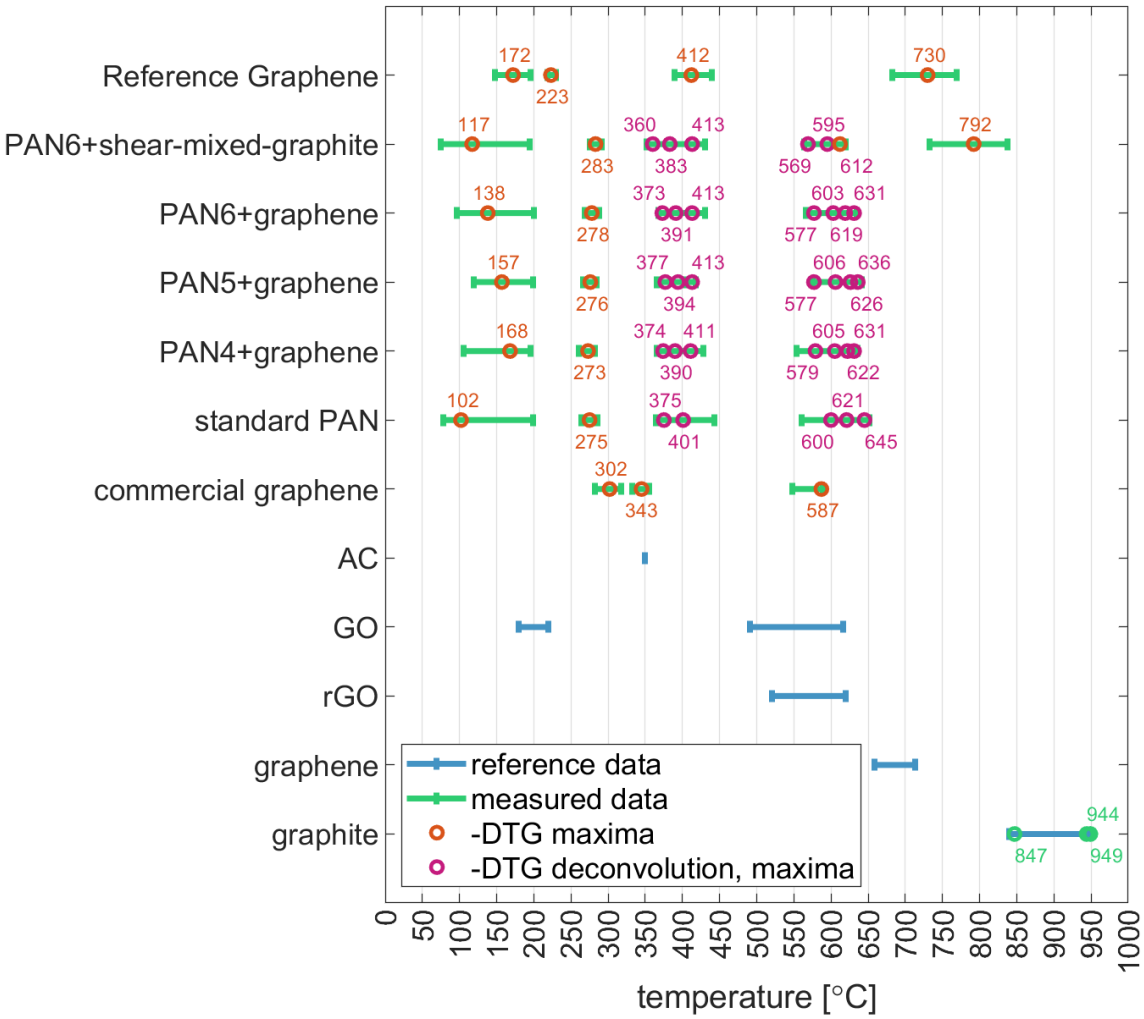

Figure 4.15: TGA-data overview: comparative analysis of mass loss events ranges (highlighted in green) and the peak maxima (indicated by circles) observed across all evaluated TGA samples. The colour coding of the peak maxima circles offers additional insights: - Green circles: peak maxima derived directly from the DTG2 curves. - Magenta circles: peak maxima obtained from the deconvolution of -DTG2 data. (In case, of overlapping mass loss events). - Additionally, the figure includes reference data from existing literature (marked in blue), allowing for direct comparison and contextual understanding of the observed TGA patterns.

the mass loss event deconvolutes into four -DTG peaks, compared to three for pure PAN, with the PAN peaks shifting from 600-645 °C to 577-626 °C. The downshift of all -DTG peaks relative to their respective reference materials suggests an interaction between graphene and PAN, altering the thermal decomposition behavior.
In addition, thermal stability of graphene may decrease when it is incorporated in minor quantities within the composite, contrasting with thermal stability temperature ranges reported in literature and for reference graphene.

A fifth peak at 792 °C in the TGA profile of the PAN composite (PAN6+shear-mixed-graphite) indicates the presence of graphite, as this peak is absent in PAN+graphene composites without graphite. The peak at 413 °C identifies graphene within the composite, demonstrating the ability of TGA to differentiate between graphene and graphite.
TGA can also distinguish between pure graphene and other carbon-based materials, such as rGO, which shows a lower decomposition temperature due to its higher defect density (rGO quality discussed in section 3.2).
Nonetheless, TGA data do not provide details on the number of graphene layers, which would be evident from additional mass loss events and an increased number of -DTG maxima in reference graphene.

5

Synthesis and characterisation of graphene-reinforced electrospun PAN fibres

This chapter details the production process of graphene-reinforced PAN nanofibres, focusing on the electrospinning synthesis method and its optimal conduction parameters. Following this, the chapter presents an assessment of the produced fibres, which addresses their morphology, thermal stability, and key performance attributes.

5.1 Characterisation technique: scanning electron microscopy

Scanning electron microscopy is employed to study the surface characteristics of PAN nanofibres. SEM provides insights into their uniformity, diameter distribution, and surface morphology.
In scanning electron microscopy (SEM), as illustrated in figure 5.1 A), a focussed electron beam is employed to generate highly magnified images of sample surfaces. Electrons from the cathode (electron source) are accelerated towards the anode and then focused into a small-diameter probe via a condenser lens system. The sharper the focus, the higher the beam current, achieved by minimising beam interception through the aperture. The scanning coil within the objective lens changes the focus point position of the beam on the sample, enabling precise imaging. The entire apparatus operates under vacuum conditions to facilitate effective electron movement.

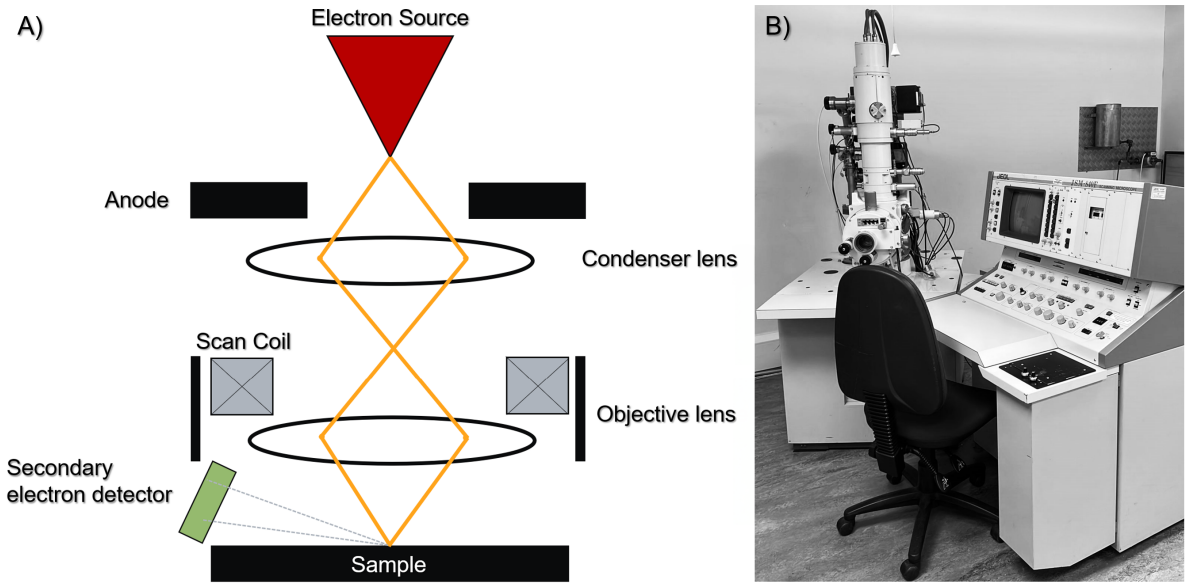

Figure 5.1: A) Diagram showing the operational principle of scanning electron microscopy (SEM), including electron beam focusing and interaction with the sample surface to generate secondary electron signals. B) Used equipment JEOL JSM-840F. Imaging is conducted at 4 kV. Samples are prepared on a carbon adhesive sheet and coated with 8 nm of platinum for enhanced imaging.

As the electron beam interacts with the surface of the sample, it penetrates a few microns deep, producing signals like secondary electrons and backscattered electrons. Here, the secondary electron signals are collected by the detector to form the image. Edges of the sample emit more secondary electrons due to the edge effect, where the geometry of the sample allows more secondary electrons to escape compared to flat regions. This makes the edges appear brighter in the final image due to the higher signal strength at these locations, thereby creating image contrast. [148, 149]

For SEM analysis, the studied samples are prepared on a carbon adhesive sheet and platinum-coated to a thickness of 8 nm, using the JEOL JSM-840F microscope (figure 5.1B) at 4 kV, to produce high-resolution images for further analysis. The selection of an 8 nm platinum coating reflects the maximum thickness that optimises cost and performance for SEM imaging. This conductive layer prevents charging effects, which occur when non-conductive samples accumulate electrons under the electron beam, resulting in image distortion, reduced resolution, and bright artefacts. The coating process utilises sputter deposition, during which argon gas plasma ejects platinum atoms from a source onto a sample, producing a uniform and conductive

layer essential for high-resolution imaging. [150–152]

5.2 Synthesis method: electrospinning

Electrospinning is a method to produce a relatively homogeneous one-dimensional nanofibre network. [4, 153] In general, electrospinning can be used for any soluble polymer with a molecular weight high enough to form an entangled network in solution, ensuring continuous fibre formation. [154]

The typical measurement setup includes a syringe with a polymer solution, a high DC-voltage supply, a spinneret and a grounded collector. Figure 5.2 shows the electrospinning setup used in this project. A high DC-voltage is applied at the tip of the spinneret during the electrospinning process, which charges the located polymer solution droplet. Charged ions accumulate around the polymer droplet. The coulombic repulsion of the ions can overcome the surface tension of the solution, and thus the droplet will elongate into a conical shape and form the Taylor cone, which marks the onset of polymer jet formation for fibre production in electrospinning. Upon reaching a critical voltage, an electrically charged jet of polymer fluid ejects from the tip of the Taylor-cone. [33, 154–156] Fibre formation begins as the solvent rapidly evaporates, and the jet accelerates towards the collector. Initially, the jet stretches uniformly along the electric field, inducing molecular chain alignment. As the jet elongates, electrostatic repulsion among surface charges destabilises its linear path, initiating whipping instabilities and forming loops. The circumference of these loops increases with continued elongation. When the whipping loops reach a critical size, bending instabilities develop, causing irregular deviations in the path of the jet that promote further elongation and thinning. The integrity of the jet is maintained by the combined effects of polymer chain entanglement and surface tension. Entanglement reinforces cohesion to resist breakage, while surface tension counteracts destabilising electrostatic forces, ensuring continuous jet elongation and fibre formation. Additionally, sufficient electrical conductivity facilitates surface charge accumulation, promoting jet elongation, while optimal viscosity ensures polymer chain entanglement, preventing jet breakage and enabling continuous fibre formation. [4, 6, 47, 157, 158]

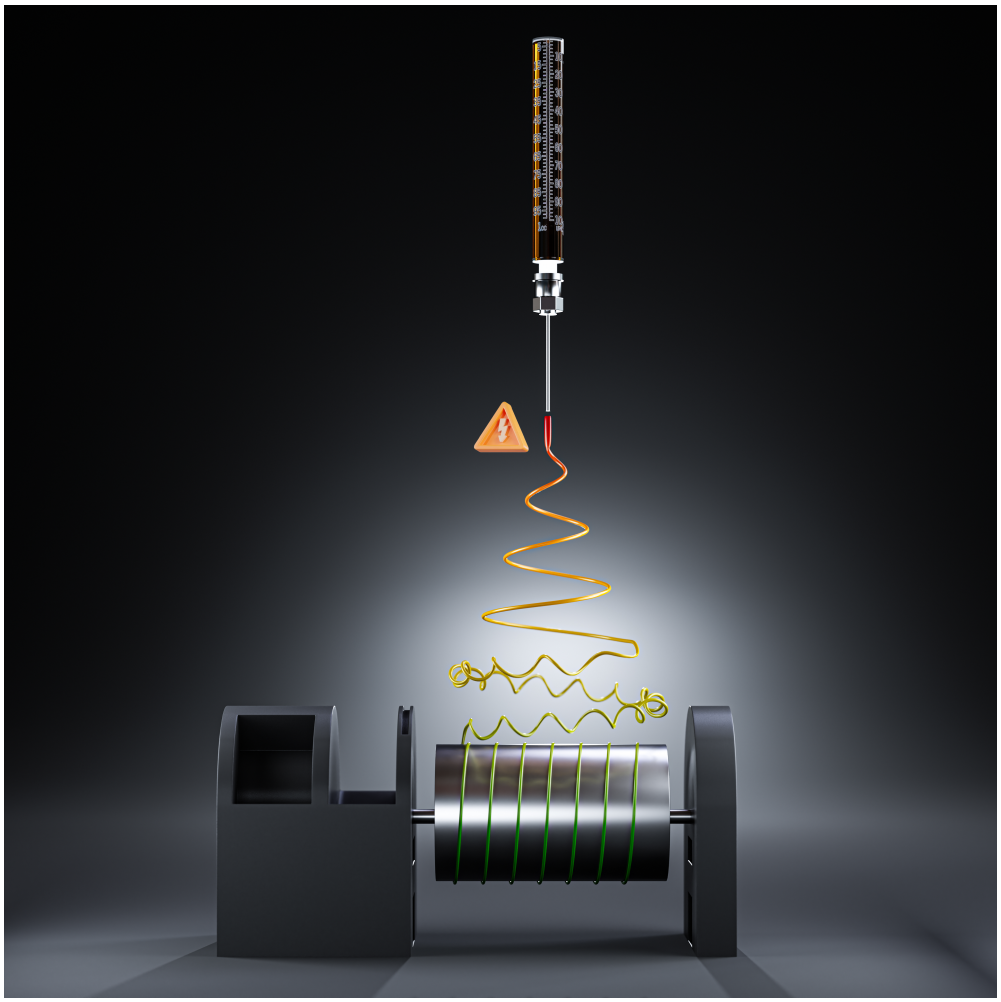

Figure 5.2: Vertical Electrospinning setup with a drum collector and a syringe. The syringe contains in DMF dissolved PAN. High voltage applied at the tip of the spinneret induces a charged polymer jet that forms nanofibres upon rapid solvent evaporation. The rotating drum continuously stretches the fibres, enhancing their alignment and molecular chain orientation. This figure is created using the software *Blender*.

Generally, a grounded metallic substrate is used to collect the fibres. [154, 159] For the vertical electrospinning configuration, gravity is working on the system, which further decreases the diameter of the nanofibre. [158]

With a standard electrospinning setup, nonwoven meshes can be fabricated because of the chaotic jet path. Changing the collector or injection strategy makes it possible to create other nanofibre morphologies, such as aligned, porous, core-shell and hollow nanofibres. [33, 154, 155]

In this project, a drum is used as collector (figure 5.2). The drum rotates at high speed and generates a drawing force that continuously stretches the fibres, improving nanofibre alignment.

This force is controlled by adjusting the collector speed and spinneret-to-collector distance in this study. [15, 160] For example, other common utilised variants are coaxial spinnerets, enabling two solutions to be spun into nanofibres with a core-shell heterostructure. In this way, a hollow morphology can be created by the extraction of the core-solvent. [46, 157, 158, 161]

5.2.1 Key-parameters and their effects

By varying electrospinning conditions and the preparation of the solution, the resulting characteristics of the nanofibres —such as uniformity, diameter, crystallinity, and porosity— can be controlled. [157, 162] Numerous parameters influence these characteristics, all of which are interdependent, as outlined in table 5.1. Hence, an optimal calibration of these parameters is crucial for the successful synthesis of nanofibres, ensuring desired properties are achieved.

Table 5.1: Impact of parameters on electrospinning process ⇒ Solution Parameters; Process Parameters and Environmental parameters

Solution Prameter	
Polymer concentration [163] [27] [156] [15]	• Significantly affects the fibre diameter: higher concentration → bigger, more uniform fibre diameters. • Very high concentration: non-uniform fibre formation /solution not spinnable.
Molecular weight [164] [156] [15]	• Higher weight → higher viscosity → higher required voltage. • Very low molecular weight: jet breakage and droplet formation. • High molecular weight: long polymer chains → increased entanglement → fibre diameter increases.
Viscosity [27] [156] [158] [15]	• Increases by increasing the polymer solution concentration. Also depends on temperature and choice of solvent. • Very low viscosity: droplets appear, fibre diameter decreases. Can result in spraying of droplets (i.e. electro-spraying). • Too high viscosity: solution not spinnable.
Surface tension [27] [156] [158]	• Can be changed through varying the solvent. • Low tension: uniform fibre formation. • Very low tension: jet breakage and droplet formation. • High tension: beaded fibre morphology. • Very high tension: solution not spinnable.

Dielectricity [165]	• High dielectricity: increased molecular polarisation in the polymer solution → amplified local electric field around the jet → stronger force on surface charges → greater jet elongation and whipping instabilities → fibre diameter decreases. • Low dielectricity: beads formation. • Improvement through solvents like Toluene, Acetone or Acetic acid.
Process Prameter	
Applied voltage [163] [27] [156] [158] [15]	• Too low voltage: beads formation/solution not spinnable. • High voltage: fibre diameter decreases (concentration has more influence). • Very high voltage: multiple jet formation/beads formation /solution solidifies and blocks tip.
Nozzle-to--tip distance [166] [27] [167] [156]	• Controls the solidification time of the fibre. • Too low distance: wet fibre mats with embedded droplets because solvent-solidification time too low. • Large distance: decrease electrical field intensity →fibre diameter increases and production rate declines (if voltage constant). • Too large distance: beads formation/solution not spinnable since electrostatic forces too weak. Wider fibre diameter distribution.
Flow rate [165] [156] [158] [15]	• Flow rate controlled by pumping rate. • Too low flow rate: nozzle blocks. • High flow rate: fibre diameter increases, wider fibre diameter distribution, but higher yield (higher voltage required). • Too high flow rate: beads fibre formation.
Rotating speed [166] [27] [4] [15]	• Rotating speed of the collector is relevant if rotating-drum collector is used. • Drawing force between drum and jet is created → fibres are stretched and aligned. • High collecting speed: fibre alignment and stretching enhanced; fibre diameter decreases. • Too high collecting speed: Jet loses contact with the collector → fibre deposition fails.
Environmental Prameter	

Temperature [27] [156] [158]	• High temperature: the evaporation rate of solvent increases → solution viscosity decreases → fibre diameter decreases.
Relative Humidity [166] [27] [165] [168] [158]	• Too low humidity: nozzle blocks because evaporation rate is too high. • High humidity: fibre diameter decreases due to lower evaporation rate [156]/(When water is used as the solvent) fibre diameter increases and formation of nonuniform fibres because of higher water content.

5.3 Development and construction of the experimental setup

To achieve improved alignment of nanofibres, as previously reviewed, the standard electrospinning setup requires modification. In this project, a rotating drum is utilised as the collector. The drum rotates at high speed and continuously stretches the nanofibres. The drawing force causes a better nanofibre alignment. The schematic of this modified setup is depicted in figure 5.2, and the prototype of the drum collector is shown in figure 5.3. This final design has been developed through continuous refinement and testing of the setup throughout this work.

In this experimental setup, a steel cylinder sourced from surplus material in the workshop of Professor Patrick Grant by Gideon Ring determines the dimensions of the drum. The design and configuration of the setup are adapted to fit the specifications of the drum. The drum collector is 22 cm long and 8 cm wide, with an axle 2 cm longer than the drum itself, with a diameter ranging between 12.7 and 12.9 mm. To ensure the stable fixation of the drum, two holder parts are designed using Autodesk Fusion 360 software and then produced through 3D-printing with PLA material. Detailed schematics of these holder parts are presented in figure 5.4.

The primary role of the holder parts is to securely connect the drum to the motor, and to ensure a stable and continuous drum rotation. To enable drum rotation for the required duration of over 10 minutes, crucial for producing sufficiently thick and homogeneous materials, the system is designed to reduce the load on the motor. This reduction is facilitated by minimising friction between the moving drum and its holder, which is achieved through the integration of bearings into

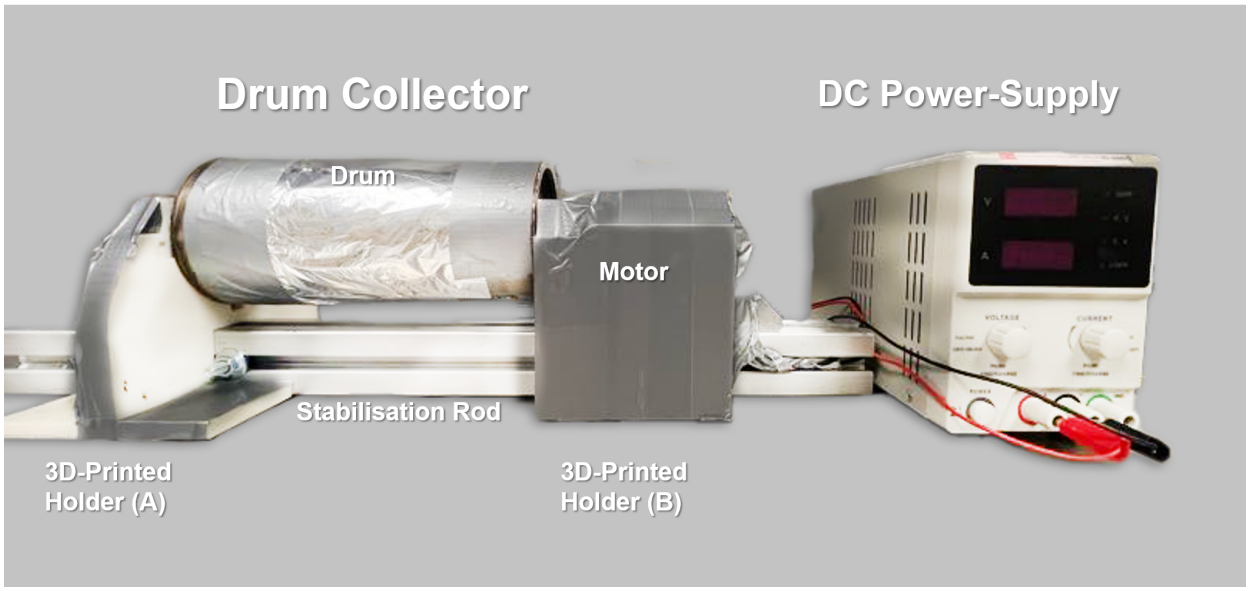

Figure 5.3: Custom-built drum collector (max 8311 RPM) for nanofibre collection - Components: 3D-Printed Holder (A) Drum support, connected to Drum via integrated bearings. 3D-Printed Holder (B) houses Motor, supports Drum, connected to drum via integrated bearings. Motor and Drum joined by metal connector. Stabilisation Rod aligns and secures setup. DC Power Supply regulates Drum speed, adjusting Motor current and voltage; connected via positive/negative terminals.

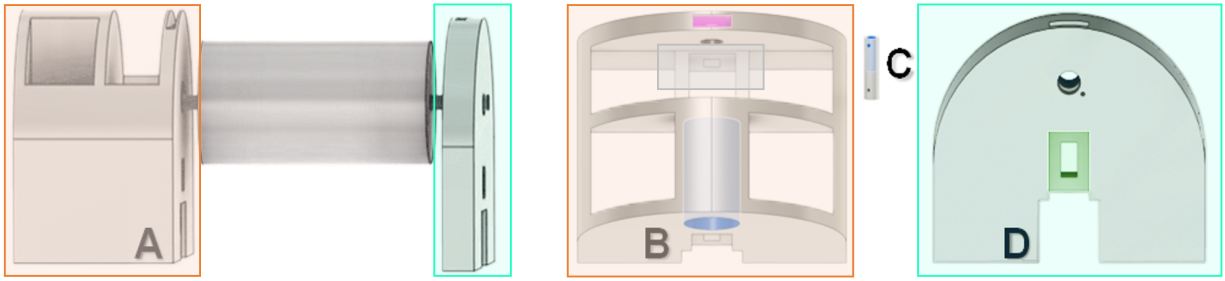

Figure 5.4: Holder parts schematics - (A) Overall design of drum collector with left holder (orange) and right holder (cyan); (B, D) Holder parts from different perspectives. (B) Features motor location (blue) and bearing insertion slot (pink), with brass connector (C) Coupling motor and drum (grey area in (B)). (D) Displays stabilisation feature for aluminum profile, connected using mounting brackets as link component (fixation feature also present in (B)); bearing slot (pink) is also part of (D).

the system (figure 5.5, right). Morevoer, the drum and motor are linked using a brass connector part, manufactured by Peter Flaxman in the Oxford Materials Science workshop (figure 5.4, C). To electrically ground the drum, the ground cable is attached to the outer ring of one of the bearings. This practice is effective because the bearing is electrically conductive, connected to the drum, and its outer bearing part is stationary. Other conductive parts of the collector rotate, hence, are unsuitable for grounding.



Figure 5.5: Motor: powers drum rotation - 5844 RPM at 6 V, 1.7 A; 8379 RPM at 8.6 V, 1.7 A; 3373 RPM at 3.6 V, 1.1 A, providing consistent and efficient motion for fibre collection. Bearings: mounted on drum axis facilitate smooth, low-friction rotation, maintaining stable drum operation for fibre collection.

For aligning the nanofibres, a motor with a sufficient high rotation speed is fundamental. The 321-3192 12vD.C. motor with a maximum speed of 8380 RPM is selected, as depicted in figure 5.5, left. This motor is powered by a 12 V/DC power supply.

5.4 Parametric study and optimisation on PAN fibres

A comprehensive parametric study of PAN-based nanofibres is presented in this section. The primary objective of this study is to determine the optimal electrospinning conditions for this experimental setup.

5.4.1 Electrospinning parameter analysis at zero speed: the standard collector

In the initial phase of this parametric study, the focus is on the simplest configuration: electrospinning nanofibres from PAN dissolved in DMF.

Here, a standard collector without rotation (RPM=0) is employed to understand the basic electrospinning dynamics. Therefore, this configuration is the starting point for determining optimal electrospinning parameters without the influence of additional composite materials. The studied electrospinning parameters are weight percentage concentration of solution [wt.%], humidity [hu in %], needle size [gauge, ga], collector-to-nozzle distance [cm] and rotating speed of the drum [RPM]. In this parametric study, a range of PAN concentrations dissolved in DMF is investigated: 8 wt.%, 9.5 wt.%, 10 wt.%, 11.5 wt.%, 12 wt.%, 13 wt.%, 14 wt.%. For each of these concentrations, tests are conducted under four humidity levels (15 %, 16 %, 20 % and 30%), utilising four needle gauge sizes (17 ga, 18 ga, 19 ga and 20 ga), and two collector-to-nozzle distances (15 cm and 20 cm). The higher concentrations, particularly 12 wt.%, 13 wt.% and 14 wt.%, exhibit a viscosity too high for successful electrospinning, causing nozzle blockage and preventing jet formation and elongation. [27, 156, 158] In contrast, at 8 wt.%, the viscosity is too low, resulting in the formation of not uniform fibres and beads, as demonstrated in figure 5.6.

Within the parametric electrospinning study, the 8 wt.% concentration, which has the lowest viscosity, also exhibits the smallest fibre diameter of 118 nm$\pm$68 nm. When the concentration is increased to between 9.5 wt.% to 11.5 wt.%, the fibre diameter ranges from 200 nm to 500 nm (figure 5.7 E). It is also noted that electrospinning is not possible at humditiy levels greater than 32 %, as water molecules in the air accumulate on the jet surface, reducing surface charge density. This diminishes the electrostatic forces which are necessary for jet ejection and elongation, thus preventing fibre formation. [169]

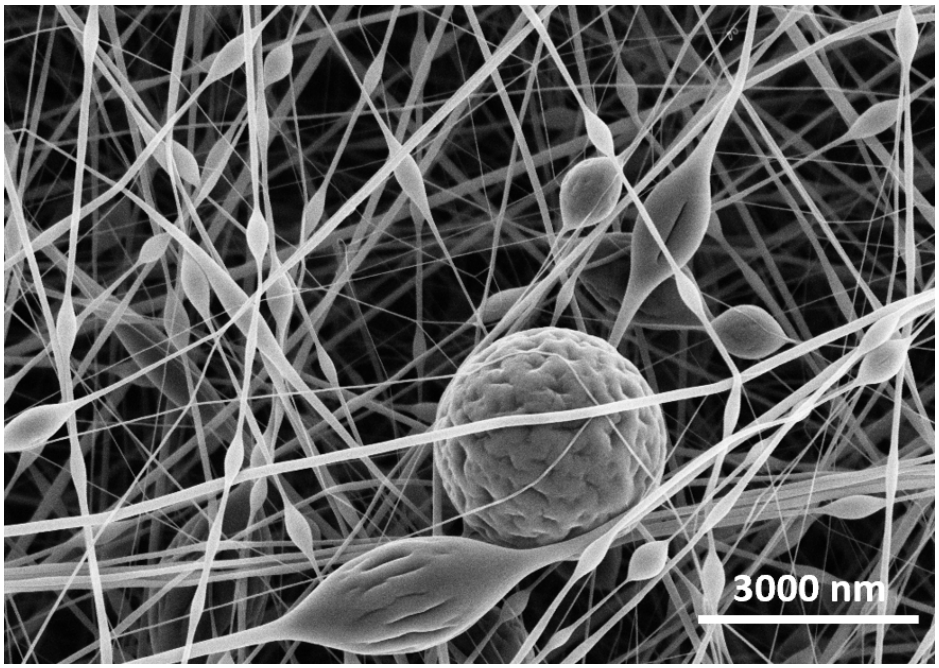

Figure 5.6: Secondary electron image of PAN nanofibres. Fabricated with parameters: 8wt.%PAN, 20 ga, 20 cm, 15% hu, 21.5 kV, 0 ml/h; Diameter: 118 nm$\pm$68 nm. Low viscosity leads to non-uniform fibres and bead formation. Fibre diameters are measured using ImageJ software, with 150 individual fibres analysed to ensure statistically reliable results. The average diameter and standard deviation are calculated using Matlab to characterise the overall distribution and variability of the fibres. (Figure 5.8 highlights fibres produced under optimal conditions, displaying defect-free fibres with homogeneous diameters.)

Building on the previous discussion of electrospinning parameters, figure 5.7 presents the relationship between various parameters, including collector-to-nozzle distance, humidity, gauge size, polymer concentration, nanofibre diameter, and applied voltage. Figure 5.7 A) indicates that fibre diameter is not significantly affected by the nozzle-to-collector distance. The analysis of fibre diameter as a function of this distance reveals a random distribution, suggesting that fibre size is predominantly influenced by factors other than distance. In contrast, higher voltages tend to reduce fibre diameter because the electric forces on the fibre become greater (figure 5.7 E). Figures 5.7 B) further demonstrate that higher humidity levels cause fibre diameters to increase, as fibres absorb more water during the electrospinning process, thereby leading to a reduction in required voltage due to lower solution viscosity. Therefore, humidities $\geq$30 % are excluded from further investigations to identify the optimal synthesis conditions. Figure 5.7 C) suggests that the resulting fibre diameters are similar for PAN polymer concentrations

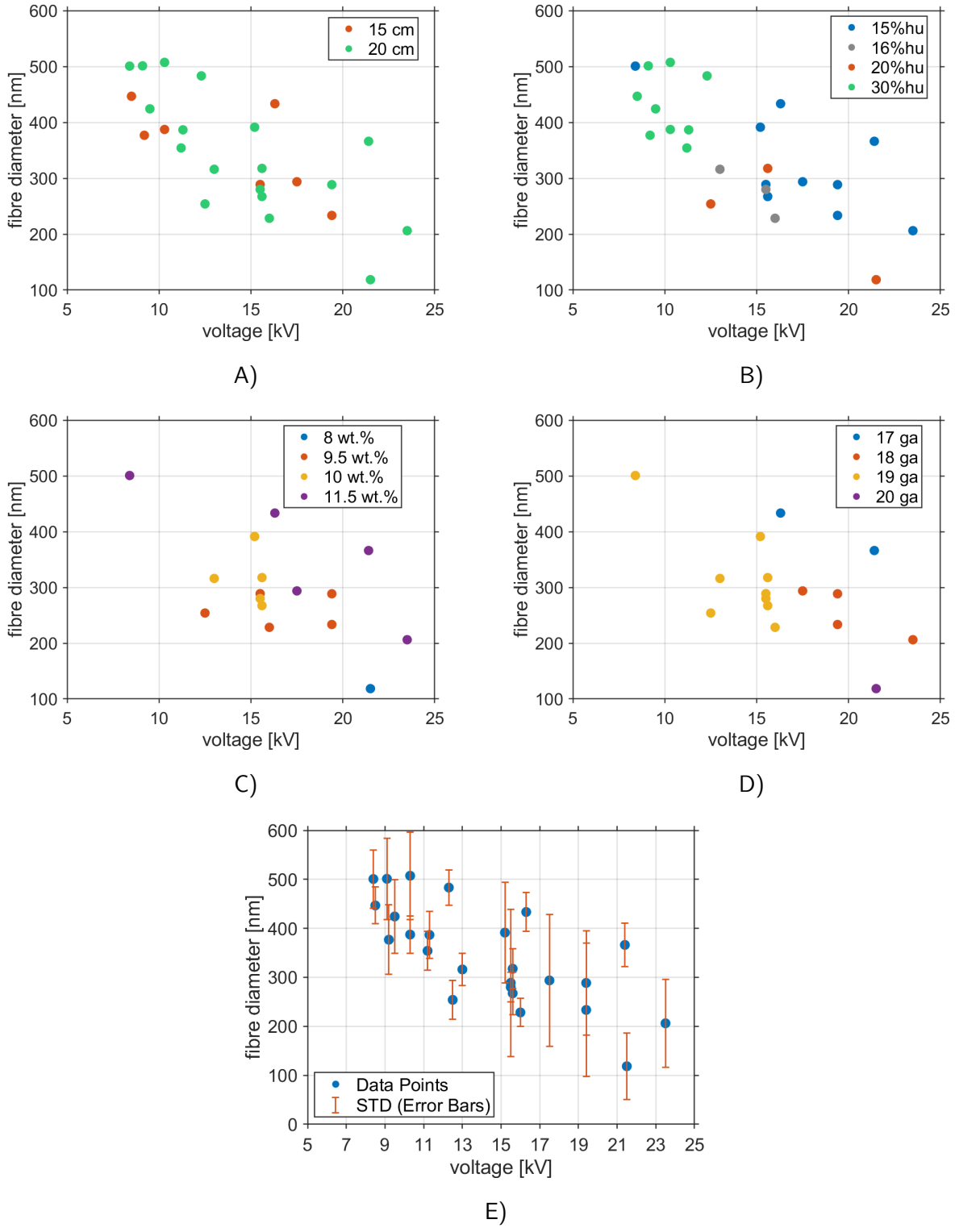

Figure 5.7: Electrospinning parameter correlations: A) Diameter - voltage - collector-to-nozzle distance, B) Diameter - voltage - humidity, C) Diameter - concentration - distance, D) Diameter - concentration - gauge size, F) Diameter - Voltage. *Optimal electrospinning parameters identified:* 9.5-10 wt.%PAN concentration, 15-20 % humidity, 15-20 cm distance, 18-19 ga needle size.

between 9.5-10 wt.%, indicating a stable electrospinning process within this concentration range. Figure 5.7 C) also shows that higher polymer concentrations tend to correlate with larger fibre diameters. Whereas gauge size, as indicated in figure 5.7 D), has a relatively minor influence on fibre diameter within the operational polymer concentration range for electrospinning, with 18 ga and 19 ga being the most ideal for uniform and consistent fibre production.

In conclusion, the optimal parameters for electrospinning in this study are determined to be 9.5-10 wt.% polymer concentration, 15-20 % humidity, 15-20 cm collector-to-nozzle distance, and 18-19 ga needle size. As shown in figure 5.7 E), the smallest fibre diameter, 280 nm, which exhibits the lowest standard deviation of $\pm$31 nm, is achieved under synthesis conditions of 10 wt.%PAN, 19 ga, 20 cm, 15% hu and 15.5 kV. Under these synthesis parameters, as presented in figure 5.8, the PAN nanofibres produced are uniform, non-porous, and bead-free.

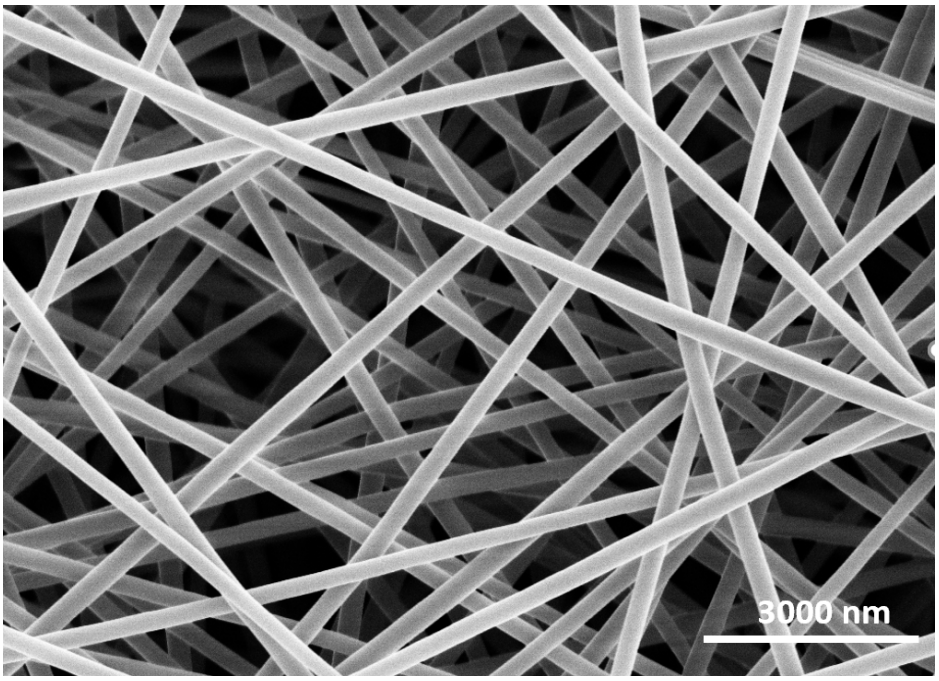

Figure 5.8: Secondary electron image of PAN nanofibres. Fabricated with optimal electrospinning parameters: 10 wt.%PAN, 19 ga, 20 cm, 15% hu, 15.5 kV, 0 ml/h. The resulting fibres exhibit a uniform diameter of 280 nm $\pm$31 nm, and are non-porous and bead-free. Fibre diameters are measured using ImageJ from 150 fibres. Average diameter and standard deviation are calculated in Matlab to assess fibre distribution and variability.

5.4.2 Enhancing fibre alignment with increased drum collector speed

This section examines the optimal rotation speed required to achieve fibre alignment in electrospinning. According to existing literature, speeds below 1500 RPM are commonly used ([170–172]). The custom-built laboratory setup, however, can reach speeds up to 8379 RPM. Thus, to assess the impact of different speeds on fibre alignment, PAN nanofibres are electrospun at 0 RPM, 4000 RPM, and 8000 RPM, each for a duration of 10 minutes. SEM images of these experiments, presented in figure 5.9, facilitate the evaluation of the degree of fibre alignment. At 4000 RPM, nanofibres begin to straighten but only achieve partial alignment. In contrast, at 8000 RPM, a clear alignment of nanofibres is achieved, establishing it as the speed for the drum-collector fibre production process.

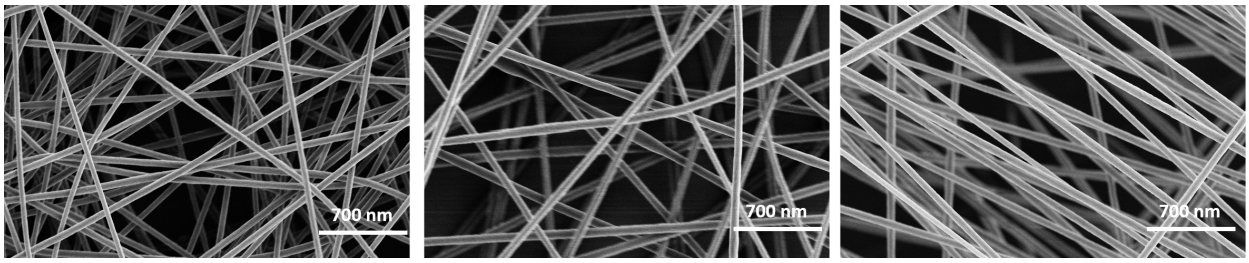

Figure 5.9: Pan nanofibres spun with 0 RPM (left), 4000 RPM (middle), 8000 RPM (right): Fabricated with parameters: 18 ga, 10 wt.%PAN, 20 cm, 30% hu. The images highlight the progression of fibre alignment, peaking at 8000 RPM.

Upon evaluating the role of the drum collector in the electrospinning synthesis process, as presented in table 5.2, a reduction in fibre diameter is observed, with reductions increasing significantly under higher humidity conditions—from 14 % to 25 %.

Table 5.2: Comparison of fibre diameters for aligned and non-aligned fibres – investigation of drum collector impact on diameter reduction (improvement shown as %), with greater reductions observed at higher humidity levels.

Condition	Fibre Diameter [nm]		Improvement
	not aligned [0 RPM]	aligned [8000 RPM]	
10 wt.%PAN, 15% hu, 18 ga, 13 cm	315±55	276±56	14 %
10 wt.%PAN, 30% hu, 19 ga, 18 cm	645±157	466±128	25 %

The enhanced reduction is attributed to slower solvent evaporation and water absorption at higher humidity, resulting in increased residual solvent and greater polymer chain mobility. [169]

Higher polymer chain mobility allows the fibre to elongate further under the mechanical drawing forces of the rotating drum collector, continuing to stretch along the surface of the drum before solidification. In addition to the reduction in fibre diameter, a key advantage of using the drum collector is the enhanced alignment of the fibre bundle, which contributes to the mechanical performance and potential applications of the fibres. [173]

5.5 Evaluation of electrospun PAN nanofibres

The study focuses on the production of graphene-reinforced PAN nanofibres via electrospinning, utilising a shear-mixed solution as the starting material. A 6 wt.% PAN concentration is chosen for this process, as it is the maximum concentration that still allows for effective shear-mixing and centrifugation processability. Higher concentrations present challenges, either in separating graphite from the solution during centrifugation or in solution solidification during shear mixing, which could be attributed to increased viscosity and consequent heat generation (see chapter 2 and section 3.2). The resulting 6 wt.% PAN+graphene solution, however, exhibits a viscosity too low for electrospinning. To overcome this, the viscosity is adjusted by blending the solution in a 1:1 ratio with a 14 wt.% PAN+DMF solution, achieving a final PAN concentration of 10 wt.%. This adjustment is made considering that the addition of graphene does not significantly alter the viscosity, as shown in figure 5.10, confirming the alignment of the solution with the optimal electrospinning conditions. Parametric studies indicate that a concentration range of 9.5-10 wt.% PAN is most suitable for electrospinning, as detailed in section 5.4.1. For example, mixing shear-exfoliated graphene at 3 wt.% with 14 wt.% PAN in a 1:1 ratio results in a final concentration of 8.5 wt.%, which falls outside the optimal electrospinning range and results in poor fibre quality, characterised by inconsistent diameter and surface irregularities.

In general, a 14 wt.% PAN solution in DMF is selected for 1:1 blending as it balances high polymer content with manageable dissolution times ($\sim$6 hours). Higher concentrations lead to slower dissolution and increased powder agglomeration, negatively affecting solution homogeneity. As a result of this optimised process, a graphene-reinforced PAN nanofibre mat, which is white in colour, is successfully produced and shown in figure 5.11.

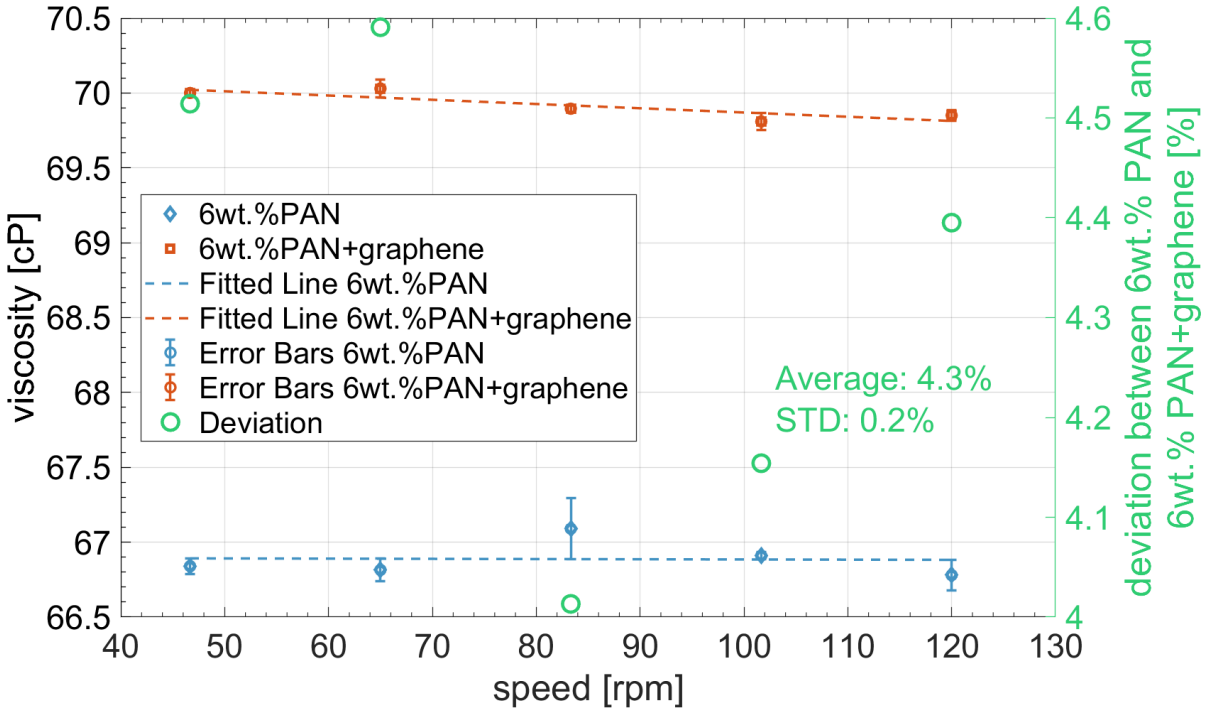

Figure 5.10: Viscosity comparison of 6 wt.% PAN and 6 wt.% PAN+graphene solutions. The two dotted lines show a linear fit of the viscosity measurements, with error bars representing standard deviation per data point. The green data points show the percentage deviation in viscosity between the two solutions. The addition of graphene results in a viscosity change of only 4.3 % (std 0.2 %), indicating minimal impact. Measurements are performed using a DV2T Viscometer (AMETEK Brookfield), with shear speeds ranging from 45 to 120 RPM, with special thanks to Shiling Dong for conducting the experiments. The results are based on three measurements.

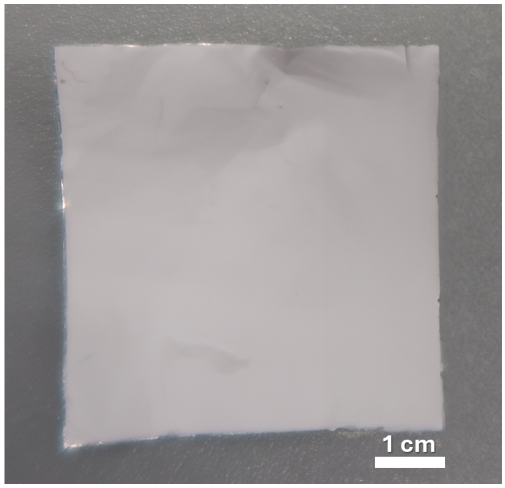

Figure 5.11: Successfully synthesised graphene-reinforced PAN nanofibre mat, characterised by a white and uniform structure.

To assess the impact of the fibre form of PAN material on thermal stability and decomposition patterns, TGA is performed on the electrospun fibre assembly, as shown in figure 5.12.

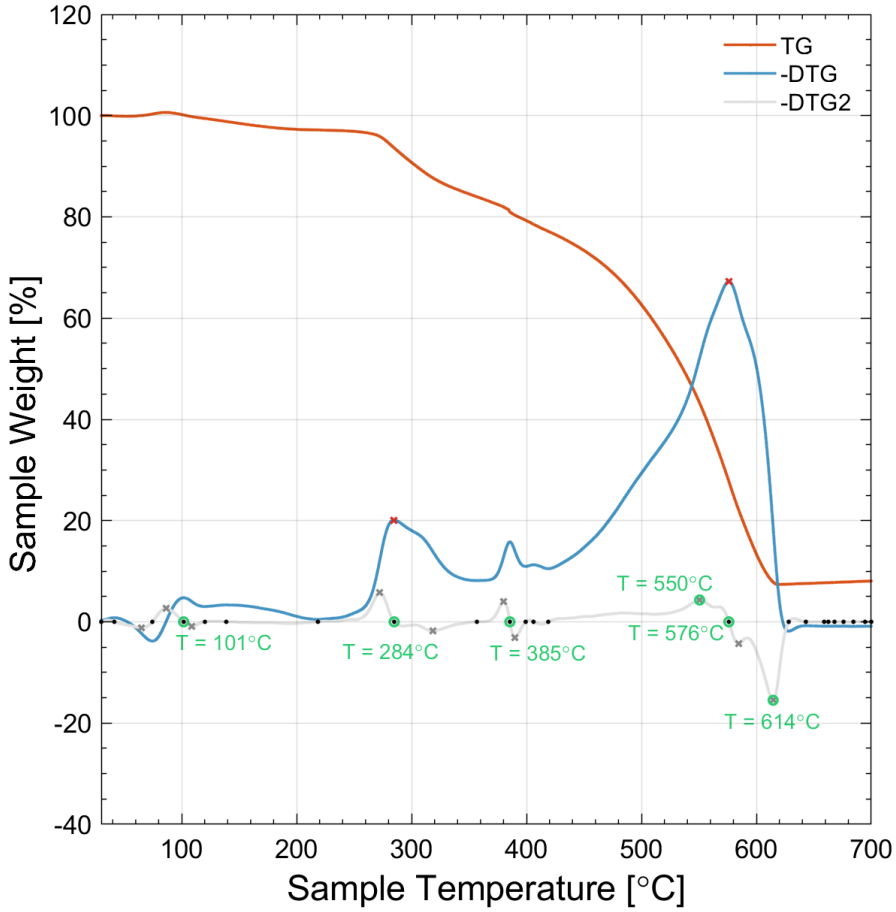

Figure 5.12: TGA: electrospun PAN nanofibre assembly. Enhanced thermal stability in the nanofibres is attributed to polymer chain alignment and orientation during electrospinning, compared to the pure dried PAN solution (see section 4.4.2). The main decomposition event is broader and occurs at a lower temperature, reflecting the diverse fibre diameters.

The TGA results of the electrospun material are compared with those obtained from the same base solution in its dried form (pure dried PAN solution; see section 4.4.2). The analysis reveals four distinct weight loss events. The initial weight loss, occurring at 101 °C, corresponds to moisture removal from the material, a process that also occurs in the dried PAN solution within the same temperature range. The second weight loss peak for the electrospun PAN nanofibres is observed at 284 °C, 10 degrees above the peak in the dried solution. This increased thermal

resistance could be attributed to the alignment, orientation, and stretching of polymer chains during electrospinning, which enhances molecular order, minimises chain entanglements, and reduces voids and free volume, thereby raising the energy required for thermal decomposition. At this temperature, the stabilisation process is initiated, characterised by the formation of ladder structures-like PAN-molecules, accounting for an approximate mass loss of 10 %. Predominantly, dehydrogenation and cyclisation processes occur within this temperature range, contributing to the enhanced thermal stability of the material. In the TG analysis of the PAN material, both the electrospun and dried version exhibit their third peak in a similar temperature range, at approximately 385 $^{\circ}C$ and 384 °C, respectively. The electrospun PAN nanofibres, however, display a significantly narrower peak, potentially indicating a different oxidation behavior compared to the dried PAN solution. This phenomenon may be attributed to the increased surface area of the fibre, which enhances oxygen interaction and accelerates the oxidation process. The fourth peak, broader for the electrospun PAN nanofibres, represents the main decomposition event, where the material undergoes a substantial weight loss of around 70 %. This broadening can be attributed to morphological variations introduced by electrospinning, resulting in diverse fibre diameters. Consequently, this leads to a wider decomposition temperature range within the material. The decomposition process in the electrospun PAN nanofibre material concludes at 614 °C, which is lower compared to the decomposition temperature of the dried PAN solution. This difference could be attributed to the higher volume and lower density of the electrospun material, in contrast to the denser film form of the dried PAN solution. Both variants exhibit a characteristic left inflection of the fourth peak, indicative of pure material without overlapping components.

5.5.1 Fibre diameter distribution and morphological uniformity of PAN nanofibres: the role of graphene

This section presents a comparative analysis of fibre diameters in PAN nanofibres, with and without graphene reinforcement. The fibres are characterised by uniform, bead-free morphology, with consistent coverage over the majority of the sample surface. This high quality contrasts with suboptimal fibre formation, which is marked by bead formation, irregular diameters, and non-uniform deposition, as illustrated in figures 5.6 and 1.6.

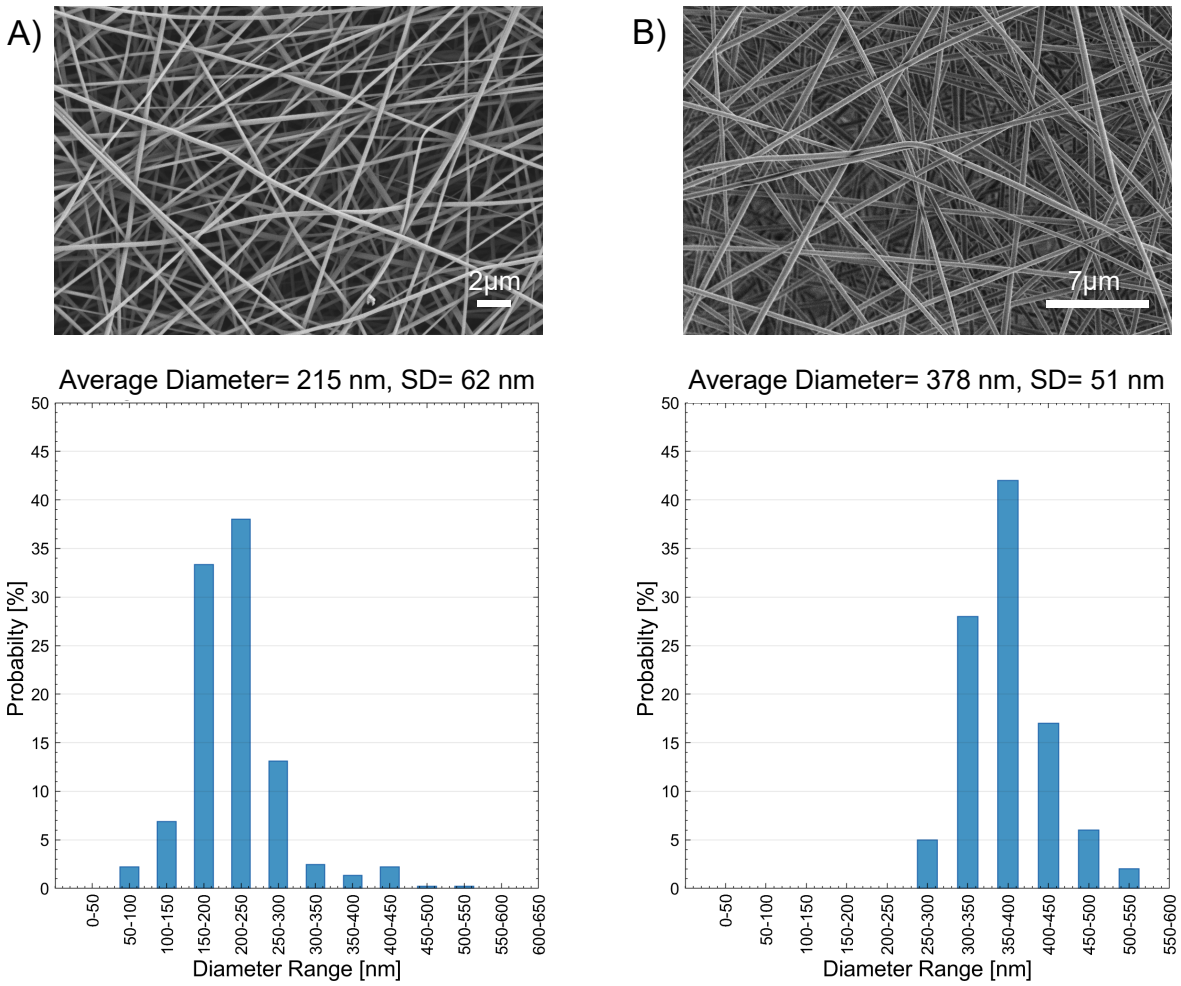

Figure 5.13: SEM characterisation of PAN nanofibres: diameter distribution and morphology comparison between A) Non-graphene-reinforced and B) Graphene-reinforced nanofibres, both collected using a standard collector. PAN nanofibres without graphene exhibit a smaller average diameter (215 nm, SD 62 nm) compared to those with graphene (376 nm, SD 51 nm). The graphene-reinforced nanofibres show a narrower distribution range, with 43 % falling between 350-400 nm, indicating more uniform fibre formation. Fabrication parameters are detailed in table 5.3

Figure 5.13 shows that PAN nanofibres without graphene reinforcement, when collected on a standard collector, exhibit a notably narrower diameter. However, their diameter distribution is wide, ranging from 50 to 450 nm, with approximately 40 % of the fibres falling within the 200-250 nm range. In contrast, the addition of graphene to the fibres results in a narrower diameter distribution, ranging from 250 to 550 nm, with over 40 % of the fibres concentrated in the 350-400 nm range. This is also reflected in the lower standard deviation for fibre diameters, with 51 nm for graphene-reinforced fibres compared to 62 nm for fibres without graphene. The

presence of graphene may promote molecular chain alignment, reducing entanglements and enhancing fibre uniformity. The increase in diameter for graphene-reinforced fibres is attributed to the enhanced electrical conductivity of the solution, which facilitates faster fibre collection and, thus, a lower solvent evaporation rate.

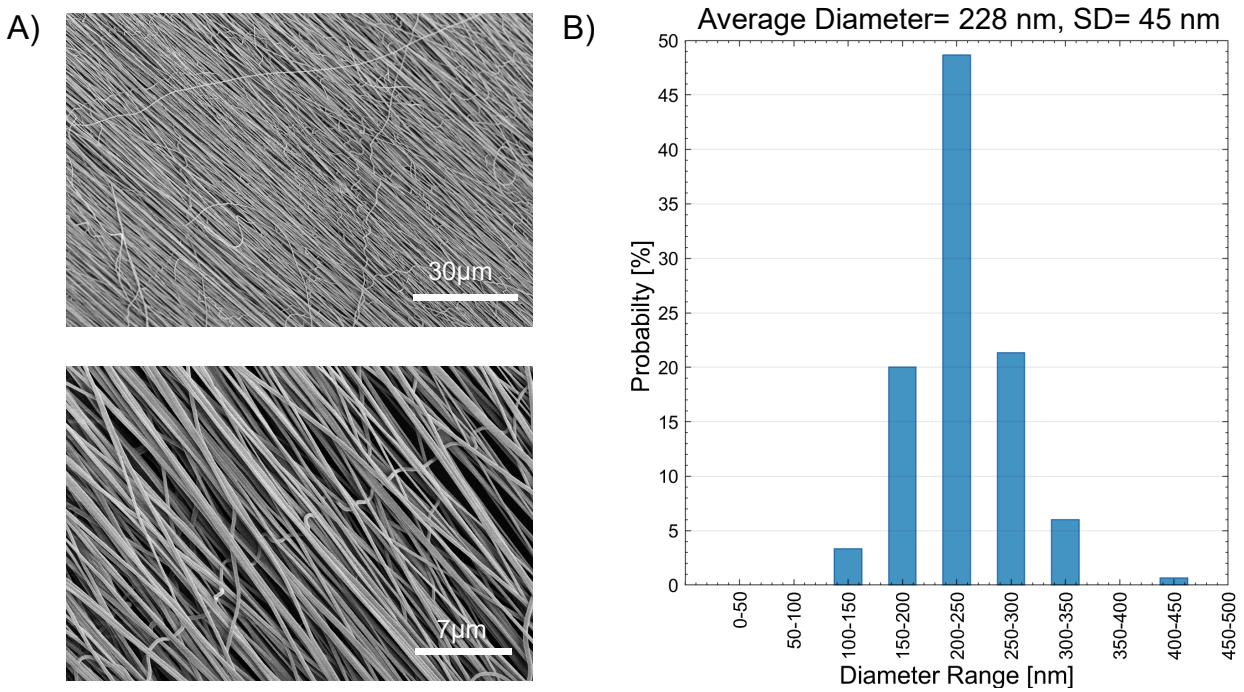

Figure 5.14: SEM characterisation showing: A) Morphology and B) Diameter distribution of graphene-reinforced PAN nanofibres collected using the drum collector. Over 50 % of the fibres exhibit diameters between 200-250 nm, indicating high uniformity. The average diameter measures 228 nm with a standard deviation of 45 nm. Fabrication parameters are provided in table 5.3.

Assessing the average diameter of graphene-reinforced PAN fibres collected using the drum collector (see figure 5.14), a diameter reduction of approximately 40 % is observed compared to those produced with the standard collector. Furthermore, the standard deviation in the fibre diameter decreases even further, with more than half of the fibres exhibiting diameters between 200-250 nm. These findings highlight the significant impact of the drum collector in enhancing the uniformity and reducing the diameter of the nanofibres, attributed to the mechanical stretching forces exerted by the drum during the electrospinning process.

The stretching forces exerted by the drum collector emphasise the critical role of molecular chain alignment and nanoscale confinement in determining fibre morphology and uniformity.

Table 5.3: Comparison of fibre diameters between fibres with and without graphene, alongside an analysis of the effect of the drum collector (∼8000 RPM, corresponding to a linear velocity of ∼67 m/s) on graphene-reinforced fibres. The comparison is valid as all fibres are fabricated under the same conditions, using the following parameters: 10 wt.% PAN, 19 ga, 15 cm, 15% hu - 15 cm chosen because this is maximum distance for drum-collector, for better comparability + distance not a strong influence factor for fibres (see section 5.4.1). The standard collector produces the smallest diameters. Graphene-reinforced fibres show a >40 % diameter reduction when drum collected. The standard collector may exhibit higher graphene concentration due to a 1:2 mixture ratio rather than 1:1. If the ratio were adjusted to 1:1, the trends would persist, though the diameter reduction between drum and non-drum collected fibres might be less pronounced.

Condition	**Average** [nm]	**SD** [nm]
Standard Collector: **10 wt.% PAN** (19 ga, 15 hu, 15 cm)	215	62
Standard Collector: 1/3 18wt.% PAN: 2/3 6wt.% PAN+graphene – total **10 wt.% PAN** (19 ga, 15 hu, 15 cm)	376	51
Drum: 14% PAN: 6% PAN+graphene, 1:1 - total **10 wt.% PAN** (19 ga, 15 hu, 15 cm)	228	45

The coil size of a PAN molecule with a molar mass of 150,000 is estimated to be between 30–40 nm in solution. [36] During fibre formation, the polymer chains are expected to contract significantly from their solution state, forming a more compact structure in the solid state. With an average fibre diameter of 228 nm for the graphene-reinforced PAN fibre, this implies the alignment of multiple molecular chains in parallel, likely exceeding six, depending on the degree of contraction during solidification. A rough estimate, based on a graphene concentration of 0.21 mg/ml (see section 3.4) and 90 mg/ml PAN, suggests a graphene content of approximately 2.3%, corresponding to about 6 nm of graphene per nanometre of fibre diameter – calculated as 2.3 % of the 228 nm fibre diameter. This indicates that each diameter unit likely incorporates a layer of graphene [55], inducing a confinement effect that could have a considerable impact on the mechanical properties of the PAN nanofibres.

However, the positive effect of graphene reinforcement on PAN nanofibres is demonstrated by the increased stretchability of the fibres. Graphene-reinforced fibres extend up to three times more than non-reinforced fibres. The initial assessment of the stretching ability of aligned graphene-reinforced PAN mats is conducted using the prototype material stretching system shown in figure 5.15. The system applies a constant force through a gripping mechanism designed to evenly distribute

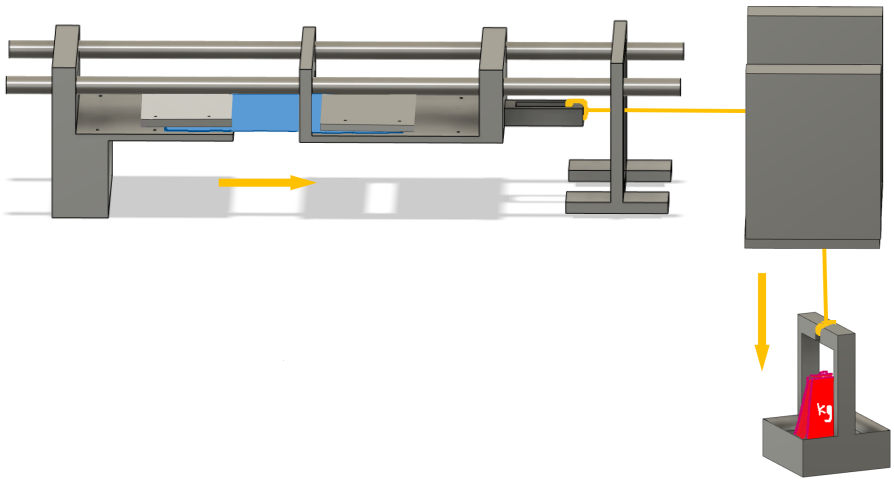

Figure 5.15: Prototype schematic for fibre mat stretching, designed using Autodesk Fusion 360. The fibre mat (blue) is strained between two holders, fixed through pressure and silver conductive paste. This ensures uniform force distribution at the fibre ends. The holders are connected by two stainless steel rods, with one fixed and the other movable. Tension is applied by weights (red) placed in an external boat, connected to the movable holder via a rod (yellow) that passes over a frictionless wheel to redirect force.

load across the fibre mat ends. A 100 g weight, corresponding to approximately 1 N of force, is employed due to its availability during initial testing. This force proves insufficient to induce significant fibre elongation. As a result, manual stretching is performed by applying force directly to the movable holder, leading to uneven and uncontrolled force transmission. To achieve more precise and uniform stretching, a motorised system with controlled force increments is recommended. Such systems enable consistent load application, reducing the risk of fibre breakage and facilitating greater elongation by allowing gradual, stepwise force increases.

The stretching system used for fibre elongation is shown in figure 5.16 A). An example illustrating the application of stretching force on the graphene-reinforced PAN mat is presented in figure 5.16 B).

The stretching ability of the fibre mat serves only as an initial indicator. To accurately evaluate the mechanical performance of the fibres, tensile testing is essential. This method applies a constant tensile load to a specimen until fracture, with displacement measurements under a known load used to generate a stress-strain curve. [174–176] From this, key mechanical metrics, including Youngs modulus and tensile strength, can be derived to assess the mechanical behaviour

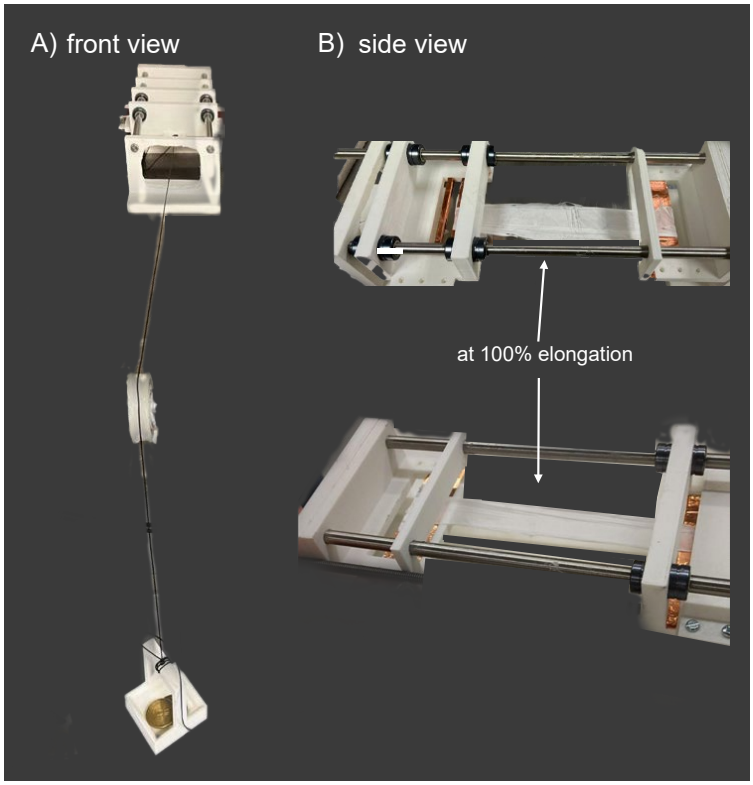

Figure 5.16: A) Front view of the prototype stretching system. B) Side view of the aligned graphene-reinforced fibre mat at 100 % elongation. The mat is produced via electrospinning of a PAN+graphene precursor solution, prepared through a shear-mixing process to synthesise graphene in a solution containing 6 wt% PAN. This production route is developed in this study.

of fibres. To achieve accurate results, equipment specifically engineered for nanofibre mats with minimal thickness is required, as conventional systems lack the sensitivity and resolution needed for such materials. A comprehensive testing protocol should include the systematic evaluation of PAN fibres (both standard and graphene-reinforced), aligned PAN fibres (with and without graphene), and their carbon-fibre derivatives. To support this analysis, the review of existing literature on the mechanical properties of electrospun fibres (see appendix .1) should be utilised. This approach ensures thorough mechanical characterisation across all variations, capturing the influence of graphene integration and fibre alignment.

6

Conclusion and future work

In this study, low-defect graphene is successfully synthesised in situ within the PAN polymer electrospinning precursor solution. The resulting graphene, produced with a 6 wt.% PAN polymer concentration dissolved in DMF during the shear-mixing step, has an estimated average thickness of nine layers and a concentration of 0.21 mg/ml in the electrospinning precursor solution. This work demonstrates the need to isolate graphene from other materials to ensure accurate characterisation. The fabricated fibres exhibit uniform morphology, with an average diameter of 228$\pm$45 nm, confirming the suitability of the precursor solution for fibre production. This is achieved by blending the shear-exfoliated graphene solution with a high-concentration 14 wt.% PAN solution, optimising the final solution concentration to fall within the electrospinning range and promote bead-free, uniform fibre formation. The resulting bead-free, homogeneous morphology points to effective graphene dispersion and the prevention of agglomeration within the polymer matrix, despite the absence of extended dispersion processes commonly reported in literature ([68, 70]). The successful integration of graphene, alongside its positive impact on mechanical properties that enables the fibres to be stretched up to three times more, indicates an increased structural order within the PAN precursor fibres. The chemical optimisation of PAN fibres through graphene reinforcement, as evidenced by their increased stretchability, forms a foundational step towards advancing the mechanical performance of carbon fibres, given the strong dependency of carbon fibre quality on the PAN precursor fibre.

To further optimise the conversion process from PAN to carbon fibres, future synthesis routes should incorporate electrical and mechanical stimuli. While previous studies have investigated isolated optimisation strategies, the combined application of thermal, chemical, electrical, and mechanical strategies remains largely unexplored. Potential strategies for this integrated approach include electro-carbonisation, flash-pyrolysis and electro-hot-stretching. Electro-carbonisation is proposed as a post-treatment method for converting polymer fibres into carbon fibres through electrical stimulation. The electrical stimulation, driven by Joule heating and electromigration, could increase defect mobility, thereby enhancing the process efficiency. [29, 177] Flash-pyrolysis refers to the rapid conversion of precursor material into carbon material. Consequently, applying electrical and mechanical stress could enhance the pyrolysis process and reduce the time and energy consumption. [29] Electro-hot-stretching aims to enhance the stretching efficiency of carbon nanofibres. Electrical stress, such as an applied electric field, is believed to increase material elasticity, thereby advancing stretching performance and promoting the uncoiling, reorienting, and aligning of molecular chains in the direction of the applied stretch force during stretching. It is theorised that electrical stress induces the sublimation of carbon atoms, which shift the fibre core and enhance material elasticity. [28] Leveraging the synergistic effects of these combined strategies represents a promising avenue for enhancing molecular orientation, reducing defects, and improving crystallinity. This approach has the potential to significantly improve the mechanical properties of carbon fibres, providing a pathway towards even more durable and higher-performing materials. Future research should also employ small-angle X-ray scattering (SAXS) measurements to investigate the orientation of graphene within PAN-based fibres, assessing its role within the fibre structure. This could provide valuable insights into the effect of graphene on fibre formation, aiding efforts to optimise carbon fibre production with increased crystallinity and fewer defects. Further mechanical performance testing on PAN precursor fibres should be conducted to examine the influence of various centrifugation parameters, allowing the effects of multi-layer graphene flakes (>10 layers) and graphite flakes on the fibre performance to be assessed.

Understanding the balance between the confinement effect of flakes larger than graphene and the role of graphene in the carbonisation process will be critical for optimising carbon nanofibre

production from graphene-reinforced PAN precursors.

TGA proves effective for identifying graphene and evaluating its quality within composites, even at low testing concentrations such as 0.21 mg/ml. At this low concentration of graphene, yield estimation in composites has been found unreliable.

To accurately identify materials by their decomposition temperature, especially at low concentrations, the deconvolution of the -DTG peaks is an essential step in this analysis. In this study, the thermal decomposition maxima for shear-exfoliated graphene are consistently observed at 412 °C and 724 °C, indicating similar material characteristics. However, Raman analysis reveals variations based on the polymer concentration. For instance, shear-mixing with a 6 wt.% polymer concentration yields an average of nine graphene layers, while a 9 wt.% polymer concentration results in seven layers—a deviation of two layers. Despite this variation, all shear-mixing processes involving polymer successfully generate graphene. While TGA does not have the resolution to differentiate between specific layer numbers, it reliably distinguishes between material components such as graphene and graphite, demonstrating high reproducibility under consistent experimental conditions.

This research demonstrates that TGA can be utilised as a cost-effective, rapid analysis method for material components and graphene classification. However, to ensure its effective application in industry, this study also highlights the necessity to build a robust and reliable reference data library, based on measurements specific to the unique characteristics of each experimental context and material of interest. This library should be based on TGA and standard characterisation techniques such as Raman spectroscopy, atomic force microscopy, and X-ray photoelectron spectroscopy. These methods provide the necessary data to establish a reliable reference system.

For instance, in this study, a characteristic shear-exfoliated graphene decomposition peak at 412 °C is identified, a finding not reported in other research. [72, 77, 79] In this context, if reference data from the literature alone had been applied, it may have introduced inaccuracies and misinterpretation of the properties of the material, preventing the correct classification of the material as graphene. This newly identified shear-exfoliated decomposition peak underscores the need for further research into commercially available graphene variants, as the current data

on rGO, graphene, graphite, and GO might overlook variations from the 20 scalable production processes used by over 500 companies worldwide.
Moreover, additional investigation is needed to determine why this peak at 412 °C appears specifically for shear-exfoliated graphene, utilising standard characterisation techniques to analyse samples decomposed at this temperature.

In summary, this synthesis method for graphene-reinforced, uniform PAN-based nanofibres offers a cost-effective and efficient approach to in situ production of low-defect graphene, fully integrated into the synthesis process as a precursor for high-performance carbon fibres. This ensures that the graphene produced meets classification standards, addressing the issue that commercially available graphene often fails to qualify as true graphene. [61] The introduction of rapid and inexpensive verification via TGA makes graphene identification more accessible to a wider range of applications and industries.

Appendices

.1 Fibres: mechanical performance

The properties of single nanofibres, especially the mechanical ones, have to be studied because they strongly influence the overall performance of the nanofibre material. When the mechanical performance of nanofibre mats is investigated, the result also depends on factors like the linkage between fibres or the alignment. For this reason, it is essential to study the properties of single nanofibres to gain a better understanding of the chemical, physical, and mechanical characteristics of the nanofibre structure. [4, 32, 178]

Table .1: State of the art - Mechanical single nanofibre testing: *Presented Parameters* ⇒ Polymer Material (Molecular weight M_w [kg/mol]; ES: Electrospinning parameter, volatage [kV], working distance [cm], pumpe rate [ml/h], disk collector take-up velocity [m/s or rpm], A.: Annealing, C. Carbonisation, Drawing time(mechanical stretching): λ; Diameter [nm]; Young' Modulus [GPa]; Tensile Strength [MPa]; Method= Tensile Testing: TT; AFM tensile testing: AFM-T; Mechanical resonance method: AFM-R, AFM based vertical three point bending method: AFM-B, Nanoindentation: NI, Peak Force Quantitative NanoMechanics mode test: QNM, Microelectromechanical system MEMS; Year; Reference: Ref.

Polymer	**Diameter** [nm]	**Young's Modulus** [GPa]	**Tensile Strength** [MPa]	**Method**	**Year**	**Ref.**
1:1 PCL($M_w = 80$):Fibrinogen + 9:1 HFP:DMEM → 100 mg/mL (**ES**: 20 kV, 15 cm, 0.8 ml/h)	230 ± 90	1.4 ± 0.99		AFM-B/OMS	2020	[179]
PCL($M_w = 120 - 300$) + HFP → 100 mg/mL, >30 days (**ES**: 20 kV, 15 cm, 0.8 ml/h)	440–1040	0.062 ± 0.026		AFM-B/OMS	2015	[180]
PCL($M_w = 120 - 300$) + HFP → 100 mg/mL, <30 days (**ES**: 20 kV, 15 cm, 0.8 ml/h)	440–1040	0.099 ± 0.084		AFM-B/OMS	2015	[180]
PCL($M_w = 80$) + 3:1 $CHCl_3$:CH_3OH (**ES**: 9-10 kV, 0.5 ml/h)	1400 ± 300	0.12 ± 0.03	40 ± 10	TT/SEM	2004	[181]
PCL($M_w = 80$) + 1:1 THF:DMF → 15 wt.% (**ES**: 12 kV, 18 cm, 1 ml/h)	250˜700	3.7 ± 0.7		AFM-B	2011	[182]
PCL($M_w = 80$) + 1:1 DMF:$CHCl_3$	$350 - 1000$	$0.25 - 0.35$	$68 - 50$	TT/SEM	2008	[183]
PA6:SiO_2 + HCOOH + 1:1 THF:DMF → → 4-25 wt.% (**ES**: 4-35 kV, 15 cm, 1 ml/h)	$600 - 100$	3.1˜6.9		AFM-B	2009	[184]
PA6 + 1:1 HCOOH :CH_3COOH → 12 wt.% (**ES**: 60 kV, 15 cm)	113.0 ± 16.3	1.32 ± 1.52	78.1 ± 6.0	AFM-T/SEM	2011	[185]

PA6 + HCOOH → 20 wt.% (**ES**: 15 kV, 8 cm, 0.2 ml/h)	~ 800	0.9	304	TT/SEM	2010	[186]
PA66 + HCOOH → 20 wt.% (**ES**: 30 kV, 5 ml/h, 5 m/s)	570 ± 40	0.45 ± 0.15	110 ± 14	AFM-T/SEM	2005	[187]
PA66 + HCOOH → 20 wt.% (**ES**: 30 kV, 5 ml/h, 20 m/s)	550 ± 120	0.95 ± 0.39	150 ± 49	AFM-T/SEM	2005	[187]
PA6(3)T ($M_w = 15$) + 99:1 DMF:$HCOOH$ → 22 wt.%, Hot press: 260 °C (**ES**: 35 kV, 42 cm, 0.12 ml/h)	170 ± 26	~ 5.5		TT/SEM	2011	[188]
PA6(3) T($M_w = 15$) + 99:1 DMF:$HCOOH$ → 30 wt.%, Hot press: 260 °C (**ES**: 40 kV, 33 cm, 0.6 ml/h)	612 ± 54	~ 3.68		TT/SEM	2011	[188]
PU + 1:1 DMF:THF (**ES**: 9-10 kV, 13 cm)	~ 150	~ 25		AFM-B	2018	[189]
PU + 1:1 DMF:THF (**ES**: 9-10 kV, 13 cm)	~ 300	~ 5		AFM-B	2018	[189]
TPU + 4:1 DMF:THF (**ES**: 14.5 kV, 25 cm, 0.6 ml/h)	1485 ± 53	0.048 ± 0.013	283.5 ± 13.5	TT/SEM	2014	[190]
PS($M_w = 230$)+ DMF → 0.3 g/mL (**ES**: 15 kV, 25 cm, 0.24 ml/h)	1767 ± 121	0.682 ± 0.04	19.8 ± 1.5	TT/SEM	2014	[190]
PAN+ DMF → 10 wt.% (**ES**: 18 kV, 15 cm)	~ 318	~ 5.72		AFM-T /SEM	2005	[191]
PAN+ DMF → 10 wt.% (**ES**: 22 kV, 15 cm)	~ 280	~ 26.55		AFM-T /SEM	2005	[191]
PAN($M_w = 150$) + DMF + → 9 wt.%, C.: 800 °C (**ES**: 25 kV, 25 cm)	$\sim 200 - 400$	80 ± 19	1860 ± 550	MEMS/SEM	2010	[192]
PAN($M_w = 150$) + DMF + → 9 wt.%, C.: 1100 °C (**ES**: 25 kV, 25 cm)	$\sim 200 - 350$	105 ± 27	2300 ± 700	MEMS/SEM	2010	[192]
PAN($M_w = 150$) + DMF + → 9 wt.%, C.: 1400 °C (**ES**: 25 kV, 25 cm)	$\sim 150 - 400$	172 ± 40	3520 ± 640	MEMS/SEM /(TEM)	2010	[192]
PAN($M_w = 150$) + DMF + → 9 wt.%, C.: 1700 °C (**ES**: 25 kV, 25 cm)	$\sim 150 - 500$	191 ± 58	2050 ± 700	MEMS/SEM	2010	[192]
1:83 PAN:DWNT + DMF + → 10.12 wt.%, C.: 800 °C (**ES**: 12 kV, 20 cm, 0.6 ml/h)	108	262	7300	MEMS/TEM	2013	[35]

1:83 PAN:DWNT + DMF + → 10.12 wt.%, C.: 800 °C (**ES**: 12 kV, 20 cm, 0.6 ml/h)	173	145	3400	MEMS/TEM	2013	[35]
PAN($M_w = 150$) + DMF + → 8 wt.%, C.: 1100 °C (**ES**: 0.9 kV/cm)	200 ± 5	61 ± 3.24	$300 - 400$	AFM-R/SEM /(TEM)	2005	[193]
PAN($M_w = 150$) + DMF → 8 wt.%, C.: 1100 °C (**ES**: 0.9 kV/cm)	150 ± 5	75.3 ± 3.08	$400 - 750$	AFM-R/SEM /(TEM)	2005	[193]
PAN($M_w = 150$) + DMF → 8 wt.%, C.: 1100 °C (**ES**: 0.9 kV/cm)	105 ± 5	57.6 ± 4.3	$550 - 900$	AFM-R/SEM /(TEM)	2005	[193]
coPAN (97:2:1 An:Ba:ITA + DMSO + AIBN)+ DMF → 7.5 wt.%, λ.: 1.4 (**ES**: 12 kV, 20 cm)	614.3	6.6 ± 0.5	367 ± 32	TT/AFM	2020	[173]
coPAN (97:2:1 An:Ba:ITA + DMSO + AIBN) + DMF → 7.5 wt.%, λ.: 2.2 (**ES**: 12 kV, 20 cm)	506.2	12.4 ± 1.0	595 ± 55	TT/AFM	2020	[173]
PAN (M_w=150) + DMF → 8-11 wt.%, A.: 130 °C (**ES**: 10-12 kV, 20 cm)	2800	0.36	15	TT/FE-SEM	2013	[43]
PAN (M_w=150) + DMF → 8-11 wt.%, A.: 130 °C (**ES**: 10-12 kV, 20 cm)	~ 100	48	1750	TT/FE-SEM	2013	[43]
PAN (M_w=150) + DMF → 10 wt.% (**ES**: 25 kV, 20 cm, 2 ml/h)	$300 - 600$	2-1.2	$60 - 45$	MEMS/SEM	2020	[194]
PAN (M_w=150) + DMF → 10 wt.% (**ES**: 25 kV, 20 cm, 2 ml/h)	$180 - 300$	5.5-3.5	$170 - 110$	MEMS/SEM	2020	[194]
PAN	200	26.8		AFM-R	2007	[195]
PAN + DMF → 9 wt.%	200 - 600	$6.3 - 1,5$	$200 - 90$	MEMS	2010	[196]
TiC/CNF = PAN+ PVP + $TiCl_4$+ DMF + H_2O , C.: 1000 °C (**ES**: 27 kV, 20 cm, 0.9 ml/h, 30 rpm)	284 ± 45	446		TT/SEM	2015	[197]
BFO + PVP + 1:2 C_3H_6O :DMF, A.: 600 °C	~ 700	52.5 ± 5.1		NI	2018	[198]
CFO + PVP + 1:1 H_2O :EtOH, A.: 600 °C	~ 700	146.2 ± 5.3		NI	2018	[198]
1:1 BFO:CFO + PVP + 1:2 C_3H_6O:DMF,	~ 700	90.3 ± 4.3		NI	2018	[198]

A.: 600 °C						
Al_2O_3= PVP + pseudo-boehmite nanocomposite+ + SiO_2 + EtOH → 5.5 wt.%, C.: 1300 °C (**ES**: 20 kV, 20 cm, 2.7 ml/h)	450	18.1 ± 4.9		AFM-B	2014	[199]
$V - ZnO$= PVP + EtOH + H_2O + $C_5H_8O_2$ + $ZnC_4H_6O_4$ → 0.038g/mol C.: 700 °C (**ES**: 25 kV, 18 cm, 1.8 ml/h)	$50 - 300$	58.7 ± 4.2		NI	2010	[200]
PZT + PVP + EtOH + CH_3COOH, A.:650 °C (**ES**: 10 kV)	300	42.99		AFM-B/SEM	2006	[201]
$SrTiO_3$ = PVP + TNBT + $C_4H_8O_5Sr$ + CH_3COOH ,C.: 650 °C (**ES**: 20 kV, 13.4 cm, 0.3 ml/h)	400	118 ± 3		QNM	2018	[202]
PZT + PVP + EtOH + CH_3COOH, A.: 650 °C (**ES**: 15 kV)	56	~ 70		AFM-R/SEM	2011	[203]
SnO_2= $C_4H_6O_4Sn$ + PVAc + DMF + $C_2H_4O_2$, C.: 600 °C (**ES**: 14 kV)	$160 - 350$	72.5959		AFM-B	2017	[204]
PVA (M_w=85-146) + $d.H_2O$ → 7-9 wt.% (**ES**: 12-15 kV, 15 cm)	130.6 ± 57.2	0.47 ± 0.27	62.2 ± 18.5	AFM-T/SEM	2011	[185]
PVA (M_w=85-146) + $d.H_2O$ → 6-13 wt.%	200-600	$6 - 1$		AFM-B	2012	[205]
PVA (M_w=85-146) + $d.H_2O$ → 6-13 wt.%	$70 - 200$	$14 - 4$		AFM-B	2012	[205]
PVA (M_w=127) + $d.H_2O$ (**ES**: 25 kV, 20 cm)	290 ± 11	2.1		NI	2013	[206]
PLLA (M_w=300) + 7:3 DCM:DMF → 1 wt.%, A.: 75 °C (**ES**: 12 kV, 1 ml/h)	217 ± 36	11.3 ± 2.7		AFM-B/SEM	2006	[38]
PLLA (M_w=300) + 7:3 DCM:DMF → 1 wt.% (**ES**: 12 kV, 1 ml/h)	230 ± 40	4.7 ± 1.2		AFM-B/SEM	2006	[38]
PLLA (M_w=300) + 7:3 DCM:DMF → 1 wt.% (**ES**: 12 kV, 1 ml/h)	230 ± 40	4.8 ± 1.9	204 ± 86	TT/SEM	2006	[38]
PLLA (M_w=100) + DCM → 9 wt.% (**ES**: 10 kV, 15 cm, 0.5 ml/h, 31.5 m/s)	346 ± 147	7.8 ± 2	343 ± 81	TT/SEM	2012	[37]

PLLA (M_w=700) + DCM → 1.75 wt.% (**ES**: 10 kV, 15 cm, 0.5 ml/h, 31.5 m/s)	399 ± 26	3.6 ± 0.3	150 ± 7	TT/SEM	2012	[37]
PLLA (M_w=300) + DCM → 1.75 wt.%, A.: $80\,^{\circ}C$ (**ES**: 10/15 kV, 0.5 ml/h, 1.05 m/s)	890 ± 190	1.0 ± 1.6	89 ± 40	TT/SEM	2005	[39]
PLLA (M_w=300) + DCM → 1.75 wt.%, A.: $80\,^{\circ}C$ (**ES**: 10/15 kV, 0.5 ml/h, 10.5 m/s)	610 ± 50	2.9 ± 0.4	183 ± 25	TT/SEM	2005	[39]
PLLA + DCM → 0.0015 wt.% (**ES**: 20 kV, 22 cm)	> 800	$\sim 1-3$		AFM-B/SEM	2018	[207]
PLLA + DCM → 0.015 wt.% (**ES**: 20 kV, 22 cm)	< 800	$\sim 3-12$		AFM-B/SEM	2018	[207]
PLLA (M_w=125) + DCM → 10 wt.% (**ES**: 7 kV, 7 cm)	~ 150	~ 7	~ 850	MEMS/SEM	2009	[208]
PLLA (M_w=125) + DCM → 10 wt.% (**ES**: 7 kV, 7 cm)	> 1000	$0-1.5$	$10-50$	MEMS/SEM	2009	[208]
L-PLA + DCM → 12 wt.% (**ES**: 20 kV, 15 cm, 1 ml/h, 31.5 m/s)	$500-700$	5.09 ± 2.24	184.1 ± 81.92	TT/SEM	2015	[209]
L-PLA + DCM → 12 wt.% (**ES**: 30 kV, 15 cm, 1 ml/h, 31.5 m/s)	$1000-2000$	2.88 ± 0.83	83.11 ± 14.2	TT/SEM	2015	[209]
Silk/PEO(M_w=900) + H_2O → 7.1 wt.% (**ES**: 12.5 kV, 21.5 cm, 1.8 ml/h)	800 ± 50	0.75 ± 0.06		NI/SEM	2004	[210]
PEO(M_w=100) + 1:1 H_2O:EtOH → 10-20 wt.%, C.:$850\,^{\circ}C$ (**ES**: 5-10 kV)	70 – 450	7.0 ± 0.5		AFM-B/SEM	2005	[211]
PEO(M_w=900) + H_2O → 6 wt.% (**ES**: 12 kV, 16 cm, 0.04 ml/h)	700	0.045		NI	2005	[212]
PEO + 1:4 H_2O:EtOH → 5 wt.% (**ES**: 8-10 kV, 0.12 ml/h)	500 ± 30	1.39 ± 0.35		NI	2009	[213]
PEO + 1:4 H_2O:EtOH → 5 wt.%, A.: $80\,^{\circ}C$ (**ES**: 8-10 kV, 0.12 ml/h)	500 ± 30	0.22 ± 0.04		NI	2009	[213]

1:5 Chi:PEO(M_w=900) + H_2O : $C_6H_8O_7$ + TritonX → 5.7 wt.%, A.: 80 °C (**ES**: 30 kV, 15 cm 0.5 ml/h)	280 ± 80	0.036 ± 0.012		NI/FE-SEM	2017	[214]
1:5 Chi:PEO(M_w=900) + H_2O : $C_6H_8O_7$ + TritonX → 5.7 wt.%, A.: 145 °C (**ES**: 30 kV, 15 cm 0.5 ml/h)	240 ± 25	2.15 ± 0.63		NI/FE-SEM	2017	[214]
PHBV + HV + 2:3 $C_2H_4Cl_2$:$CHCl_3$ → 12 wt.% (**ES**: 12 kV, 15 cm, 0.5 ml/h 7.8 m/s)	513 ± 75	2.67 ± 0.94	268 ± 52.2	TT/SEM	2009	[215]
PHBV + HV + 3:2 $C_2H_4Cl_2$:$CHCl_3$ → 12 wt.% (**ES**: 12 kV, 15 cm, 0.5 ml/h 15.7 m/s)	728 ± 98	1.22 ± 0.55	81.97 ± 31.78	TT/SEM	2009	[215]
BPAPC + THF → 14 wt.% (**ES**: 30 kV, 20 cm, 0.25 ml/h 1800 rpm)	∼ 340	∼ 2.11		AFM-B/FE-SEM	2010	[216]
BPAPC + THF → 14 wt.% (**ES**: 30 kV, 20 cm, 0.25 ml/h 1800 rpm)	∼ 270	∼ 2.86		AFM-B/FE-SEM	2010	[216]
BPAPC + THF → 14 wt.% (**ES**: 30 kV, 20 cm, 0.25 ml/h 1800 rpm)	∼ 992	∼ 0.04		AFM-B/FE-SEM	2010	[216]
PI = PAA + DMAc → 5 wt.%, A.: 370 °C (**ES**: 50 kV, 25 cm, 2.5 ml/h)	251 ± 57	37 ± 10	1666 ± 450	TT/SEM	2011	[217]
PI = PAA + DMAc → 3.5 wt.%, A.: 250 °C (**ES**: 100 kV/m 0.3 ml/h)	215 ± 12	23.5 ± 2.6	214 ± 21	AFM-T/SEM	2017	[40]
PI = PAA + DMAc → 3.5 wt.%, A.: 370 °C (**ES**: 100 kV/m 0.3 ml/h)	200 − 240	86.3 ± 6.5	1947 ± 118	AFM-T/SEM	2017	[40]
BPDA/PPA + DEMAB + DMAc → 3 wt.% (**ES**: 50 kV, 25 cm, 2.5 ml/h)		13 ± 0.39	766 ± 41	TT	2008	[178]
PI = BPDA/PPA + DEMAB + DMAc → 3 wt.%, A.: 430 °C (**ES**: 50 kV, 25 cm, 2.5 ml/h)	∼ 260	76 ± 12.6	1708 ± 118	TT	2008	[178]
PI = PAA + DMF → 4.5 wt.%, A.: 380 °C (**ES**: 25 kV, 0.5 ml/h, 2200 rpm)	∼ 275		∼ 1900	TT	2015	[218]
Co-PI = BPDA + ODA +	570 ± 68	59	1770	TT/SEM	2015	[219]

PRM + DMAc $\rightarrow$ 10 wt.% , A.: 330 $^{\circ}C$ (**ES**: 15 kV, 15 cm, 0.6 ml/h, 24 m/s)						
PI = PAA + DMAc+ DMEA + H_2O + EtOH , A.: 430 $^{\circ}C$ (**ES**: 30 kV, 35 cm, 10 ml/h, 24 m/s)	2320 ± 580	5.6	1064 ± 63	TT/SEM	2017	[220]
PI = PAA + DMF $\rightarrow$ 5.5 wt.%, A.: 370 $^{\circ}C$ (**ES**: 25 kV, 25 cm, 0.4 ml/h, 24 m/s)	325 ± 22	36.3 ± 3.7	2913 ± 152	TT/SEM	2020	[41]
PI/rGO = PAA/GO + DMF $\rightarrow$ 5.5 wt.%, A.: 370 $^{\circ}C$ (**ES**: 25 kV, 25 cm, 0.4 ml/h, 24 m/s)	314 ± 16	72.8 ± 4.9	3727 ± 248	TT/SEM	2020	[41]
PAMPS + H_2O + EtOH $\rightarrow$ 3.5 wt.% (**ES**: 0.67 kV/cm 0.12 ml/h, 24 m/s)	~ 55	~ 0.3		AFM-B	2006	[221]
PAMPS + H_2O + EtOH $\rightarrow$ 3.5 wt.% (**ES**: 0.67 kV/cm 0.12 ml/h, 24 m/s)	~ 110	~ 2.1		AFM-B	2006	[221]
1:9 PAA:NTCA-DAB $\rightarrow$ 10 wt.% ,A.: 500 $^{\circ}C$, C.: 1800 $^{\circ}C$ (**ES**: 15 kV, 15 cm, 1 ml/h, 24 m/s)		178.3 ± 40.7	56.5	QNM	2018	[222]
1:9 PAA:NTCA-DAB $\rightarrow$ 10 wt.% , C.: 2400 $^{\circ}C$ (**ES**: 15 kV, 15 cm, 1 ml/h, 24 m/s)	350	348 ± 57.1	19.4	QNM	2018	[222]

Bibliography

[1] Composites Manufacturing. Distribution of carbon fiber consumption worldwide in 2020 by end-use market [graph]. In Statista, February 2021. Retrieved December 18, 2023, from `https://www.statista.com/statistics/702145/global-carbon-fiber-consumption-share-by-end-use-market/`.

[2] G. Nie, X. Zhao, Y. Luan, J. Jiang, Z. Kou, and J. Wang. Key issues facing electrospun carbon nanofibers in energy applications: on-going approaches and challenges. *Nanoscale*, 12(25):13225–13248, 2020.

[3] Yaohui Zhang, Nana Wang, and Zhongchao Bai. The progress of cobalt-based anode materials for lithium ion batteries and sodium ion batteries. *Applied Sciences*, 10(9), 2020.

[4] Soheila Mohammadzadehmoghadam, Yu Dong, and Ian Jeffery Davies. Recent progress in electrospun nanofibers: Reinforcement effect and mechanical performance. *Journal of Polymer Science Part B: Polymer Physics*, 53(17):1171–1212, 2015.

[5] Sneha Chawla, Jizhe Cai, and Mohammad Naraghi. Mechanical tests on individual carbon nanofibers reveals the strong effect of graphitic alignment achieved via precursor hot-drawing. *Carbon*, 117:208–219, 2017.

[6] D. Papkov, N. Delpouve, L. Delbreilh, S. Araujo, T. Stockdale, S. Mamedov, K. Maleckis, Y. Zou, M. N. Andalib, E. Dargent, V. P. Dravid, M. V. Holt, C. Pellerin, and Y. A. Dzenis. Quantifying polymer chain orientation in strong and tough nanofibers with low crystallinity: Toward next generation nanostructured superfibers. *ACS Nano*, 13(5):4893–4927, 2019.

[7] Yuxi Yu, Zekai Tan, Jibin Zhang, and Guan-bin Liu. Microstructural evolution and mechanical investigation of hot stretched graphene oxide reinforced polyacrylonitrile nanofiber yarns. *Polymers for Advanced Technologies*, 31(9):1935–1945, 2020.

[8] Xinyue Wang, Qidong Zhao, Bin Yang, Zhongjian Li, Zheng Bo, Kwok Ho Lam, Nadia Mohd Adli, Lecheng Lei, Zhenhai Wen, Gang Wu, and Yang Hou. Emerging nanostructured carbon-based non-precious metal electrocatalysts for selective electrochemical co2 reduction to co. *Journal of Materials Chemistry A*, 7(44):25191–25202, 2019.

[9] Hamid Khayyam, Reza Nakhaie Jazar, Srinivas Nunna, Gelayol Golkarnarenji, Khashayar Badii, Seyed Mousa Fakhrhoseini, Satish Kumar, and Minoo Naebe. Pan precursor fabrication, applications and thermal stabilization process in carbon fiber production: Experimental and mathematical modelling. *Progress in Materials Science*, 107:100575, 2020.

[10] B. Saha and G. C. Schatz. Carbonization in polyacrylonitrile (pan) based carbon fibers studied by reaxff molecular dynamics simulations. *J Phys Chem B*, 116(15):4684–92, 2012.

[11] Mengying Zhang, Weiwei Liu, Hongqing Niu, and Dezhen Wu. Structure–property relationship of carbon fibers derived from polyimide/polyacrylonitrile blends. *High Performance Polymers*, 31(2):168–177, 2019.

[12] N. A. Munajat, A. H. Nurfaizey, A. A. M. Bahar, K. Y. You, S. H. S. M. Fadzullah, and G. Omar. High-frequency dielectric analysis of carbon nanofibers from pan precursor at different pyrolysis temperatures. *Microwave and Optical Technology Letters*, 60(9):2198–2204, 2018.

[13] R. Ojeda-López, G. Ramos-Sánchez, J. M. Esparza-Schulz, L. Lartundo, and A. Domínguez-Ortiz. On site formation of n-doped carbon nanofibers, an efficient electrocatalyst for fuel cell applications. *International Journal of Hydrogen Energy*, 42(51):30339–30348, 2017.

[14] D. Papkov, A. M. Beese, A. Goponenko, Y. Zou, M. Naraghi, H. D. Espinosa, B. Saha, G. C. Schatz, A. Moravsky, R. Loutfy, S. T. Nguyen, and Y. Dzenis. Extraordinary improvement of the graphitic structure of continuous carbon nanofibers templated with double wall carbon nanotubes. *ACS Nano*, 7(1):126–42, 2013.

[15] Biao Zhang, Feiyu Kang, Jean-Marie Tarascon, and Jang-Kyo Kim. Recent advances in electrospun carbon nanofibers and their application in electrochemical energy storage. *Progress in Materials Science*, 76:319–380, 2016.

[16] CW (Magazine). Compound annual growth rate of carbon fiber demand worldwide between 2016 and 2025, by market [graph]. In Statista, December 2016. Retrieved December 15, 2023, from `https://www.statista.com/statistics/689254/compound-annual-growth-rate-of-global-carbon-fiber-demand-by-market/`.

[17] MachineMFG. Carbon fiber vs. aluminum: A comprehensive comparison. 2024. Accessed: 2024-12-13.

[18] CCeV and AVK. Global demand for carbon fiber from 2010 to 2022 (in 1,000 metric tons) [graph]. In Statista, November 2018. Retrieved December 15, 2023, from `https://www.statista.com/statistics/380538/projection-demand-for-carbon-fiber-globally/`.

[19] Global carbon fibre market size, share, trends, forecast: By raw material: Pan-based carbon fibre, pitch-based carbon fibre; by type: Continuous carbon fibre, long carbon fibre, short carbon fibre; by form: Polymer matrix composites (pmc), others; by end use; regional analysis; market dynamics; competitive landscape; 2024-2032, Year of Publication. Accessed: Date of Access.

[20] A.B. Ali, D. Slawig, A. Schlosser, J. Koch, N.C. Bigall, F. Renz, C. Tegenkamp, and R. Sindelar. Polyacrylonitrile (pan) based electrospun carbon nanofibers (ecnfs): Probing the synergistic effects of creep assisted stabilization and cnts addition on graphitization and low dimensional electrical transport. *Carbon*, 172:283–295, 2021.

[21] Peng Xiao, Shujiao Zhang, Yanjun Gong, Yue Liu, Zhihong Li, and Dongfeng Li. Fractal structure change of pitch-based carbon fiber during high-temperature heat treatment. *Chemical Physics Letters*, 811:140239, 2023.

[22] Ting Wu, Chunxiang Lu, Tongqing Sun, Yonghong Li, Shuxia Yuan, Denghua Li, Guanbo Wang, and Xiaodan Ren. New discovery on the relationship between microstructure and tensile strength of pan-based carbon fibers. *Microporous and Mesoporous Materials*, 330:111584, 2022.

[23] Sai Ma, Jie Liu, Qian Liu, Jieying Liang, Yong Zhao, and Hao Fong. Investigation of structural conversion and size effect from stretched bundle of electrospun polyacrylonitrile copolymer nanofibers during oxidative stabilization. *Materials & Design*, 95:387–397, 2016.

[24] P Morgan. Carbon fibers and their composites, 2005.

[25] Deng hua Li, Chunxiang Lu, Sujun Du, Gang-Ping Wu, Yu Yang, and Li na Wang. Structural features of various kinds of carbon fibers as determined by small-angle x-ray scattering. *Applied Physics A*, 122:1–10, 2016.

[26] Harald Rennhofer, Dieter Loidl, Stephan Puchegger, and Herwig Peterlik. Structural development of pan-based carbon fibers studied by in situ x-ray scattering at high temperatures under load. *Carbon*, 48(4):964–971, 2010.

[27] Blesson Isaac, Robert M. Taylor, and Kenneth Reifsnider. Mechanical and dielectric properties of aligned electrospun fibers. *Fibers*, 9(1), 2021.

[28] J. Y. Huang, S. Chen, Z. F. Ren, G. Chen, and M. S. Dresselhaus. Real-time observation of tubule formation from amorphous carbon nanowires under high-bias joule heating. *Nano Lett*, 6(8):1699–705, 2006.

[29] Ruixin Ma, Donald Erb, and Kathy Lu. Flash pyrolysis of polymer-derived sioc ceramics. *Journal of the European Ceramic Society*, 38(15):4906–4914, 2018.

[30] Shilpa Shilpa and Ashutosh Sharma. Free standing hollow carbon nanofiber mats for supercapacitor electrodes. *RSC Advances*, 6(82):78528–78537, 2016.

[31] Lijun Yang, Pan Yang, Ruizhu Yang, Jingchuan Wang, Yawei Hao, and Xiaochong Zhao. Low-temperature fabrication of carbon nanofibers with improved graphitization via incorporating carbonaceous inclusions. *Polyhedron*, 164:13–16, 2019.

[32] Ahmed Barhoum, Mikhael Bechelany, and Abdel Salam Hamdy Makhlouf. *Handbook of Nanofibers*. Characterization and Evaluation of Nanofiber Materials. Springer, 2019.

[33] S. Ramakrishna, R. Jose, P. S. Archana, A. S. Nair, R. Balamurugan, J. Venugopal, and W. E. Teo. Science and engineering of electrospun nanofibers for advances in clean energy, water filtration, and regenerative medicine. *Journal of Materials Science*, 45(23):6283–6312, 2010.

[34] Hexcel Corporation. Hextow hm63: Product data sheet, 2020.

[35] Allison M. Beese, Dimitry Papkov, Shuyou Li, Yuris Dzenis, and Horacio D. Espinosa. In situ transmission electron microscope tensile testing reveals structure–property relationships in carbon nanofibers. *Carbon*, 60:246–253, 2013.

[36] Jian Yao, Cees W. M. Bastiaansen, and Ton Peijs. High strength and high modulus electrospun nanofibers. *Fibers*, 2(2):158–186, 2014.

[37] Xiwen Zhang, Ryohei Nakagawa, Kok Ho Kent Chan, and Masaya Kotaki. Mechanical property enhancement of polylactide nanofibers through optimization of molecular weight, electrospinning conditions, and stereocomplexation. *Macromolecules*, 45(13):5494–5500, 2012.

[38] E. P. Tan and C. T. Lim. Effects of annealing on the structural and mechanical properties of electrospun polymeric nanofibres. *Nanotechnology*, 17(10):2649–54, 2006.

[39] R. Inai, M. Kotaki, and S. Ramakrishna. Structure and properties of electrospun plla single nanofibres. *Nanotechnology*, 16(2):208–13, 2005.

[40] Shaohua Jiang, Donghua Han, Chaobo Huang, Gaigai Duan, and Haoqing Hou. Temperature-induced molecular orientation and mechanical properties of single electrospun polyimide nanofiber. *Materials Letters*, 216:81–83, 2018.

[41] Xiaoping Zhou, Chenhui Ding, Chuyun Cheng, Shuwu Liu, Gaigai Duan, Wenhui Xu, Kunming Liu, and Haoqing Hou. Mechanical and thermal properties of electrospun polyimide/rgo composite nanofibers via in-situ polymerization and in-situ thermal conversion. *European Polymer Journal*, 141, 2020.

[42] Miguel Moreno Raja, Pei Qi Lim, Yee Shan Wong, Gordon M. Xiong, Yiming Zhang, Subbu Venkatraman, and Yingying Huang. Chapter 18 - polymeric nanomaterials: Methods of preparation and characterization. In Shyam S. Mohapatra, Shivendu Ranjan, Nandita Dasgupta, Raghvendra Kumar Mishra, and Sabu Thomas, editors, *Nanocarriers for Drug Delivery*, Micro and Nano Technologies, pages 557–653. Elsevier, 2019.

[43] D. Papkov, Y. Zou, M. N. Andalib, A. Goponenko, S. Z. Cheng, and Y. A. Dzenis. Simultaneously strong and tough ultrafine continuous nanofibers. *ACS Nano*, 7(4):3324–31, 2013.

[44] Marie Richard-Lacroix and Christian Pellerin. Molecular orientation in electrospun fibers: From mats to single fibers. *Macromolecules*, 46:9473–9493, 2013.

[45] Ton Peijs, Robert Kirschbaum, and Pieter Jan Lemstra. Chapter 5: A critical review of carbon fiber and related products from an industrial perspective. *Advanced Industrial and Engineering Polymer Research*, 5(2):90–106, 2022. High-Performance Fibers.

[46] Marie Richard-Lacroix and Christian Pellerin. Molecular orientation in electrospun fibers: From mats to single fibers. *Macromolecules*, 46(24):9473–9493, 2013.

[47] Christian Pellerin, Robert E. Prud'homme, and Michel Pézolet. Orientation and relaxation study of miscible polystyrene/poly(vinyl methyl ether) blends. *Macromolecules*, 33(19):7009–7015, 2000.

[48] Mohamed B. Bazbouz, Atif Aziz, Davor Copic, Michael De Volder, and Mark E. Welland. Fabrication of high specific electrical conductivity and high ampacity carbon nanotube/copper composite wires. *Advanced Electronic Materials*, 7(4), 2021.

[49] Santosh K. Tiwari, Vijay Kumar, Andrzej Huczko, R. Oraon, A. De Adhikari, and G. C. Nayak. Magical allotropes of carbon: Prospects and applications. *Critical Reviews in Solid State and Materials Sciences*, 41(4):257–317, 2016.

[50] Boitumelo Makgabutlane, Lebea N. Nthunya, Manoko S. Maubane-Nkadimeng, and Sabelo D. Mhlanga. Green synthesis of carbon nanotubes to address the water-energy-food nexus: A critical review. *Journal of Environmental Chemical Engineering*, 9(1):104736, 2021.

[51] T. Carey, A. Alhourani, R. Tian, et al. Cyclic production of biocompatible few-layer graphene ink with in-line shear-mixing for inkjet-printed electrodes and li-ion energy storage. *npj 2D Materials and Applications*, 6(3), 2022.

[52] Arab H Hussein, Zhizhong Dong, Jennifer Lynch-Branzoi, Bernard H Kear, Jerry W Shan, Assimina A Pelegri, and Stephen D Tse. Graphene-reinforced polymer matrix composites fabricated by in situ shear exfoliation of graphite in polymer solution: processing, rheology, microstructure, and properties. *Nanotechnology*, 32(17):175703, feb 2021.

[53] BIS Research. Market value of graphene-enhanced composites worldwide in 2017 and 2023, by composite type (in million u.s. dollars) [graph]. In Statista, June 2018. Retrieved December 15, 2023, from `https://www.statista.com/statistics/960935/global-graphene-enhanced-composites-market-value-by-type/`.

[54] Dimitrios G. Papageorgiou, Ian A. Kinloch, and Robert J. Young. Mechanical properties of graphene and graphene-based nanocomposites. *Progress in Materials Science*, 90:75–127, 2017.

[55] Santosh K. Tiwari, Sumanta Sahoo, Nannan Wang, and Andrzej Huczko. Graphene research and their outputs: Status and prospect. *Journal of Science: Advanced Materials and Devices*, 5(1):10–29, 2020.

[56] Daniel Niyobuhungiro and Liu Hong. Graphene polymer composites: Review on fabrication method, properties and future perspectives. *Advances in Science and Technology Research Journal*, 15(1):37–49, 2021.

[57] Leo Rizzi, Andreas Zienert, Jörg Schuster, Martin Köhne, and Stefan E. Schulz. Electrical conductivity modeling of graphene-based conductor materials. *ACS Applied Materials & Interfaces*, 10(49):43088–43094, 2018.

[58] Soomook Lim, Hyunsoo Park, Go Yamamoto, Changgu Lee, and Ji Won Suk. Measurements of the electrical conductivity of monolayer graphene flakes using conductive atomic force microscopy. *Nanomaterials*, 11(10), 2021.

[59] Xiao-Xiong Wang, Gui-Feng Yu, Jun Zhang, Miao Yu, Seeram Ramakrishna, and Yun-Ze Long. Conductive polymer ultrafine fibers via electrospinning: Preparation, physical properties and applications. *Progress in Materials Science*, 115, 2021.

[60] Ossila. Graphene vs graphite, 2024. Accessed: 2024-06-16.

[61] Alan P. Kauling, Andressa T. Seefeldt, Diego P. Pisoni, Roshini C. Pradeep, Ricardo Bentini, Ricardo V. B. Oliveira, Konstantin S. Novoselov, and Antonio H. Castro Neto. The worldwide graphene flake production. *Advanced Materials*, 30(44):1803784, 2018.

[62] Yanyan Xu, Huizhe Cao, Yanqin Xue, Biao Li, and Weihua Cai. Liquid-phase exfoliation of graphene: An overview on exfoliation media, techniques, and challenges. *Nanomaterials*, 8(11), 2018.

[63] A. Rasyotra, A. Thakur, B. Gaykwad, et al. A review of low-cost approaches to synthesize graphene and its functional composites. *J Mater Sci*, 58:4359–4383, mar 2023.

[64] Lei Liu, Zhigang Shen, Min Yi, Xiaojing Zhang, and Shulin Ma. A green, rapid and size-controlled production of high-quality graphene sheets by hydrodynamic forces. *RSC advances*, 4(69):36464–36470, 2014.

[65] Ying Wei and Zhenyu Sun. Liquid-phase exfoliation of graphite for mass production of pristine few-layer graphene. *Current Opinion in Colloid & Interface Science*, 20(5):311–321, 2015.

[66] Rajatendu Sengupta, Mithun Bhattacharya, S. Bandyopadhyay, and Anil K. Bhowmick. A review on the mechanical and electrical properties of graphite and modified graphite reinforced polymer composites. *Progress in Polymer Science*, 36(5):638–670, 2011. Special Issue on Conducting Polymers.

[67] Mohammad A. Al-Saleh, Abdirahman A. Yussuf, Salah Al-Enezi, Roaya Kazemi, Mat Uzir Wahit, Tahani Al-Shammari, and Aseel Al-Banna. Polypropylene/graphene nanocomposites: Effects of gnp loading and compatibilizers on the mechanical and thermal properties. *Materials*, 12(23), 2019.

[68] Mohamed M. Abdel-Mottaleb, Alaa Mohamed, Shrouk A. Karim, Tarek A. Osman, and Aly Khattab. Preparation, characterization, and mechanical properties of polyacrylonitrile (pan)/graphene oxide (go) nanofibers. *Mechanics of Advanced Materials and Structures*, 27(4):346–351, 2020.

[69] Shichao Zhao, Sumedh P Surwade, Zhiting Li, and Haitao Liu. Photochemical oxidation of cvd-grown single layer graphene. *Nanotechnology*, 23(35):355703, aug 2012.

[70] Tahir Khan, Muhammad Aslam, Muhammad Basit, et al. Graphene-embedded electrospun polyacrylonitrile nanofibers with enhanced thermo-mechanical properties. *Journal of Nanoparticle Research*, 25(78):1–13, 2023.

[71] Yaxuan Yao, Lingling Ren, Sitian Gao, and Shi Li. Histogram method for reliable thickness measurements of graphene films using atomic force microscopy (afm). *Journal of Materials Science & Technology*, 33(8):815–820, 2017.

[72] Farzaneh Farivar, Pei Lay Yap, Kamrul Hassan, Tran Thanh Tung, Diana N.H. Tran, Andrew J. Pollard, and Dusan Losic. Unlocking thermogravimetric analysis (tga) in the fight against "fake graphene" materials. *Carbon*, 179:505–513, 2021.

[73] Dusan Losic, Farzaneh Farivar, and Pei Lay Yap. Refining and validating thermogravimetric analysis (tga) for robust characterization and quality assurance of graphene-related two-dimensional materials (gr2ms). *C*, 10(2), 2024.

[74] Pei Lay Yap, Farzaneh Farivar, Åsa K. Jämting, Victoria A. Coleman, Sam Gnaniah, Elisabeth Mansfield, Cheng Pu, Sandra Marcela Landi, Marcus Vinícius David, Emmanuel Flahaut, Mohammed Aizane, Michael Barnes, Mary Gallerneault, M. Dominique Locatelli, Sébastien Jacquinot, Carlton Gray Slough, Jörg Menzel, Stefan Schmölzer, Lingling Ren, Andrew J. Pollard, and Dusan Losic. International interlaboratory comparison of thermogravimetric analysis of graphene-related two-dimensional materials. *Analytical Chemistry*, 95(12):5176–5186, 2023. PMID: 36917706.

[75] A.G. Bannov, M.V. Popov, and P.B. Kurmashov. Thermal analysis of carbon nanomaterials: advantages and problems of interpretation. *J Therm Anal Calorim*, 142:349–370, oct 2020.

[76] Dusan Losic, Farzaneh Farivar, Pei Lay Yap, and Afshin Karami. Accounting carbonaceous counterfeits in graphene materials using the thermogravimetric analysis (tga) approach. *Analytical Chemistry*, 93(34):11859–11867, 2021. PMID: 34319694.

[77] Farzaneh Farivar, Pei Lay Yap, Ramesh Udayashankar Karunagaran, and Dusan Losic. Thermogravimetric analysis (tga) of graphene materials: Effect of particle size of graphene, graphene oxide and graphite on thermal parameters. *C*, 7(2), 2021.

[78] Yang Qiu, Felten Collin, Robert H. Hurt, and Indrek Külaots. Thermochemistry and kinetics of graphite oxide exothermic decomposition for safety in large-scale storage and processing. *Carbon*, 96:20–28, 2016.

[79] Ioannis Karnis, Fanourios Krasanakis, Labrini Sygellou, Anastassia N. Rissanou, Konstantinos Karatasos, and Kiriaki Chrissopoulou. Varying the degree of oxidation of graphite: effect of oxidation time and oxidant mass. *Phys. Chem. Chem. Phys.*, 26:10054–10068, 2024.

[80] Umar Khan, Arlene O'Neill, Harshit Porwal, Peter May, Khalid Nawaz, and Jonathan N. Coleman. Size selection of dispersed, exfoliated graphene flakes by controlled centrifugation. *Carbon*, 50(2):470–475, 2012.

[81] Liubov A. Belyaeva and Grégory F. Schneider. Wettability of graphene. *Surface Science Reports*, 75(2):100482, 2020.

[82] KL Ng, BM Maciejewska, L Qin, C Johnston, J Barrio, M-M Titirici, I Tzanakis, DG Eskin, K Porfyrakis, J Mi, and N Grobert. Direct evidence of the exfoliation efficiency and graphene dispersibility of green solvents toward sustainable graphene production. *ACS Sustainable Chemistry & Engineering*, 11(1):58–66, 2022.

[83] AMETEK Brookfield. What is Viscosity? - Learn About Viscosity, 2024. Accessed: 2024-06-17.

[84] Ahmed Olatunde, Mayowa Shakirdeen Obidola, and Habibu Tijjani. Chapter 3 - centrifugation techniques. In Chukwuebuka Egbuna, Kingsley C. Patrick-Iwuanyanwu, Muhammad Ajmal Shah, Jonathan C. Ifemeje, and Azhar Rasul, editors, *Analytical Techniques in Biosciences*, pages 43–58. Academic Press, 2022.

[85] Gregory A DiLisi. *Classical Mechanics, Volume 5*. 2053-2571. Morgan & Claypool Publishers, 2019.

[86] Science Notes. Centrifugal force - definition, formula, examples, 2024. Accessed: 2024-12-18.

[87] D. Phil Childs BSc.(Hons). *Rotating Flow*. Elsevier Science & Technology, London, 1 edition, 2010. Print ISBN: 9780123820983, E-Book ISBN: 9780123820990.

[88] David Halliday, Jearl Walker, and Robert Resnick. *Fundamentals of physics*. Wiley, Hoboken, 7th edition. edition, 2005.

[89] Calculator Academy. Rpm to angular velocity calculator, 2024. Accessed: 2024-12-18.

[90] A. Arifutzzaman, A. F. Ismail, I. I. Yaacob, M. Z. Alam, and A. A. Khan. Experimental investigation of concentration yields of liquid phase exfoliated graphene in organic solvent media. In *Materials Science and Engineering Conference Series*, volume 488 of *Materials Science and Engineering Conference Series*, page 012001, March 2019.

[91] Claudia Backes, Thomas M. Higgins, Adam Kelly, Conor Boland, Andrew Harvey, Damien Hanlon, and Jonathan N. Coleman. Guidelines for exfoliation, characterization and processing of layered materials produced by liquid exfoliation. *Chemistry of Materials*, 29(1):243–255, 2017.

[92] D.N. Taulbee and M. Mercedes Maroto-Valer. Centrifugation. In Ian D. Wilson, editor, *Encyclopedia of Separation Science*, pages 17–40. Academic Press, Oxford, 2000.

[93] Merck Millipore. Millex-gp, 0.22 µm, pes, 47 mm, gamma-sterilized, 2024. Accessed: 2024-07-16.

[94] Andrea C. Ferrari. Raman spectroscopy of graphene and graphite: Disorder, electron–phonon coupling, doping and nonadiabatic effects. *Solid State Communications*, 143(1):47–57, 2007. Exploring graphene.

[95] A. C. Ferrari and J. Robertson. Interpretation of raman spectra of disordered and amorphous carbon. *Phys. Rev. B*, 61:14095–14107, May 2000.

[96] Andrea C. Ferrari and Denis M. Basko. Raman spectroscopy as a versatile tool for studying the properties of graphene. *Nature Nanotechnology*, 8(4):235–246, 2013.

[97] Andrea C. Ferrari. Raman spectroscopy of graphene and graphite: Disorder, electron–phonon coupling, doping and nonadiabatic effects. *Solid State Communications*, 143(1):47–57, 2007. Exploring graphene.

[98] Axel Eckmann, Alexandre Felten, Artem Mishchenko, Liam Britnell, Ralph Krupke, Kostya S. Novoselov, and Cinzia Casiraghi. Probing the nature of defects in graphene by raman spectroscopy. *Nano Letters*, 12(8):3925–3930, 2012. PMID: 22764888.

[99] L.M. Malard, M.A. Pimenta, G. Dresselhaus, and M.S. Dresselhaus. Raman spectroscopy in graphene. *Physics Reports*, 473(5):51–87, 2009.

[100] M. V. Bracamonte, G. I. Lacconi, S. E. Urreta, and L. E. F. Foa Torres. On the nature of defects in liquid-phase exfoliated graphene. *The Journal of Physical Chemistry C*, 118(28):15455–15459, 2014.

[101] Z. Peng, X. Chen, Y. Fan, et al. Strain engineering of 2d semiconductors and graphene: from strain fields to band-structure tuning and photonic applications. *Light: Science & Applications*, 9:190, 2020.

[102] G. Sh. Shmavonyan, G. G. Sevoyan, and V. M. Aroutiounian. Enlarging the surface area of monolayer graphene synthesized by mechanical exfoliation. *Department of Microelectronics and Biomedical Devices, State Engineering University of Armenia*, 2012. Received 12 November, 2012.

[103] A C Ferrari, J C Meyer, V Scardaci, C Casiraghi, M Lazzeri, F Mauri, S Piscanec, D Jiang, K S Novoselov, S Roth, and A K Geim. Raman spectrum of graphene and graphene layers. *Physical review letters.*, 97(18):187401, 2006-10-30.

[104] Dominique B. Schuepfer, Felix Badaczewski, Juan Manuel Guerra-Castro, Detlev M. Hofmann, Christian Heiliger, Bernd Smarsly, and Peter J. Klar. Assessing the structural properties of graphitic and non-graphitic carbons by raman spectroscopy. *Carbon*, 161:359–372, 2020.

[105] C. Ferrante, A. Virga, L. Benfatto, G. Cerullo, G. Galimberti, G. Ferrini, and T. Scopigno. Raman spectroscopy of graphene under ultrafast laser excitation. *Nature Communications*, 9:308, 2018.

[106] Akira Yoshida, Yutaka Kaburagi, and Yoshihiro Hishiyama. Full width at half maximum intensity of the g band in the first order raman spectrum of carbon material as a parameter for graphitization. *Carbon*, 44(11):2333–2335, 2006.

[107] Konstantin N. Kudin, Bulent Ozbas, Hannes C. Schniepp, Robert K. Prud'homme, Ilhan A. Aksay, and Roberto Car. Raman spectra of graphite oxide and functionalized graphene sheets. *Department of Chemistry and Department of Chemical Engineering, Princeton University*, 2007. Received July 26, 2007; Revised Manuscript Received October 25, 2007.

[108] Wenjing Wu, Jeewan C. Ranasinghe, Arka Chatterjee, and Shengxi Huang. Recent advances on raman spectroscopy of graphene: towards biosensing applications. *Materials Chemistry and Physics*, 318:129281, 2024.

[109] N. M. S. Hidayah, Wei-Wen Liu, Chin-Wei Lai, N. Z. Noriman, Cheng-Seong Khe, U. Hashim, and H. Cheun Lee. Comparison on graphite, graphene oxide and reduced graphene oxide: Synthesis and characterization. *AIP Conference Proceedings*, 1892(1):150002, 10 2017.

[110] I. Moon, J. Lee, R. S. Ruoff, and S. Park. Reduced graphene oxide by chemical graphitization. *Nature Communications*, 1:73, 2010.

[111] Pawan Kumar Srivastava and Subhasis Ghosh. Synthesis and characterization of single and few layer graphene for field effect transistor. In P. K. Giri, D. K. Goswami, and A. Perumal, editors, *Advanced Nanomaterials and Nanotechnology*, pages 159–164, Berlin, Heidelberg, 2013. Springer Berlin Heidelberg.

[112] F. Hassan, R. Batmaz, J. Li, et al. Evidence of covalent synergy in silicon–sulfur–graphene yielding highly efficient and long-life lithium-ion batteries. *Nat Commun*, 6:8597, 2015.

[113] Keqing Zhou, Yongqian Shi, Saihua Jiang, Lei Song, Yuan Hu, and Zhou Gui. A facile liquid phase exfoliation method to prepare graphene sheets with different sizes expandable graphite. *Materials Research Bulletin*, 48(9):2985–2992, 2013.

[114] N. Chadha, R. Sharma, and P. Saini. A new insight into the structural modulation of graphene oxide upon chemical reduction probed by raman spectroscopy and x-ray diffraction. *Carbon Letters*, 31:1125–1131, 2021.

[115] M. Grande, G. Bianco, M. Vincenti, D. de Ceglia, D. Tosi, N. Aközbek, and M. Scalora. Optically transparent microwave polarizer based on quasi-metallic graphene. *Scientific Reports*, 5:17083, 2015.

[116] KR Paton, E Varrla, C Backes, RJ Smith, U Khan, A O'Neill, C Boland, M Lotya, OM Istrate, P King, T Higgins, S Barwich, P May, P Puczkarski, I Ahmed, M Moebius, H Pettersson, E Long, J Coelho, SE O'Brien, EK McGuire, BM Sanchez, GS Duesberg, N McEvoy, TJ Pennycook, C Downing, A Crossley, V Nicolosi, and JN Coleman. Scalable production of large quantities of defect-free few-layer graphene by shear exfoliation in liquids. *Nat Mater*, 13(6):624–630, jun 2014.

[117] Patrik Johansson, Magnus Edvardsson, Josefina Adebahr, and Per Jacobsson. Mixed solvent and polymer coordination in pan and pmma gel polymer electrolytes studied by ab initio calculations and raman spectroscopy. *The Journal of Physical Chemistry B*, 107(46):12622–12627, 2003.

[118] Y. S. Huang and J. L. Koenig. Raman spectra of polyacrylonitrile. *Applied Spectroscopy*, 25(6):620–622, 1971.

[119] Jiang-Bin Wu, Miao-Ling Lin, Xin Cong, He-Nan Liu, and Ping-Heng Tan. Raman spectroscopy of graphene-based materials and its applications in related devices. *Chem. Soc. Rev.*, 47:1822–1873, 2018.

[120] I. Childres, Luis Jauregui, W. Park, H. Caoa, and Y.P. Chena. Raman spectroscopy of graphene and related materials. *New Developments in Photon and Materials Research*, pages 403–418, 01 2013.

[121] Debarun Sengupta, Ssu-Han Chen, Aron Michael, Chee Yee Kwok, Sean Lim, Yutao Pei, and Ajay Giri Prakash Kottapalli. Single and bundled carbon nanofibers as ultralightweight and flexible piezoresistive sensors. *npj Flexible Electronics*, 4(1), 2020.

[122] Gerald A. Zickler, Bernd Smarsly, Notburga Gierlinger, Herwig Peterlik, and Oskar Paris. A reconsideration of the relationship between the crystallite size la of carbons determined by x-ray diffraction and raman spectroscopy. *Carbon*, 44(15):3239–3246, 2006.

[123] A. C. Ferrari, J. C. Meyer, V. Scardaci, C. Casiraghi, M. Lazzeri, F. Mauri, S. Piscanec, D. Jiang, K. S. Novoselov, S. Roth, and A. K. Geim. Raman spectrum of graphene and graphene layers. *Phys. Rev. Lett.*, 97:187401, Oct 2006.

[124] Ferdinando Giannazzo. *The Atomic Force Microscopy for Nanoelectronics*, pages 1–24. Springer International Publishing, Cham, 2019.

[125] Bert Voigtländer. *Introduction, & Artifacts in AFM*, pages 1–12 & 137–147. Springer International Publishing, Cham, 2019.

[126] Zhihao Li, Xiucai Sun, Xiaoli Sun, Wan-Jian Yin, and Zhongfan Liu. Substrate screening for superclean graphene growth using first-principles calculations. *Nano Research*, 17(4):2216–2222, 2024.

[127] Viet Phuong Pham, Hyeon-Sik Jang, Dongmok Whang, and Jae-Young Choi. Direct growth of graphene on rigid and flexible substrates: progress, applications, and challenges. *Chem. Soc. Rev.*, 46:6276–6300, 2017.

[128] Tianyou Zhang, Dong Zhang, and Ming Shen. A low-cost method for preliminary separation of reduced graphene oxide nanosheets. *Materials Letters*, 63(23):2051–2054, 2009.

[129] Shuai Wang, Min Yi, and Zhigang Shen. The effect of surfactants and their concentration on the liquid exfoliation of graphene. *RSC Adv.*, 6:56705–56710, 2016.

[130] Bhim Prasad Kafle. Chapter 2 - theory and instrumentation of absorption spectroscopy: Uv–vis spectrophotometry and colorimetry. In Bhim Prasad Kafle, editor, *Chemical Analysis and Material Characterization by Spectrophotometry*, pages 17–38. Elsevier, 2020.

[131] Huaiyu Wang and Paul K. Chu. Chapter 4 - surface characterization of biomaterials. In Amit Bandyopadhyay and Susmita Bose, editors, *Characterization of Biomaterials*, pages 105–174. Academic Press, Oxford, 2013.

[132] AE Niaraki Asli, J Guo, PL Lai, R Montazami, and NN Hashemi. High-yield production of aqueous graphene for electrohydrodynamic drop-on-demand printing of biocompatible conductive patterns. *Biosensors (Basel)*, 10(1):6, 2020.

[133] Subrata Pandit and Mrinmoy De. Empirical correlation and validation of lateral size-dependent absorption coefficient of graphene oxides. *ChemistrySelect*, 2(31):10004–10009, 2017.

[134] Valeria Alzari, Daniele Nuvoli, Roberta Sanna, Laura Peponi, Massimo Piccinini, Silvia Bittolo Bon, Salvatore Marceddu, Luca Valentini, José María Kenny, and Alberto Mariani. Multistimuli-responsive hydrogels of poly(2-acrylamido-2-methyl-1-propanesulfonic acid) containing graphene. *Colloid and Polymer Science*, 291:2681–2687, 2013.

[135] R. Bruce Prime, Harvey E. Bair, Sergey Vyazovkin, Patrick K. Gallagher, and Alan Riga. Thermogravimetric analysis (tga). In Joseph D. Menczel and R. Bruce Prime, editors, *Thermal Analysis of Polymers: Fundamentals and Applications*, page 241. John Wiley & Sons, Inc., San Jose, CA, 2009.

[136] Michael Shtein, Ilan Pri-Bar, Maxim Varenik, and Oren Regev. Characterization of graphene-nanoplatelets structure via thermogravimetry. *Analytical Chemistry*, 87(8):4076–4080, 2015. PMID: 25796961.

[137] Herianto Lim. Peakfit: A peak fitting tool. `https://github.com/heriantolim/PeakFit`, 2023.

[138] George H. Major, Neal Fairley, Peter M. A. Sherwood, Matthew R. Linford, Jeff Terry, Vincent Fernandez, and Kateryna Artyushkova. Practical guide for curve fitting in x-ray photoelectron spectroscopy. *Journal of Vacuum Science & Technology A*, 38(6):061203, 10 2020.

[139] Bashar Alsadik. Chapter 11 - introduction to the adjustment with levenberg–marquardt method. In Bashar Alsadik, editor, *Adjustment Models in 3D Geomatics and Computational Geophysics*, volume 4 of *Computational Geophysics*, pages 327–344. Elsevier, 2019.

[140] Henri P. Gavin. The levenberg-marquardt algorithm for nonlinear least squares curve-fitting problems, November 2022. Available online.

[141] Christopher D. Easton, Calum Kinnear, Sally L. McArthur, and Thomas R. Gengenbach. Practical guides for x-ray photoelectron spectroscopy: Analysis of polymers. *Journal of Vacuum Science & Technology A*, 38(2):023207, 02 2020.

[142] Varun Jain, Mark C. Biesinger, and Matthew R. Linford. The gaussian-lorentzian sum, product, and convolution (voigt) functions in the context of peak fitting x-ray photoelectron spectroscopy (xps) narrow scans. *Applied Surface Science*, 447:548–553, 2018.

[143] MathWorks. makima - Modified Akima piecewise cubic Hermite interpolation. `https://uk.mathworks.com/help/matlab/ref/makima.html#mw_e8ee1c8c-2cc3-46c4-90c4-c3208804ff4e`, 2019. Accessed: [Insert Date of Access].

[144] Nima Mohamadbeigi, Shayan Angizi, Sayed Khatiboleslam Sadrnezhaad, and Mohammad Javad Nikzad. Improving the multi-step fabrication approach of copper nanofiber networks based transparent electrode for achieving superb conductivity and transparency. *Materials Research Express*, 6(9), 2019.

[145] Jan Lukas Storck, Timo Grothe, Khorolsuren Tuvshinbayar, Elise Diestelhorst, Daria Wehlage, Bennet Brockhagen, Martin Wortmann, Natalie Frese, and Andrea Ehrmann. Stabilization and incipient carbonization of electrospun polyacrylonitrile nanofibers fixated on aluminum substrates. *Fibers*, 8(9), 2020.

[146] G. Konstantopoulos, S. Soulis, D. Dragatogiannis, and C. Charitidis. Introduction of a methodology to enhance the stabilization process of pan fibers by modeling and advanced characterization. *Materials (Basel)*, 13(12), 2020.

[147] Patrycja Musiol, Piotr Szatkowski, Maciej Gubernat, Aleksandra Weselucha-Birczynska, and Stanislaw Blazewicz. Comparative study of the structure and microstructure of pan-based nano- and micro-carbon fibers. *Ceramics International*, 42(10):11603–11610, 2016.

[148] S. J. B. Reed. *Scanning electron microscopy*, page 41–75. Cambridge University Press, 2005.

[149] Anwar Ul-Hamid. *A Beginners' Guide to Scanning Electron Microscopy*. Springer Cham, 1 edition, 2018. XXII, 402 pages, 122 b/w illustrations, 98 illustrations in colour.

[150] Leica Microsystems. Brief introduction to coating technology for electron microscopy. `https://www.leica-microsystems.com/science-lab/life-science/brief-introduction-to-coating-technology-for-electron-microscopy/`, 2024. Accessed: Dec. 22, 2024.

[151] Nanoscience Instruments. Gold vs platinum: Choosing the right coating for sem imaging. `https://www.nanoscience.com/blogs/gold-vs-platinum-choosing-the-right-coating-for-sem-imaging/`, 2024. Accessed: Dec. 22, 2024.

[152] Rod Heu, Sina Shahbazmohamadi, John Yorston, and Patrick Capeder. Target material selection for sputter coating of sem samples. *Microscopy Today*, 27(4):32–36, 2019.

[153] Na Meng, Xiangqin Wang, Binjie Xin, Zhuoming Chen, and Yan Liu. Preparation, structure and electrochromic behavior of pani/pva composite electrospun nanofiber. *Textile Research Journal*, 89(12):2490–2499, 2018.

[154] Seeram Ramakrishna, Kazutoshi Fujihara, Wee-Eong Teo, Thomas Yong, Zuwei Ma, and Ramakrishna Ramaseshan. Electrospun nanofibers: solving global issues. *Materials Today*, 9(3):40–50, 2006.

[155] David Brandon and Wayne D. Kaplan. Microstructural characterization of materials. *John Wiley & Sons*, 2nd Edition, 2008.

[156] S. Suresh, A. Becker, and B. Glasmacher. Impact of apparatus orientation and gravity in electrospinning-a review of empirical evidence. *Polymers (Basel)*, 12(11), 2020.

[157] Ya Huang, Jianan Song, Cheng Yang, Yuanzheng Long, and Hui Wu. Scalable manufacturing and applications of nanofibers. *Materials Today*, 28:98–113, 2019.

[158] S. Thenmozhi, N. Dharmaraj, K. Kadirvelu, and Hak Yong Kim. Electrospun nanofibers: New generation materials for advanced applications. *Materials Science and Engineering: B*, 217:36–48, 2017.

[159] Geon Hwee Kim, Hyoryung Nam, WooSeok Choi, Taechang An, and Geunbae Lim. Electrospinning nanofiber on an insulating surface with a patterned functional electrolyte electrode. *Advanced Materials Interfaces*, 5(5), 2018.

[160] M. Toriello, M. Afsari, H. K. Shon, and L. D. Tijing. Progress on the fabrication and application of electrospun nanofiber composites. *Membranes (Basel)*, 10(9), 2020.

[161] Linlin Li, Shengjie Peng, Jeremy Kong Yoong Lee, Dongxiao Ji, Madhavi Srinivasan, and Seeram Ramakrishna. Electrospun hollow nanofibers for advanced secondary batteries. *Nano Energy*, 39:111–139, 2017.

[162] T. R. Pozegic, S. G. King, M. Fotouhi, V. Stolojan, S. R. P. Silva, and I. Hamerton. Delivering interlaminar reinforcement in composites through electrospun nanofibres. *Advanced Manufacturing: Polymer & Composites Science*, 5(4):155–171, 2019.

[163] S. Y. Gu, J. Ren, and G. J. Vancso. Process optimization and empirical modeling for electrospun polyacrylonitrile (pan) nanofiber precursor of carbon nanofibers. *European Polymer Journal*, 41(11):2559–2568, 2005.

[164] Nor Hasrul Akhmal Ngadiman, M. Y. Noordin, Ani Idris, Amira Shakim Abdul Shakir, and Denni Kurniawan. Influence of polyvinyl alcohol molecular weight on the electrospun nanofiber mechanical properties. *Procedia Manufacturing*, 2:568–572, 2015.

[165] Md Shariful Islam, Bee Chin Ang, Andri Andriyana, and Amalina Muhammad Afifi. A review on fabrication of nanofibers via electrospinning and their applications. *SN Applied Sciences*, 1(10), 2019.

[166] Muhammad Omer Aijaz, Mohammad Rezaul Karim, Hamad F. Alharbi, and Nabeel H. Alharthi. Novel optimised highly aligned electrospun pei-pan nanofibre mats with excellent wettability. *Polymer*, 180, 2019.

[167] Jun-Jye Ng and Pitt Supaphol. Rotating-disk electrospinning: needleless electrospinning of poly(caprolactone), poly(lactic acid) and poly(vinyl alcohol) nanofiber mats with controlled morphology. *Journal of Polymer Research*, 25(7), 2018.

[168] Niloufar Sabetzadeh, Ali Akbar Gharehaghaji, and Mehran Javanbakht. Porous pan micro/nanofiber membranes with potential application as lithium-ion battery separators: physical, morphological and thermal properties. *Journal of Polymer Research*, 26(1), 2019.

[169] Domitille Mailley, Anne Hebraud, and Guy Schlatter. A review on the impact of humidity during electrospinning: From the nanofiber structure engineering to the applications. *Macromolecular Materials and Engineering*, page 2100115, 2021. HAL Id: hal-03217580.

[170] Zhengping Zhou, Chuilin Lai, Lifeng Zhang, Yong Qian, Haoqing Hou, Darrell H. Reneker, and Hao Fong. Development of carbon nanofibers from aligned electrospun polyacrylonitrile nanofiber bundles and characterization of their microstructural, electrical, and mechanical properties. *Polymer*, 50(13):2999–3006, 2009.

[171] Xinlu Li, Yujie Zhao, Yu Bai, Xiyu Zhao, Ronghua Wang, Yanchun Huang, Qinghua Liang, and Zhenghong Huang. A non-woven network of porous nitrogen-doping carbon nanofibers as a binder-free electrode for supercapacitors. *Electrochimica Acta*, 230:445–453, 2017.

[172] Juan Emmanuel Ruiz Rocha, Karla Rebeca Moreno Tovar, Ricardo Navarro Mendoza, Silvia Gutiérrez Granados, Sara Cavaliere, Domitille Giaume, Philippe Barboux, and Jesús Salvador Jaime Ferrer. Critical electrospinning parameters for synthesis control of stabilized polyacrylonitrile nanofibers. *Nanomaterials*, 13(19), 2023.

[173] Tang-Cheng Xu, Dong-Hua Han, Yong-Mei Zhu, Gai-Gai Duan, Kun-Ming Liu, and Hao-Qing Hou. High strength electrospun single copolyacrylonitrile (copan) nanofibers with improved molecular orientation by drawing. *Chinese Journal of Polymer Science*, 2020.

[174] Danny Schaeffler. Tensile testing part 1: Equipment, samples and procedures. `www.metalformingmagazine.com/article/?/quality-control/material-testing/tensile-testing-part-1-3a-equipment-2c-samples-and-procedure`, April 2020. Accessed: Date of Access.

[175] Ridwan Ridwan, Aditya Rio Prabowo, Nurul Muhayat, Teguh Putranto, and Jung Min Sohn. Tensile analysis and assessment of carbon and alloy steels using fe approach as an idealization of material fractures under collision and grounding. *Curved and Layered Structures*, 7(1):188–198, 2020.

[176] J. R. Davis. *Tensile Testing*. ASM International, 2004. Accessed via ProQuest Ebook Central.

[177] B. Wang, D. E. Wolfe, M. Terrones, M. A. Haque, S. Ganguly, and A. K. Roy. Electro-graphitization and exfoliation of graphene on carbon nanofibers. *Carbon*, 117:201–207, 2017.

[178] Fei Chen, Xinwen Peng, Tingting Li, Shuiliang Chen, Xiang-Fa Wu, Darrell H. Reneker, and Haoqing Hou. Mechanical characterization of single high-strength electrospun polyimide nanofibres. *Journal of Physics D: Applied Physics*, 41(2), 2008.

[179] J. M. Sharpe, H. Lee, A. R. Hall, K. Bonin, and M. Guthold. Mechanical properties of electrospun, blended fibrinogen: Pcl nanofibers. *Nanomaterials (Basel)*, 10(9), 2020.

[180] S. R. Baker, S. Banerjee, K. Bonin, and M. Guthold. Determining the mechanical properties of electrospun poly-epsilon-caprolactone (pcl) nanofibers using afm and a novel fiber anchoring technique. *Mater Sci Eng C Mater Biol Appl*, 59:203–212, 2016.

[181] E. P. Tan, S. Y. Ng, and C. T. Lim. Tensile testing of a single ultrafine polymeric fiber. *Biomaterials*, 26(13):1453–6, 2005.

[182] F. Croisier, A. S. Duwez, C. Jerome, A. F. Leonard, K. O. van der Werf, P. J. Dijkstra, and M. L. Bennink. Mechanical testing of electrospun pcl fibers. *Acta Biomater*, 8(1):218–24, 2012.

[183] Shing-Chung Wong, Avinash Baji, and Siwei Leng. Effect of fiber diameter on tensile properties of electrospun poly(ϵ-caprolactone). *Polymer*, 49(21):4713–4722, 2008.

[184] Yanhuai Ding, Ping Zhang, Yong Jiang, Fu Xu, Jiuren Yin, and Yongde Zuo. Mechanical properties of nylon-6/sio2 nanofibers prepared by electrospinning. *Materials Letters*, 63(1):34–36, 2009.

[185] F. Hang, D. Lu, R. J. Bailey, I. Jimenez-Palomar, U. Stachewicz, B. Cortes-Ballesteros, M. Davies, M. Zech, C. Bodefeld, and A. H. Barber. In situ tensile testing of nanofibers by combining atomic force microscopy and scanning electron microscopy. *Nanotechnology*, 22(36):365708, 2011.

[186] Mohamed Basel Bazbouz and George K. Stylios. The tensile properties of electrospun nylon 6 single nanofibers. *Journal of Polymer Science Part B: Polymer Physics*, 48(15):1719–1731, 2010.

[187] E. Zussman, M. Burman, A. L. Yarin, R. Khalfin, and Y. Cohen. Tensile deformation of electrospun nylon-6,6 nanofibers. *Journal of Polymer Science Part B: Polymer Physics*, 44(10):1482–1489, 2006.

[188] Chia-Ling Pai, Mary C. Boyce, and Gregory C. Rutledge. Mechanical properties of individual electrospun pa 6(3)t fibers and their variation with fiber diameter. *Polymer*, 52(10):2295–2301, 2011.

[189] J. Zhou, Q. Cai, X. Liu, Y. Ding, and F. Xu. Temperature effect on the mechanical properties of electrospun pu nanofibers. *Nanoscale Res Lett*, 13(1):384, 2018.

[190] S. Jiang, G. Duan, E. Zussman, A. Greiner, and S. Agarwal. Highly flexible and tough concentric triaxial polystyrene fibers. *ACS Appl Mater Interfaces*, 6(8):5918–23, 2014.

[191] Shu-Ying Gu, Qi-Lin Wu, Jie Ren, and G. Julius Vancso. Mechanical properties of a single electrospun fiber and its structures. *Macromolecular Rapid Communications*, 26(9):716–720, 2005.

[192] Salman N. Arshad, Mohammad Naraghi, and Ioannis Chasiotis. Strong carbon nanofibers from electrospun polyacrylonitrile. *Carbon*, 49(5):1710–1719, 2011.

[193] E. Zussman, X. Chen, W. Ding, L. Calabri, D. A. Dikin, J. P. Quintana, and R. S. Ruoff. Mechanical and structural characterization of electrospun pan-derived carbon nanofibers. *Carbon*, 43(10):2175–2185, 2005.

[194] R. Shrestha, J. Cai, M. Naraghi, and M. P. de Boer. Size-dependent creep master curve of individual electrospun polymer nanofibers. *Experimental Mechanics*, 60(6):763–773, 2020.

[195] Philip A. Yuya, Yongkui Wen, Joseph A. Turner, Yuris A. Dzenis, and Zheng Li. Determination of young's modulus of individual electrospun nanofibers by microcantilever vibration method. *Applied Physics Letters*, 90(11), 2007.

[196] M. Naraghi, T. Ozkan, I. Chasiotis, S. S. Hazra, and M. P. de Boer. Mems platform for on-chip nanomechanical experiments with strong and highly ductile nanofibers. *Journal of Micromechanics and Microengineering*, 20(12), 2010.

[197] Gangyong Zhou, Tianrou Xiong, Shaohua Jiang, Shaoju Jian, Zhengping Zhou, and Haoqing Hou. Flexible titanium carbide–carbon nanofibers with high modulus and high conductivity by electrospinning. *Materials Letters*, 165:91–94, 2016.

[198] Feng An, Gaokuo Zhong, Qingfeng Zhu, Yongli Huang, Yang Yang, and Shuhong Xie. Synthesis and mechanical properties characterization of multiferroic bifeo3-cofe2o4 composite nanofibers. *Ceramics International*, 44(10):11617–11621, 2018.

[199] Zhihua Zhao, Xiaoqing Shen, Hongchang Yao, Jianshe Wang, Jinzhou Chen, and Zhongjun Li. Alumina nanofibers obtained via electrospinning of pseudo-boehmite sol/pvp solution. *Journal of Sol-Gel Science and Technology*, 70(1):72–80, 2014.

[200] Y. Q. Chen, X. J. Zheng, S. X. Mao, and W. Li. Nanoscale mechanical behavior of vanadium doped zno piezoelectric nanofiber by nanoindentation technique. *Journal of Applied Physics*, 107(9), 2010.

[201] Shiyou Xu, Yong Shi, and Sang-Gook Kim. Fabrication and mechanical property of nano piezoelectric fibres. *Nanotechnology*, 17(17):4497–4501, 2006.

[202] Qingfeng Zhu, Yuxia Gao, Yang Yang, Yongli Huang, Xiaolan Tan, Feng An, Kai Pan, and Shuhong Xie. Nanomechanical property measurements of srtio3 submicron-fiber. *Journal of Wuhan University of Technology-Mater. Sci. Ed.*, 33(6):1350–1354, 2018.

[203] Xi Chen and Yong Shi. Electrical determination of elastic modulus of individual pzt nanofibers by in situ sem. *Proceedings of the ASME Design Engineering Technical Conference*, 7, 2011.

[204] X. Liu, Z. Li, Y. H. Jiang, L. H. Zhan, Y. M. Hao, P. Zhang, and Y. H. Ding. Mechanical properties of a single sno2 fiber prepared from the electrospinning method. *Journal of Sol-Gel Science and Technology*, 84(1):152–157, 2017.

[205] Urszula Stachewicz, Russell J. Bailey, Wei Wang, and Asa H. Barber. Size dependent mechanical properties of electrospun polymer fibers from a composite structure. *Polymer*, 53(22):5132–5137, 2012.

[206] Jihoon Lee and Yulin Deng. Nanoindentation study of individual cellulose nanowhisker-reinforced pva electrospun fiber. *Polymer Bulletin*, 70(4):1205–1219, 2012.

[207] A. Morel, S. Domaschke, V. Urundolil Kumaran, D. Alexeev, A. Sadeghpour, S. N. Ramakrishna, S. J. Ferguson, R. M. Rossi, E. Mazza, A. E. Ehret, and G. Fortunato. Correlating diameter, mechanical and structural properties of poly(l-lactide) fibres from needleless electrospinning. *Acta Biomater*, 81:169–183, 2018.

[208] Dominik Jaeger, Jan Schischka, Jörg Bagdahn, and Raimund Jaeger. Tensile testing of individual ultrathin electrospun poly(l-lactic acid) fibers. *Journal of Applied Polymer Science*, 114(6):3774–3779, 2009.

[209] Liye Li, Pengcheng Liu, Kongjun Zhu, Jing Wang, Guoan Tai, and Jinsong Liu. Flexible and robust n-doped carbon nanofiber film encapsulating uniformly silica nanoparticles: Free-standing long-life and low-cost electrodes for li- and na-ion batteries. *Electrochimica Acta*, 235:79–87, 2017.

[210] Mao Wang, Hyoung-Joon Jin, David L. Kaplan, and Gregory C. Rutledge. Mechanical properties of electrospun silk fibers. *Macromolecules*, 37(18):6856–6864, 2004.

[211] Leon M. Bellan, Jun Kameoka, and Harold G. Craighead. Measurement of the young's moduli of individual polyethylene oxide and glass nanofibres. *Nanotechnology*, 16(8):1095–1099, 2005.

[212] E. P. S. Tan, C. N. Goh, C. H. Sow, and C. T. Lim. Tensile test of a single nanofiber using an atomic force microscope tip. *Applied Physics Letters*, 86(7), 2005.

[213] W. Wang, T. Peijs, and A. H. Barber. Indentation induced solid state ordering of electrospun polyethylene oxide fibres. *Nanotechnology*, 21(3):035705, 2010.

[214] Mirjana Grkovic, Dusica B. Stojanovic, Vladimir B. Pavlovic, Mirjana Rajilic-Stojanovic, Milos Bjelovic, and Petar S. Uskokovic. Improvement of mechanical properties and antibacterial activity of crosslinked electrospun chitosan/poly (ethylene oxide) nanofibers. *Composites Part B: Engineering*, 121:58–67, 2017.

[215] K. H. Chan, S. Y. Wong, X. Li, Y. Z. Zhang, P. C. Lim, C. T. Lim, M. Kotaki, and C. B. He. Effect of molecular orientation on mechanical property of single electrospun fiber of poly[(r)-3-hydroxybutyrate-co-(r)-3-hydroxyvalerate]. *J Phys Chem B*, 113(40):13179–85, 2009.

[216] Chia-Chun Liao, Cheng-Chien Wang, Kuo-Chen Shih, and Chuh-Yung Chen. Electrospinning fabrication of partially crystalline bisphenol a polycarbonate nanofibers: Effects on conformation, crystallinity, and mechanical properties. *European Polymer Journal*, 47(5):911–924, 2011.

[217] Yu Chen, Donghua Han, Wen Ouyang, Shuiliang Chen, Haoqing Hou, Yong Zhao, and Hao Fong. Fabrication and evaluation of polyamide 6 composites with electrospun polyimide nanofibers as skeletal framework. *Composites Part B: Engineering*, 43(5):2382–2388, 2012.

[218] Jian Yao, Maria F. Pantano, Nicola M. Pugno, Cees W. M. Bastiaansen, and Ton Peijs. High-performance electrospun co-polyimide nanofibers. *Polymer*, 76:105–112, 2015.

[219] Linlin Chen, Shaohua Jiang, Juan Chen, Fei Chen, Yunyun He, Yongmei Zhu, and Haoqing Hou. Single electrospun nanofiber and aligned nanofiber belts from copolyimide containing pyrimidine units. *New Journal of Chemistry*, 39(11):8956–8963, 2015.

[220] Haibo Xu, Shaohua Jiang, Chenhui Ding, Yongmei Zhu, Jinjiang Li, and Haoqing Hou. High strength and high breaking load of single electrospun polyimide microfiber from water soluble precursor. *Materials Letters*, 201:82–84, 2017.

[221] Min Kyoon Shin, Sun I. Kim, Seon Jeong Kim, Sung-Kyoung Kim, Haiwon Lee, and Geoffrey M. Spinks. Size-dependent elastic modulus of single electroactive polymer nanofibers. *Applied Physics Letters*, 89(23):231929, 2006.

[222] Jian Zhu, Yichun Ding, Xiaojian Liao, Wenhui Xu, Hean Zhang, and Haoqing Hou. Highly flexible electrospun carbon/graphite nanofibers from a non-processable heterocyclic rigid-rod polymer of polybisbenzimidazobenzophenanthroline-dione (bbb). *Journal of Materials Science*, 53(12):9002–9012, 2018.

.